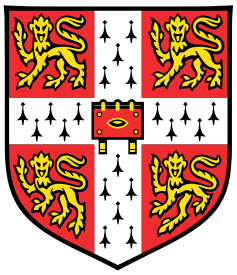

Josephson coupling and proximity effects through rare earth helimagnetic interfaces

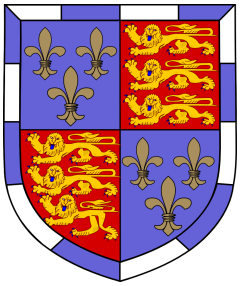

Bence Börcsök

Supervisor: Prof. Jason Robinson

Department of Materials Science and Metallurgy
University of Cambridge

This dissertation is submitted for the degree of
Doctor of Philosophy

St. John's College October 2019

Papának

aki megérte, hogy biciklivel menjek hozzájuk,
de azt már nem, hogy befejezzem a PhD-t.

Declaration

I hereby declare that except where specific reference is made to the work of others, the contents of this dissertation are original and have not been submitted in whole or in part for consideration for any other degree or qualification in this, or any other university. This dissertation is my own work and contains nothing which is the outcome of work done in collaboration with others, except as specified in the text and Abstract. This dissertation contains fewer than 60,000 words including abstract, appendices, footnotes, tables.

Bence Börcsök
October 2019

Acknowledgements

There are many people who supported me during my PhD. First and foremost, I would like to thank Jason Robinson for being a great supervisor. He believed in me even at times when I did not. Without his encouragements, contagious excitement for physics and well-timed bollocking, I could not have finished my PhD. I would also like to acknowledge Charles Simonyi, the Cambridge Trust and St. John's College, Cambridge for their financial support. I would also like to express my gratitude to St. John's College, Cambridge for welcoming me and supporting me in all activities, academic and non-academic. I especially grateful to our late master, Chris Dobson, my tutor, Sylvana Tomaselli, and graduate tutor, Sue Colwell, for their extraordinary work.

I would like to thank the Device Materials Group, especially Yuanzhou Gu, David Gustafson, Nadia Stelmashenko and Sachio Komori for training me and helping with my experiments. I am also thankful to Alexander Buzdin for the fruitful collaboration and Harry Bradshaw for proofreading my thesis.

The Cambridge University DanceSport Team has not only ensured that I am in good physical health but also given me many experiences and friends without whom my time at Cambridge would not have been the same. Rachel Cummings and I danced through four degrees together, and I am extremely proud of our accomplishments and grateful for our times together. David Mallabone has taught me a lot about dancing and even more about life and how to be a good person. I also have to thank Kirsty, Sam, Luke, Chi-Hé, Tom, Bex, Kien, Guy, Mary, Sav, Fil and Caitlin. I am incredible lucky to have met you.

I have the most amazing group of friends whom I owe a great deal of gratitude. I am eternally grateful to the SBR community, especially Jonathan, Sara, Tom, Jess and Harry, for all the fun we had over the past four years. I had the great pleasure of living with such amazing people as Rachel and Fred. I greatly appreciate those who stood by me despite the geographical distance: Jani, Réka, Kinga, Kriszta, Eszter, Rozi, Chaka. The Voolma family, Marin, Halliki, Silja, Linda and Leila, who has inspired and loved me so much that I cannot thank them enough. There is not enough space for me to give a full list but I am also thankful to all the College and University staff, my students and everyone who contributed to my PhD experience one way or another.

And last but definitely not least, those who set me on this journey. Thank you to KP for convincing me to apply to Cambridge, to János Schultz, Tamás Mező, Szilveszter Prókai and Zsuzsanna Fehér for preparing me for university and quite frankly for life. And most of all, an enormous thank you to my family. There are no words suitable to describe the love and gratitude I feel for your supporting and encouraging my ambitions and my crazy ideas and believing in me at all times. Knowing that I have a place and family to fall back on gave me the power and strength to push through what might have been the hardest challenge of my life so far.

Végül, de semmiképp sem utolsó sorban köszönet azoknak, akik elindítottak ezen a pályán. Köszönet KP-nak, hogy rábeszélt, hogy jelentkezzek Cambirdge-be, illetve Schultz Jánosnak, Mező Tamásnak, Prókai Szilveszternek és Fehér Zsuzsannának azért hogy felkészítettek az egyetemre és mindemellett az életre is. De a legnagyobb köszönettel a családomnak tartozom. Nincsenek szavak, amik elmondanák, hogy mennyire szeretlek titeket, és mennyire hálás vagyok nektek azért, hogy minden célom és elrugaszkodott ötletem támogatjátok és segítitek, és mindig hisztek bennem. A PhD talán a legnehezebb kihívás volt az életemben eddig, és a tudat, hogy van egy hely, ahol feltétel nélkül szeretnek, adott erőt ahhoz, hogy végig csináljam.

Abstract

This thesis presents research on the effect of superconducting-helimagnetic heterostructures. First, the electric and magnetic properties of epitaxial Nb(20 nm)/HoDy(40 nm) bilayers are studied. The saturation magnetisation values are consistent with previously reported values for Ho and Dy. The magnetic spiral is observed up to 43 % Dy content although the Dy content changes the stability of the helimagnetic state. The transition temperature (T_c) of the bilayers is obtained from resistance *vs* temperature curves for different external magnetic field values. T_c lowered as the HoDy alloy transitioned from the helimagnetic state to the ferromagnetic state. The change in T_c decreases with the Dy content.

Highly oriented Nb/Ho/Nb Josephson junctions are also studied in this work. The electron mean-free-path in the normal state is longer in the textured junctions than in the polycrystalline junctions reported below but still below the thermal coherence length implying that the transport processes are diffusive. The decay length of the critical current (I_c) in the helimagnetic state is over 100 nm and consistent with the non-magnetic coherence length in the dirty limit.

The external magnetic field (H) dependence of I_c deviates from the expected Fraunhofer pattern and shows split peaks with extra minima and concave central peak. A theoretical model was constructed to explain the $I_c(H)$ curves. The model assumes that the magnetisation increases faster along the edges of the junction and the highly magnetised regions propagate from the outside to the centre of the Ho barrier. The model successfully reproduces the characteristic features observed in the junctions and implies that in certain junctions, regions with 0 and π phase change coexist next to each other.

The main results presented in Chapter 9 have been published before the submission of this thesis:

B. Börcsök, S. Komori, A. I. Buzdin, and J. W. A. Robinson, Sci. Rep. 9, 5616 (2019)

Table of contents

Introduction

Superconductivity was discovered by Onnes who noticed that the resistivity of mercury drops to zero around 4.2 K. The lack of energy dissipation is still probably the most well-known property of superconductivity and most applications try to take advantage of the zero resistance. High temperature superconductors have the potential to reduce the energy loss between the power plants and the consumers by replacing parts of the electric grid with superconducting lines. The German city Essen has recently trialed a 1 km-long superconducting line [1].

Superconducting parts have also been proposed for electronic devices. Despite the continuous cooling required to keep the parts superconducting, the energy benefits can overweight the cooling cost resulting in more energy consuming systems like supercomputers and server centres [2]. Moreover, using superconducting computing elements can also make computers faster [3]. These potential advantages motivate the development of new superconducting devices with potential applications in computing.

Most superconducting devices rely on the interactions between superconducting and non-superconducting materials. In recent decades, there has been increased interest towards introducing ferromagnetic elements in superconducting devices. For example, the resistance of a superconducting spin valves can be controlled with an external magnetic field similarly to classical spin valves used in hard drive readout heads, although their resistance change comes from the suppression of superconductivity as opposed to the varying number of conduction channels. Josephson junctions with magnetic barriers also have potential application as logic gates in superconducting computing as well as qubits in quantum computers [3, 4]. Furthermore, Cooper pairs with spin-1 can be generated with inhomogeneous interface magnetisation, which opens up the possibility of using spin polarised supercurrent in information technology [5]. These are just a few of the potential applications of superconductor-ferromagnet heterostructures.

Rare earth ferromagnets provide an excellent candidate for superconducting devices. Their low exchange energy and lack of spin-polarisation enhance their interaction with superconducting material. They often also have more exotic magnetic structures at low

temperature including magnetic spirals. The helimagnetic state can be used to create the inhomogeneity to spin-1 Cooper pairs [6].

The aim of this thesis is to further understand the effects and behaviour of the magnetic spiral in superconducting devices. First, we study the proximity effect in highly-textured Nb/HoDy bilayers. The magnetic spiral is observed in the alloys and the effects of the transition from the helimagnetic state to the ferromagnetic state on the Nb is measured for multiple compositions. Secondly, the Josephson coupling is investigated in highly textured Nb/Ho/Nb junctions. The increased crystal quality leads to higher characteristic voltages across the junctions, which decays much slower with the barrier thickness than in the polycrystalline junctions.

The thesis consists of 4 Parts. Part I summarises the essential background knowledge used in this work including the fundamental theory of superconductivity (Chapter 1), Josephson effect (Chapter 2), magnetism (Chapter 3) and the ferromagnetic proximity effect (Chapter 4). Part II focuses on the experimental techniques used in the sample preparation (Chapter 5) and measurements (Chapter 6). The result of this work are presented and discussed in Part III with Chapter 7 presenting the measurements on Nb/HoDy bilayers, textured Ho Josephson junctions being discussed in Chapter 8 and the theoretical model for their magnetic dependence is presented in Chapter 9. We summarise the experiments (Chapter 10) and an outlook for potential future work (Chapter 11) in Part IV.

Part I

Background

Chapter 1

Basic superconductivity

Superconductivity was first discovered in 1911 by Onnes in solid mercury shortly after he managed to liquefy helium [7]. He noticed that below about 4.2 K the resistance of mercury disappeared. Soon many other metals were found to have superconducting phase at low temperatures. In 1933, Meissner discovered that superconductors fully expel any magnetic field and show perfect diamagnetism [8]. The phenomenon was named *Meissner effect* after him. However, it took almost 40 years to construct the first theory explaining conventional superconductivity. It was the Ginzburg-Landau theory in 1950 giving a phenomenological explanation [9] and the Bardeen-Cooper Schrieffer (BCS) theory followed in 1957 discovering the microscopic processes [10]. These theories allowed scientists to predict and exploit new phenomena in superconductors such as flux quantisation, the Josephson effect, etc. This chapter summarises the two fundamental theories of superconductivity. Section 1.1 outlines the Ginzburg-Landau theory and section 1.2 outlines the summarises the BCS theory. Section 1.3 discusses superconductivity outside the superconductor.

1.1 Ginzburg-Landau theory

The Ginzburg-Landau theory is a macroscopic theory, i.e. it provides a framework that can explain the observed properties and phenomena of the superconducting phase without explaining the microscopic processes responsible for the existence of the phase. It builds on Landau's earlier work on phase transitions and suggests that superconducting phase can be described by a complex order parameter (ψ) [11]. Experiments showed that the heat capacity changes discontinuously at the transition temperature (T_c), while the entropy remains continuous, therefore the superconducting transition must be a second order phase transition. Assuming the free energy density (f) is analytical near T_c and can be expressed in terms of the powers of ψ and $(T - T_c)$ and considering the coupling to the magnetic field, the

following form was proposed for f:

$$f = \alpha|\psi|^2 + \frac{\beta}{2}|\psi|^4 + \frac{1}{2m}\left|(-i\hbar\nabla + 2e\boldsymbol{A})\psi\right|^2 + \frac{1}{2\mu_0}\boldsymbol{B}_{\mathrm{M}}^2 \tag{1.1}$$

where $\boldsymbol{A}$ is the magnetic vector potential, $\boldsymbol{B}_{\mathrm{M}}$ is the magnetic field induced by the supercurrents, α, β and m are free parameters. The first two terms are from the Landau-theory to ensure that the phase transition is second order. When $\alpha > 0$, $\psi = 0$ minimises f, however when $\alpha < 0$, $|\psi| = \sqrt{-\alpha/\beta}$ with any arbitrary phase corresponds to a minimum, which breaks the symmetry of f. This means that α is temperature dependent and zero at T_{c} so close to T_{c} it can be approximated as $\alpha = a(T - T_{\mathrm{c}})$, while β needs to be a positive constant for the transition to be second order. The third term in (1.1) represents the gauge-invariant kinetic energy and m can be interpreted as an effective mass. It can be derived from the BCS theory that m represents the mass of the Cooper pairs, therefore $m = 2m_{\mathrm{e}}$, where m_{e} is the electron mass. The last term is the energy density of the magnetic field induced by the supercurrent. The positive sign of this term means that it acts as an energy penalty for magnetic fields inside the superconductor and leads to the Meissner effect. (1.1) contains all the lowest order terms that are consistent with the symmetries and gauge invariance of superconductivity.

In equilibrium, the total free energy must be at its minimum. Minimising f with respect to ψ and $\boldsymbol{A}$ gives the two Ginzburg-Landau equations:

$$\frac{1}{2m}(-i\hbar\nabla + 2e\boldsymbol{A})^2\psi + (\alpha + \beta|\psi|^2)\psi = 0 \tag{1.2}$$

$$\boldsymbol{j}_{\mathrm{s}} = \frac{\nabla \times \boldsymbol{B}_{\mathrm{M}}}{\mu_0} = \frac{ie\hbar}{m}(\psi^*\nabla\psi - \psi\nabla\psi^*) - \frac{4e^2\boldsymbol{A}}{m}\psi^*\psi = -\frac{2en_{\mathrm{s}}}{m}(\hbar\nabla\theta + 2e\boldsymbol{A}) \tag{1.3}$$

where $\psi = \sqrt{n_{\mathrm{s}}}\exp(i\theta)$, n_{s} is the superfluid density and θ is the superconducting phase.

(1.2) is the first Ginzburg-Landau equation and has a form similar to the Schrödinger-equation for a free particle meaning that ψ behaves similarly to a macroscopic wavefunction with the main difference that it is not linear. The second term includes a term with $|\psi|^2$ which breaks the linearity. The lack of linearity means that the superposition principle is not applicable for superconductivity unless $|\psi| \ll 1$ in which case the non-linear term is negligible and (1.2) becomes linear. The second Ginzburg-Landau equation defines the supercurrent density according to Ampère's law and relates it to ψ. The change of the superconducting phase results in a supercurrent along the gradient. Therefore, θ is changing linearly in superconducting wires carrying charge in zero magnetic field. The last term

includes $\boldsymbol{A}$ and implies that the presence of a magnetic field generates supercurrents in accordance with the Meissner effect.

The perfect diamagnetism of superconductors can be explained by taking the curl of (1.3)

$$\nabla^2 \boldsymbol{B} = \boldsymbol{B}/\lambda^2, \tag{1.4}$$

where $\lambda = \sqrt{m/(4\mu_0 e^2 n_\mathrm{s})}$ is the *London penetration depth*. (1.4) was originally derived from the London equations in 1935 by Fritz and Heinz London who were the first to explain the Meissner effect [12]. The London equations are based on classical considerations and assume that electrons move in the superconductor as if they were moving in vacuum. (1.4) is a typical screening equation and predicts the magnetic field to decay exponentially inside the superconductor as it is energetically favourable to shield an external field with supercurrents. The Ginzburg-Landau theory explains the origins of the London equation and derives an expression for λ. As $n_\mathrm{s} = |\alpha|/\beta$ and $\alpha \propto (T - T_\mathrm{c})$, λ is proportional to $(T - T_\mathrm{c})^{-1/2}$ and therefore diverge at T_c as expected.

London also suggested the following equation for the time evolution of the superconducting phase

$$\frac{\partial \theta}{\partial t} = \frac{2e}{\hbar}\phi \tag{1.5}$$

where ϕ is the electric potential. (1.5) cannot be derived from the Ginzburg-Landau free energy but it is familiar from quantum mechanics. Combining (1.5) with the time derivative of the current from (1.3) gives

$$\frac{\partial \boldsymbol{j}_\mathrm{s}}{\partial t} = -\frac{2en_\mathrm{s}}{m}\left(2e\nabla\phi + 2e\frac{\partial \boldsymbol{A}}{\partial t}\right) = \frac{4e^2 n_\mathrm{s}}{m}\boldsymbol{E} \tag{1.6}$$

where $\boldsymbol{E} = -\nabla\phi - \partial\boldsymbol{A}/\partial t$ is the electric field. (1.6) is an acceleration equation: an electric field increases the current through the superconductor but not needed to maintain that current. As we have seen so far Ginzburg-Landau theory successfully explains the resistance-free current and the perfect diamagnetism, the two main characteristics of the superconducting phase.

There are further phenomena that can be derived from the Ginzburg-Landau equations. Integrating (1.3) along a closed loop in a region where there is no supercurrent, i.e. $j_\mathrm{s} = 0$, shows that the enclosed magnetic flux must be

$$\phi = \oint \boldsymbol{A} \cdot \mathrm{d}\boldsymbol{l} = -\hbar/2e\Delta\theta \tag{1.7}$$

where $\Delta\theta$ is the total phase change of ψ along the loop. As ψ needs to be single valued, $\Delta\theta$ needs to be a multiple of 2π. This means that the magnetic flux enclosed by a superconductor is quantised with the magnetic flux quantum being $\phi_0 = h/2e$. The superconductor will screen the magnetic field inside a superconducting ring such that the flux is a multiple of ψ_0.

We can also investigate how small perturbations in ψ behave in the superconducting phase. If the superconductor is in a zero-field equilibrium state with uniform $|\psi| = \sqrt{n_s} = \sqrt{|\alpha|/\beta}$ and a small perturbation of $\delta\psi$ is introduced, (1.2) transforms into:

$$\nabla^2\delta\psi - \frac{2m}{\hbar^2}(-|\alpha| + 3\beta n_s)\delta\psi = \nabla^2\delta\psi - 2\frac{\delta\psi}{\xi^2} = 0 \tag{1.8}$$

where $\xi = \sqrt{\hbar^2/2m|\alpha|}$ is the *coherence length*. (1.8) shows that a perturbation dies off exponentially over the length-scale of ξ. The temperature-dependence of ξ is the same as λ and diverges at T_c. This is not surprising as the perturbations make ψ collapse as the system reaches T_c.

λ and ξ are the two characteristic length scales in the Ginzburg-Landau theory. They are both expressed in terms of fundamental constants and the free parameters from (1.1) and they can be used to write α and β in terms of measurable quantities. Both λ and ξ have the same temperature dependence and so their ratio (κ) is independent of T. κ only depends on material parameters and is used to distinguish between type I or a type II superconductors. The energy penalty for inducing magnetic field relative to the energy penalty for fluctuations in ψ is dependent on κ so type I and type II superconductors behave differently in strong magnetic fields.

The Ginzburg-Landau theory is based on the power series expansion of the free energy about T_c so it is the most accurate close to T_c. It is independent of the microscopic processes responsible for the existence of the superconducting phase, therefore it is applicable for both Type-I and Type-II superconductors and, with slight modifications, to other phase transitions, such as superfluidity. Its power lies in describing macroscopic process such as the effect of an external magnetic field on a superconductor, which relevant for Josephson junction discussed in Chapter 2. Although the Ginzburg-Landau theory is powerful to describe macroscopic processes, it is insufficient to predict physical parameters, like T_c or ξ and to analyse microscopic phenomena such as the long range triplet generation. To fully understand superconductivity a microscopic theory, such as the Bardeen-Cooper-Schrieffer (BCS) theory, is needed.

1.2 BCS theory

Although both superconductors and superfluids can be described by the Ginzburg-Landau theory, their microscopic theory is very different. The main reason is that the particles involved in superfluidity are bosons while in superconductivity they are fermions. Einstein and Bose suggested the existence of Bose-Einstein condensate in 1924 for photons and then they extended their theory for massive bosons [13]. In 1938 Fritz London suggested a mechanism for superfluidity [14] and in 1947 Boguliubov derived the kinetic equations and the spectrum of excitations from the second-quantised Hamiltonian [15]. Even though the two phenomena are very similar in some sense, both involve particles moving without dissipating energy, they are different in that electrons cannot form a Bose-Einstein condensate because of the Pauli exclusion principle so a different theory was needed to describe superconductors.

In 1957 Bardeen, Cooper and Schrieffer proposed that electrons can have attractive interactions mediated by lattice vibration (phonons) [10]. For stationary charge, the lattice distorts to screen the charge. If an electron is moving fast enough there will be a delay in restoring the lattice, which leads to a positively charged screening cloud behind it. The positive tail will attract other electrons. They also showed that an overall attractive interaction of any magnitude between the electrons near the Fermi surface leads to the formation of Cooper pairs at low temperatures. Cooper pair is a pair of electrons with opposite wave vectors coupled together in the spin singlet state. As the electrons are in a spin singlet state, their overall spin is zero, which means that they can behave similar to bosons and undergo condensation.

A year later Boguliubov confirmed the theory by deriving the existence of Cooper pairs using second quantisation assuming four-point interactions between the electrons [16]. Using the creation operator $a^{\dagger}_{\mathrm{k},\uparrow}$, which creates a single electron with momentum k and spin up, and the annihilation operator $a_{k,\uparrow}$, the effective Hamiltonian is

$$\hat{H} = \sum_{k,\sigma} \varepsilon_k a^{\dagger}_{k,\sigma} a_{k,\sigma} + \frac{1}{2} \sum_{k_1,\sigma_1,k_2,\sigma_2,q} a^{\dagger}_{k_1+q,\sigma_1} a^{\dagger}_{k_2-q,\sigma_2} V_{k_1,k_2,q} a_{k_1,\sigma_1} a_{k_2,\sigma_2}. \tag{1.9}$$

The first term represents the kinetic energy for single-particle energy measured from the chemical potential (μ) $\varepsilon_{\mathrm{k}} = \hbar^2 k^2/2m_{\mathrm{e}} - \mu$. The second term is the potential energy term for a four point interaction between two electrons where the transferred momentum is q. $V_{\mathrm{k_1,k_2,q}}$ is the energy change corresponding to the momentum transfer and is negative if the interaction if attractive. This Hamiltonian assumes that interactions between electrons are local and can be thought of as a collision. This assumption is reasonable in that sense that the

superconducting condensate can be derived using it. For some more complicated phenomena, such as the proximity effect discussed in Section 1.3, a non-local Hamiltonian is needed.

The BCS state is a coherent state of Cooper pairs and can be written in the following form *k*

$$|\mathrm{BCS}\rangle = \prod_k \left(u_k + e^{\mathrm{i}\theta} v_k a^\dagger_{k+s,\uparrow} a^\dagger_{-k+s,\downarrow}\right)|0\rangle \tag{1.10}$$

where $|0\rangle$ is the vacuum state. $a^\dagger_{k+s,\uparrow} a_{-k+s,\downarrow}$ creates a Cooper pair with pair momentum $2\hbar s$. As all pairs have the same pair momentum and phase, the state represent a supercurrent flow and in the ground state $s = 0$. From the normalisation of $|\mathrm{BCS}\rangle$, $u_k^2 + v_k^2 = 1$, where u_k^2 and v_k^2 are the probabilities of the given state being empty or filled. To find the values for u_k and v_k, the expectation value of the Hamiltonian needs to be minimised, which takes the following form for the $s = 0$ ground state

$$\langle E\rangle = \langle \mathrm{BCS}|\hat{H}|\mathrm{BCS}\rangle = \sum_k 2v_k^2\varepsilon_k + \sum_{k,k'} v_k u_{k'} u_k v_{k'} V_{k,-k,k'-k}. \tag{1.11}$$

The $\frac{1}{2}$ factor is missing from the second term because $V_{k,-k,k'-k} = V_{-k,k,k'-k}$ it is the same if $k_1 = k$ and $k_2 = -k$ or the other way around. Minimising $\langle E\rangle$ with respect to v_k and the normalisation condition gives

$$2u_k v_k \varepsilon_k - \Delta_k(u_k^2 - v_k^2) = 0 \tag{1.12}$$

where

$$\Delta_k = -\sum_{k'} u_{k'} v_{k'} V_{k,-k,k'} \tag{1.13}$$

Δ_k can be interpreted as an internal field describing the overall influence of the other pairs. It can vary in space and it used as the main quantity to describe the superconducting state in the BCS theory. For most systems $V_{k,-k,k'}$ is only slightly depend on the value of k and for most cases the band gap can be assumed to be independent of k, $\Delta_k = \Delta$. This is called the *weak-coupling limit*.

With further algebra it can be shown that energy dispersion for single-particle excitations, i.e. electrons from breaking Cooper pairs, depends on Δ

$$E_k^2 = \varepsilon_k^2 + \Delta^2. \tag{1.14}$$

This means that creating an excitation requires at least Δ energy. There is a gap with size Δ in the excitation spectrum, which is why Δ is called the *BCS band gap*. Measurements have found such gaps in the excitation spectrum of superconductors before the BCS theory

and this prediction supports the validity of the theory. This also means that all scattering processes with energies below Δ are prohibited because there are no available states to transfer into. This leads to the dissipationless supercurrent. The presence of excitations decreases the binding energy and hence Δ, since the sum in (1.13) has fewer terms. This is why the superconducting phase collapses above the critical current density. Once current has enough energy to create a few excitations, it decreases the band gap, which lead more and more excitations until all Cooper pairs break up.

The values for u_k and v_k can be expressed from (1.12) in terms of Δ and ε_k. Substituting these back to (1.13) gives the *self-consistency equation* for Δ

$$\Delta = -\sum_k \frac{\Delta}{2\sqrt{\varepsilon_k^2 + \Delta^2}} V. \tag{1.15}$$

The self-consistent equation provides a route to calculate or estimate Δ from the density of states relevant k values. For example in the weak-coupling limit, we can assume that only energies below the $k_\mathrm{B}\theta_\mathrm{D}$ are relevant, where θ_D is the Debye temperature. The sum can be turned into an integral and we get

$$\Delta = \frac{k_\mathrm{b}\theta_\mathrm{D}}{\sinh(1/NV)} \approx 2k_\mathrm{B}\theta_\mathrm{D} e^{-1/\mathrm{NV}} \tag{1.16}$$

From (1.16) it is obvious that if there is any attractive interaction between electrons, the superconducting gap will appear at $T = 0$.

So far we only considered superconductivity at $T = 0$. For $0 < T < T_\mathrm{c}$ the superconductivity still exists but excitations will be present due to thermal fluctuations. If the occupation number of excitations with E_k energy (f_k) is known, the calculations can be carried out very similarly to the zero-temperature case. (1.14) remains the same but the self-consistent equation changes to

$$\Delta = -\sum_k (1 - 2f_k) \frac{\Delta}{2\sqrt{\varepsilon_k^2 + \Delta^2}} V. \tag{1.17}$$

(1.17) can be used to calculate $\Delta(T)$ at any temperature. Assuming f_k has Fermi distribution, the self-consistent can be solved numerically at the transition temperature, where $\Delta(T_\mathrm{c}) = 0$, giving

$$k_\mathrm{B}T_\mathrm{c} = 1.14 k_\mathrm{B}\theta_\mathrm{D} e^{-1/\mathrm{NV}} \tag{1.18}$$

Comparing (1.18) to (1.16), T_c can be related to Δ at zero temperature $\Delta_0 = 1.76 k_\mathrm{B}T_\mathrm{c}$. Similarly the temperature dependence of Δ near T_c can be derived as $\Delta(T) \approx 1.74\Delta_0\sqrt{1 - T/T_\mathrm{c}}$. This is clearly not true at very low temperatures because it grows over Δ_0.

Gor'kov derived the Ginzburg-Landau equations from the BCS model [17]. In his derivation he used the Fourier transform of the creation and annihilation operators, which describe the creation of and annihilation of electrons at a certain position instead of with a certain momentum. He found that the Ginzburg-Landau order parameter is proportional to the expectation value of the pair annihilation operators in real space. Considering the non-local interactions in superconductors he also related ψ to the *gap field* ($\Delta(r)$) and found that $\xi = \hbar v_{\mathrm{F}}/\pi\Delta_0$, where v_{F} is the Fermi velocity. This confirms that both theories are equally valid description of superconductivity. This allows us to use them interchangeably to describe superconducting processes.

1.3 Superconductivity at the interface

In the previous sections, we only considered bulk superconductivity and ignored any effects from surfaces. Surfaces and interfaces become important in thin film superconductors and nanoscale devices such as Josephson junctions. We present a macroscopic and microscopic approach to understand the influence of interfaces on the superconductor.

1.3.1 Proximity effect

We start with a macroscopic approach following the Ginzburg-Landau theory. In section 1.1, we minimised free energy density f to derive the Ginzburg-Landau equations. However in principle, the total free energy (F) is the quantity that needs to be minimal when the superconductor is at equiliblrium

$$F = \int_{\mathrm{V}} f \mathrm{d}V = F_0 + \int_{\mathrm{V}} \left[\alpha |\psi|^2 + \frac{\beta}{4}|\psi|^2 + \frac{1}{2m}\left|(-i\hbar\nabla + 2e\boldsymbol{A})\psi\right|^2 + \frac{1}{2\mu_{\mathrm{o}}} B_{\mathrm{M}}^2 \right] \mathrm{d}V. \quad (1.19)$$

In the bulk minimising F and f is equivalent. The distinction only becomes significant at the surfaces. To study the surface contribution the kinetic energy term can be rewritten using the divergence theorem

$$\begin{aligned} \int_{\mathrm{V}} \frac{1}{2m}\left|(-i\hbar\nabla + 2e\boldsymbol{A})\psi\right|^2 \mathrm{d}V = & \int_{\mathrm{V}} \frac{1}{2m}\psi^*(-i\hbar\nabla + 2e\boldsymbol{A})^2\psi \mathrm{d}V \\ & + \frac{i\hbar}{2m}\oint_{\mathrm{V}} \psi^*(-i\hbar + 2e\boldsymbol{A})\psi \mathrm{d}S \end{aligned} \quad (1.20)$$

If we now minimise F with respect to ψ and A we get back the Ginzburg-Landau equations from the volume integrals but the surface integral yields a boundary condition

$$(-i\hbar\nabla_{\mathrm{n}} + 2eA_{\mathrm{n}})\psi = 0 \tag{1.21}$$

where the suffix n refers the component normal to the surface. This form of the boundary condition means that in the absence of a magnetic field $|\psi|$ remains the same right to the surface. (1.1) includes no term for surface energy so there is no energy penalty for keeping ψ large at the surface or having a discontinuity in ψ. The microscopic theory has confirmed that (1.21) is the correct boundary condition for interfaces with vacuum and insulators, when electrons are fully reflected from the surface. When electrons can leave the superconductor, into a normal metal (N) for example, including a surface energy term proportional to $|\psi|^2$ in (1.20) gives a more appropriate boundary condition in the form of

$$(-i\hbar\nabla_{\mathrm{n}} + 2eA_{\mathrm{n}})\psi = \frac{\psi}{b} \tag{1.22}$$

where b is called the *extrapolation length*. As the gradient of ψ is negative at the surface, ψ is decreasing near the surface and b determines the level of suppression. The suppression from the surface exponentially approaches the bulk value over the coherence length. (1.1) is also valid in the normal metal but α is positive and ψ is zero in the bulk. At the surface however, ψ is non-zero and exponentially decays into N over the length scale of the coherence length in N (ξ_{n}). If ξ_{n} is finite, ψ can penetrate N over a finite distance. Therefore, placing a normal metal next to a superconductor weakens the superconductivity in the superconductor near the surface and induces superconductivity in the normal metal over a short distance. These phenomena are called the *proximity effect* and the *inverse proximity effect* and were first experimentally demonstrated by Meissner in 1960 [18]. The measurement showed that thin layers of normal metals (Cu, Au, Ag, Cr, Fe, Co, Ni and Pt) can become superconducting when placed in contact with superconducting tin and that the T_{c} for thin tin wires decreases if coated with normal metals.

The suppression of the superconductivity decays into the superconductor over the coherence length like most perturbations. The decay length of ψ in the normal metal is

$$\xi_{\mathrm{n}} = \frac{\hbar v_{\mathrm{F}}}{2\pi k_{\mathrm{B}} T} \qquad \text{or} \qquad \xi_{\mathrm{n}} = \sqrt{\frac{\hbar v_{\mathrm{F}} l}{6\pi k_{\mathrm{B}} T}} \tag{1.23}$$

in the clean and the dirty limit respectively, where l is the electron mean free path. In the clean limit $\xi < l$ and the electron's motion is ballistic, while in the dirty limit $l \ll \xi_{\mathrm{n}}$ meaning that the electron's motion is diffusive.

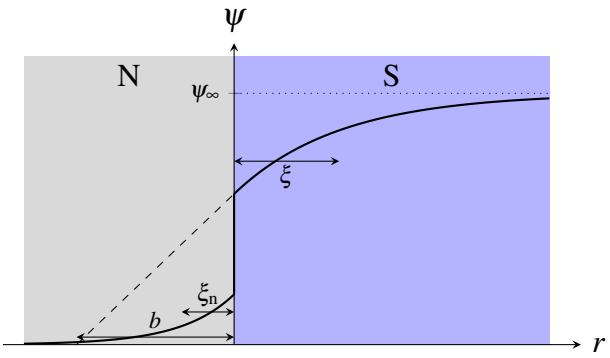

Fig. 1.1 An illustration of ψ at a SN interface. The dashed line shows the extrapolation from the gradient of ψ at the interface. The decay length of ψ in S and N are ξ and ξ_n respectively.

For an exact solution, the Boguliobov equations need to be solved in principle. However, besides a few simple cases solving the Boguliobov equation is troublesome and simplifications are needed [19, 20]. The equations can be simplified by using Green functions and applying quasiclassical approximations that average over the oscillations below the characteristic length scales of superconductivity. For systems in the dirty limit ($l \ll \xi_F$), this leads to the Usadel equation for the normal ($G(x,\omega)$) and anomalous Green's functions ($F(x,\omega)$)

$$\begin{gathered} -\frac{D}{2}\left[G(x,\omega)\frac{\partial^2}{\partial x^2}F(x,\omega) - F(x,\omega)\frac{\partial^2}{\partial x^2}G(x,\omega)\right] + \omega F(x,\omega) = \Delta(x)G(x,\omega) \\ G^2(x,\omega) + F^2(x,\omega) = 1 \end{gathered} \tag{1.24}$$

where $\omega = (2n+1)\pi T$ are the Matsubara frequencies and $D = v_F l/3$ is the diffusion coefficient and the second equation is the normalisation condition [21]. In the N region $\Delta(x) = 0$ so the right-hand side is zero. Similarly to (1.15), the Usadel equation is also accompanied by a self-consistency equation for the S layer

$$\Delta(x)\ln\frac{T_c}{T_{c0}} + \pi k_B T_c \sum_\omega \left(\frac{\Delta(x)}{\hbar|\omega|} - F_s(x,\omega)\right) = 0 \tag{1.25}$$

where T_c is the critical temperature of the structure and T_{c0} is the critical temperature of the bulk superconductor.

Kuprianov and Lukichev derived the general boundary conditions for Usadel equation [22] which takes the following form near T_c

$$\begin{aligned} \sigma_s \left(\frac{\partial F_s}{\partial x}\right)_{x=0} &= \sigma_n \left(\frac{\partial F_n}{\partial x}\right)_{x=0}, \\ F_s(0) &= F_n(0) + R_{int}\sigma_s \left(\frac{\partial F_s}{\partial x}\right)_{x=0}, \end{aligned} \tag{1.26}$$

where σ is the normal state conductivity and R_{int} is the interface resistance per unit area. Equivalent boundary conditions apply for $G(x,\omega)$. (1.26) shows that ψ can be discontinuous and R_{int} increases the discontinuity at the boundary and hence weakens the proximity effect. This is not surprising as when the transparency is low (and R_{int} is large), most of the electrons are reflected back from the interface and the regions can hardly affect each other. An illustration of ψ at an interface is shown in Fig 1.1.

1.3.2 Andreev reflection

For a microscopic approach we need to understand how single electrons can form Cooper pairs at the interface and how normal current is converted to supercurrent and vice versa. A single electron is an excitation in the superconducting phase but excitations are not allowed below the gap, which suggest that low energy normal currents cannot enter superconductors. There are no experimental observations of this. Andreev gave a theoretical explanation for the normal current-supercurrent conversion in 1964 and the process was named *Andreev reflection* after him [23]. He considered an electron approaching the superconductor from the N side with energy E. Near the interface Δ increases from 0 to Δ_s, which is the band gap at the interface. The electron needs to be reflected back at the point when $\Delta(r) = E$. However, considering the *Boguliobov equations*, which can be considered the non-local equivalents of (1.12), it turns out that the electron is reflected as a hole with opposite spin and momentum. The process conserves energy and momentum and enters $2e$ charge into the superconductor meaning a Cooper pair is formed. The process works the same way for hole which are reflected from the interface as electrons. Andreev reflection does not change the entropy therefore there is no energy barrier or interface resistance (R_{int}) for the current flowing through an NS interface. This process assumes that the electron has energy below the bulk band gap (Δ_∞) and that $\Delta(r)$ changes slowly compared to the Fermi wavelength near the interface. If there is a sharp change in the band gap, part of the current is reflected back to N. If the electrons are higher in energy than Δ_∞, they can enter S as excitations. Both of these processes involve energy dissipation and lead to an interface resistance. High temperatures, when Δ is suppressed and impurities on the interface, which decrease the

transparency and result in a sharp change in $\Delta(r)$, both increases R_{int}. Andreev reflection is also strongly inhibited in ferromagnet-superconductor interfaces because electrons are highly spin-polarised and the process is spin-dependent.

Chapter 2

Josephson effect

In the previous section we saw that superconductivity can survive in a non-superconducting material over a short range. If a very thin barrier is placed between two superconductor, the decaying order parameters overlap and therefore the supercurrent can flow through the barrier. This structure is called a *Josephson junction*, named after Brain Josephson who theoretically predicted the phenomenon in 1962 [24]. His original calculations considered tunnel junctions with insulating barrier (I) but the general results hold for a wide range of structures and were experimentally confirmed shortly after [25–27]. Josephson junctions have been used for magnetic field measurements in SQuID devices and the new voltage calibration standard also relies on Josephson junctions. In this chapter, we discuss the most important properties of Josephson junctions.

2.1 Weak links

Superconducting junctions are normally classified based on the strength of the coupling between the superconducting electrodes. Strong links provide a strong coupling and behave as a continuous bulk superconductor therefore ψ is continuous across a strong link. On the other hand, weak links are capable of carrying supercurrent but their behaviour is different from bulk superconductors, for example ψ can be discontinuous in a weak link [28]. Even though the main results hold for a wide range of structures, we only consider weak links here.

When the phase on one side of the link is increased by 2π, a strong link is left with a phase gradient and a supercurrent flowing through it as ψ needs to remain continuous. However, a weak link returns to the original state, which means that the free energy of the link

must be a periodic function of the superconducting phase across the junction ($\Theta = \theta_2 - \theta_1$):

$$F = -F_0 \cos(\Theta) \tag{2.1}$$

where F_0 is a positive constant. If there is a voltage V across the weak link, it will increase the phase difference according to (1.5). The power done on the link by the current I_s, which is $I_s V$, must be equal to the time derivative of the free energy

$$I_s V = \frac{\partial F}{\partial t} = F_0 \sin(\Theta) \frac{2eV}{\hbar} \tag{2.2}$$

and therefore

$$I_s = I_c \sin(\Theta) \tag{2.3}$$

where $I_c = 2eF_0/\hbar$ is the Josephson critical current. I_s is a supercurrent as it can flow through the weak link even when $V = 0$ if $-I_c < I_s < I_c$.

2.2 Josephson critical current

To deduce the magnitude of I_c the microscopic theory is needed to be considered. Josephson originally derived his theory for tunnel junctions, where the two superconductors are separated by a thin normal metal layer (N). If the thickness of the N layer (d) is short compared to the characteristic lengths, especially the coherence length in N (ξ_n), the tunnelling process can be described by the tunnelling coefficient t and the density of states on both sides. If the same superconducting material is used on both sides of the junction the following formula can be derived for the critical current [24, 29, 30]

$$I_c = \frac{\pi \Delta(T)}{2eR_n} \tanh\left(\frac{\Delta(T)}{2k_B T}\right) \tag{2.4}$$

where $\Delta(T)$ is the BCS band gap of the superconductor at temperature T, and R_n is the normal state resistance of the junction and it includes the effect of t. Important to note that $I_c R_n$, also called characteristic voltage, is independent of the thickness of the N layer and all thickness dependence is included in R_n. At $T = 0$, the the characteristic voltage, is $\pi\Delta(0)/2e$ in an ideal weak link.

When d is comparable to or greater than ξ_N, (2.4) is not accurate anymore as a significant proportion of the Cooper pairs is lost in N. In this case the proximity effect on both sides of N needs to be considered. The order parameter penetrates the normal metal from both sides and they overlap in the middle therefore supercurrent can flow through the junction.

The calculations give a simple formula for critical current near T_c [31, 28]

$$I_c = \frac{3\pi}{2eR_n}\frac{\Delta_s^2}{kT_c}\frac{d/\xi_N}{\sinh(d/\xi_N)} \tag{2.5}$$

where d is the thickness of the barrier, Δ_s is the BCS band gap just in side the superconductor. Δ_s is used in this formula to take into account the inverse proximity effect. The thickness dependence of the characteristic voltage is dictated by the $(d/\xi_N)/\sinh(d/\xi_N)$ part, which can be closely estimated as an exponential decay. The length scale of the decay is set by ξ_N, which is equal to $\hbar v_F/2\pi k_B T$ in the clean limit and to $\sqrt{l\hbar v_F/6\pi k_B T}$ in the dirty limit, where l is the electron mean free path in N. As both Δ_s and ξ_N increases with falling temperature, I_c also increases when T is decreasing for both thick and thin Josephson junctions. (2.4) takes the same for near T_c as (2.5) does when $d \to 0$

$$I_c \propto \frac{1}{eR_n}\frac{\Delta_0^2}{kT_c^2}(T_c - T) \tag{2.6}$$

where Δ_0 is the BCS band gap at $T = 0$. The agreement in the limiting cases shows the consistency of the theories. Both formulas predict I_c to increase linearly with temperature near T_c.

The critical current can be calculated at a general temperature using the Usadel equation. Once the Green's functions $F(x,\omega)$ and $G(x,\omega)$ are obtained from (1.24) and from the relevant boundary conditions, the supercurrent density through the Josephson junction takes a from similar to (1.3)

$$j_s(\Theta) = ienD\pi k_B T \sum_\omega \left(F\frac{\mathrm{d}F^*}{\mathrm{d}x} - F^*\frac{\mathrm{d}F}{\mathrm{d}x} \right), \tag{2.7}$$

where n is the electron density and D is the diffusivity. In most cases the form of F is such that (2.7) has the normal sinusoidal dependence $I_s = I_c \sin\Theta$. For low interface transparency, (2.7) transforms into [32]

$$j_c = ienD\pi k_B T \sum_\omega \left(\frac{\Delta}{\hbar\omega}\right)^2 \frac{2k/\cosh(2kd)}{\tanh(2kd)(1+\Gamma^2k^2)+2k\Gamma}, \tag{2.8}$$

where $k = \sqrt{2\omega/D}$ is the wave vector and $\Gamma = R_{int}\sigma_n\sqrt{\Delta^2+\hbar^2\omega^2}/\hbar\omega$ is the interface factor. (2.8) takes into account the affect of the interface, which in general lowers the critical current. However, in the perfectly transparent limit ($R_{int} \to 0$) it becomes similar to (2.5). (2.8) is

widely used to fit measurement data for metallic Josephson junctions and we also use it in Chapter 8.

2.3 Current-source model

If the current through the junction is greater than I_c, some voltage is required across the junction. The current-voltage characteristics (IV) can be complicated for Josephson junctions but for most cases the *resistively shunted junction* (RSJ) model provides a reasonable explanation. In the RSJ model, the supercurrent flows through an ideal Josephson element and all the normal current flows through a normal resistance in parallel to the junction. The voltage arises from the normal current through the resistance.

Let us consider what happens when we drive a current I through a junction in the RSJ model. I is the sum of the currents flowing through the Josephson element (I_s) and through the normal resistor (I_n)

$$I = I_s + I_n = I_c \sin(\Theta) + V/R \tag{2.9}$$

where V is the voltage across the junction and R_n is the normal state resistance. (2.9) can be turned into a differential equation of Θ using (1.5) and $V = \phi$

$$\frac{\hbar}{2eR}\frac{d\Theta}{dt} = I - I_c \sin(\Theta). \tag{2.10}$$

It is easy to see that if $I < I_c$, Θ reaches a value for which $V = 0$ and the junction is fully superconducting. If $I > I_c$ however, Θ keeps increasing. The analytical solution to (2.10) is

$$I \tan\left(\frac{\Theta}{2}\right) = I_c + \frac{\bar{V}}{R_n}\tan\left(\frac{\omega_J t}{2}\right) \tag{2.11}$$

where $\omega_J = 2e\bar{V}/\hbar$ is the Josephson frequency and $\bar{V}$ is the mean voltage across the junction defined by the following relationship

$$\left(\frac{\bar{V}}{R_n}\right)^2 = I^2 - I_c^2. \tag{2.12}$$

$\bar{V}$ has this quadratic behaviour because the superconducting phase is continuously increasing if $I > I_c$ so the supercurrent oscillates. It is easy to see from (2.10) that Θ changes slower near $\sin\Theta = 1$ than near $\sin\Theta = -1$ so the time average of I_s is not 0. As $\bar{V}$ increases, I gets closer and closer to $\bar{V}/R_n$ because the fluctuation in the rate of change of Θ gets smaller so the Josephson junction behaves as a normal resistor when the $I \gg I_c$ (Fig 2.1).

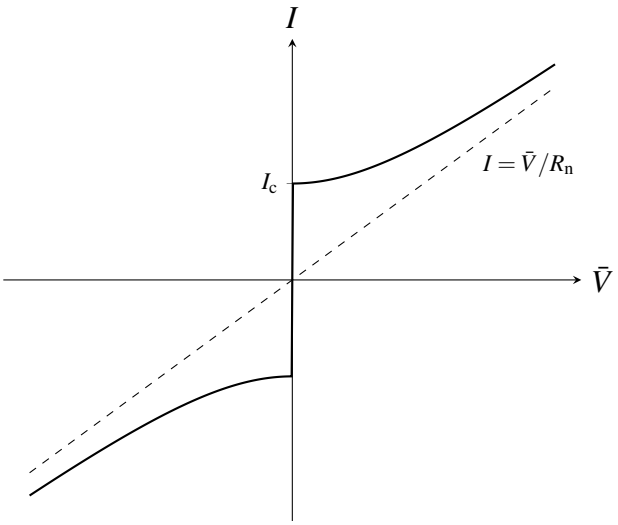

Fig. 2.1 The current-voltage characteristics for the resistively shunted junction model. The dashed line indicates the classical resistance approached asymptotically at high voltages.

2.4 Josephson junctions in magnetic field

So far we only investigated Josephson junction in zero magnetic field. The second Ginzburg-Landau equation links the superconducting phase to the vector potential so a non-zero magnetic field will affect Θ and hence I_c. To understand how I_c depends on an external magnetic field B, first we need to look at the relationship between $\boldsymbol{A}$ and Θ.

2.4.1 Gauge invariance

The Ginzburg-Landau equations depend on $\boldsymbol{A}$ and ψ, which are not observable quantities but related to the electric and magnetic fields as $\boldsymbol{E} = -\nabla\phi - \partial\boldsymbol{A}/\partial t$ and $\boldsymbol{B} = \nabla \times \boldsymbol{A}$. $\boldsymbol{E}$ and $\boldsymbol{B}$ remain unchanged under the gauge transformation $\boldsymbol{A} \to \boldsymbol{A} + \nabla\chi$ and $\phi \to \phi + \partial\chi/\partial t$, where $\chi(\mathbf{r},t)$ is an arbitrary function. The supercurrent j_s is observable and cannot depend on the gauge. To make sure that (1.3) is gauge invariant, the superconducting phase also needs to undergo the gauge transformation $\theta \to \theta - (2e/\hbar)\chi$. Similarly, the Josephson critical current also has to be gauge invariant, therefore Θ in (2.3) must be the gauge invariant phase difference defined by

$$\Theta = \theta_2 - \theta_1 - \frac{2e}{\hbar}\int_1^2 \boldsymbol{A}\cdot \mathrm{d}\boldsymbol{l} \tag{2.13}$$

where the integral is evaluated along any line between the superconducting electrodes With this definition of Θ, all equations in the previous sections remain true and can be used to investigate the behaviour of a Josephson junction in a magnetic field.

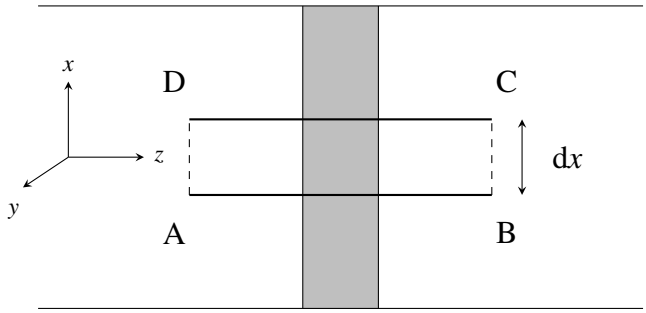

Fig. 2.2 The schematic of the path integrals in (2.14).

2.4.2 Quantum interference

In general, Θ is position dependent. To understand how Θ varies with position, let us evaluate (2.13) for two lines dx from each other (Fig 2.2). If the integrals start and end deep inside the superconducting electrodes where the magnetic field is zero and ψ and θ is uniform, the change in Θ must be equal to the difference between the two line integrals of $\boldsymbol{A}$

$$\begin{aligned}\Delta\Theta &= \theta_{\mathrm{C}} - \theta_{\mathrm{D}} - \frac{2e}{\hbar}\int_{\mathrm{D}}^{\mathrm{C}} \boldsymbol{A}\cdot\mathrm{d}\boldsymbol{l} - \theta_{\mathrm{B}} + \theta_{\mathrm{A}} + \frac{2e}{\hbar}\int_{\mathrm{A}}^{\mathrm{B}} \boldsymbol{A}\cdot\mathrm{d}\boldsymbol{l} \\ &= \frac{2e}{\hbar}\left(\int_{\mathrm{A}}^{\mathrm{B}} \boldsymbol{A}\cdot\mathrm{d}\boldsymbol{l} - \int_{\mathrm{D}}^{\mathrm{C}} \boldsymbol{A}\cdot\mathrm{d}\boldsymbol{l}\right).\end{aligned} \tag{2.14}$$

As shown in the previous section, Θ is gauge invariant so (2.14) can be evaluated in any gauge. If we consider the gauge in which $\boldsymbol{A} = 0$ deep inside the superconductor, where the magnetic field is zero, the line integrals of $\boldsymbol{A}$ between A and D, and C and B must be zero. Therefore, connecting the two line integrals to form a rectangular loop integral does not change the right-hand side

$$\Delta\Theta = \frac{2e}{\hbar}\oint \boldsymbol{A}\cdot\mathrm{d}\boldsymbol{l} = 2\pi\frac{\Delta\phi}{\phi_0} \tag{2.15}$$

where $\Delta\phi$ is magnetic flux through the ABCDA loop. The second equation uses the fact that the integral of the magnetic vector potential along a closed loop is equal to the magnetic flux through that loop. The magnetic flux can be written as $\Delta\phi = Bd_{\mathrm{eff}}\mathrm{d}x$, where B is the component of magnetic field at the centre of the junction perpendicular to the ABCD loop and d_{eff} is the effective thickness of the junction such that $Bd_{\mathrm{eff}} = \int_{\mathrm{A}}^{\mathrm{B}} B_{\perp}\mathrm{d}l$. This relates the gradient of Θ to the magnetic field perpendicular to its direction

$$\frac{\partial\Theta}{\partial x} = 2\pi\frac{Bd_{\mathrm{eff}}}{\phi_0}. \tag{2.16}$$

An equivalent equation for $\partial\Theta/\partial y$ can be derived. If the spacial variation of B and d_{eff} is known, $\Theta(x,y)$ can be obtained by solving the differential equations. To find the total critical current, we need to integrate over the whole junction

$$I_{\text{c}} = \iint j_{\text{c}}(x,y)\sin[\Theta(x,y)]\text{d}x\text{d}y \tag{2.17}$$

where j_{c} is the local critical current density. j_{c} can be affected by impurities and the interface quality through Δ_{s} and ξ_{N} as discussed in Section 2.2. This is the general method to calculate how an external field influences the critical current in a Josephson junction. In Section 2.6 (2.17) is evaluated for circular and rectangular junctions with negligible screening.

2.5 Magnetic screening

The difficulty in using the method outlined in the previous section is that B is the total magnetic field, which can differ significantly from the applied field due the screening effects. Combining the Maxwell equations with (2.3) we get

$$\frac{\partial B}{\partial x} = \mu_0 j_{\text{s}} = \mu_0 j_{\text{c}} \sin\Theta. \tag{2.18}$$

Differentiating (2.16) with respect to x and substituting in (2.18) a differential equation for Θ is obtained

$$\frac{\partial^2\Theta}{\partial x^2} = \frac{1}{\lambda_{\text{J}}^2}\sin\Theta \tag{2.19}$$

where $\lambda_{\text{J}} = \sqrt{\phi_0/2\pi\mu_0 j_{\text{c}} d_{\text{eff}}}$ is the Josephson penetration depth. For a typical junction, λ_{J} is of the order of 1 to 1000 µm [33]. The general solution of (2.19) is complicated but the solutions can be described qualitatively using the similarity to the equation governing a pendulum. When $\Theta \ll 1$, and (2.19) reduces to

$$\frac{\partial^2\Theta}{\partial x^2} = \frac{\Theta}{\lambda_{\text{J}}^2} \tag{2.20}$$

and has exponential solutions decaying with λ_{J}. (2.20) has the same form as the first London equation (1.4) and represents a screening current solution similar to the Meissner effect. The main difference is that while the London penetration depth depends on the superconducting parameters, the Josephson penetration depth has no explicit dependence on the superconductors. If the weak link is much wider than λ_{J}, then it can completely screen out fields lower than a critical field value of $B_{\text{c}} = 2\mu_0 j_{\text{c}}\lambda_{\text{J}}$.

2.6 Negligible screening

If the junction's lateral dimensions are smaller than λ_J, the magnetic screening is negligible. This corresponds to $\lambda_J \to \infty$ in (2.19). In this case the net magnetic field is equal to the applied external field $B = B_{ext}$. If a uniform external field is applied in the y-direction, then from (2.16)

$$\Theta = \Theta_0 + 2\pi \frac{B d_{eff}}{\phi_0} x \tag{2.21}$$

provided the junction is also uniform and d_{eff} is a constant. The value of Θ_0 is chosen in a way to minimise the free energy of the junction and hence maximise I_c, which is achieved by $\Theta_0 = \pi/2$ for symmetric junctions. j_c is influenced by impurities and the interface quality but usually the variations from these sources are negligible and j_c can be assumed to be uniform as well. Substituting these into (2.17) we get an integral for I_c that only depends on the junctions geometry

$$I_c = j_c \iint \cos\left(2\pi \frac{B d_{eff}}{\phi_0} x\right) \mathrm{d}x\mathrm{d}y. \tag{2.22}$$

(9.5) is analogous to the diffraction integral of a wave passing through an aperture. In this analogy I_c is equivalent of the amplitude of the waves and B is equivalent of the position on the screen. $I_c(B)$ follows the Airy pattern in circular junctions and the Fraunhofer pattern in rectangular junction

$$I_c = wLj_c \frac{\left|\sin\left(\pi B L d_{eff}/\phi_0\right)\right|}{\pi B L d_{eff}/\phi_0} = I_0 \left|\mathrm{sinc}\left(\pi\phi/\phi_0\right)\right| \tag{2.23}$$

where L is the dimension of the junction in the x-direction and w in the y-direction and $\phi = BLd_{eff}$ is the magnetic flux through the junction (Fig 2.3). The absolute value of the integral is taken because I_c is defined to be positive. I_c goes to zero when the junction contains a whole number of flux quanta and current flowing forwards cancels the current flowing backwards. The maxima of the lobes of the Fraunhofer pattern decreases as ϕ^{-1}. The quantum interference in a single Josephson junction was first experimentally observed by Rowell in 1963 [26].

In case j_c is not uniform, the integral is more complicated and $I_c(B)$ deviates from the patterns discussed above. (9.5) can be used to predict the $I_c(B)$ pattern from $j_c(x,y)$ and find the critical current distribution from $I_c(B)$. An example for this is the effect of a small random fluctuation in j_c, which lead to non-zero minima in $I_c(B)$ [34]. The residual critical current is proportional to the mean-square of the fluctuations and decreases with the dimension of

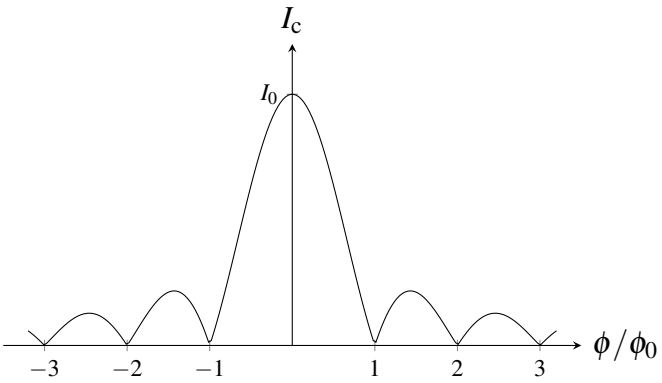

Fig. 2.3 The $I_c(\phi)$ curve of a rectangular junction follows the Fraunhofer pattern.

the inhomogeneities. Further examples for relating $I_c(B)$ ot $j_c(x,y)$ are given by Barone and Paterno [35].

Chapter 3

Fundamentals of magnetism

Magnetism is the field of physics that studies magnetic ordering of materials. Many types of magnetic ordering exists such as ferromagnetic, antiferromagnetic, ferrimagnetic, helimagnetic for example. The magnetic phase transition can be of various order but in most cases a phenomenological approach similar to the one discussed in Section 1.1 can be applied. In this chapter we summarise the basic ideas of magnetism and outline the framework used in the next chapters and discuss the properties of Ho and Dy.

3.1 Molecular magnetism

In this section we present a molecular theory for magnetism originally proposed by Heisenberg [36]. In this model, we assume that the material is made up of small magnetic dipoles that can orient themselves independently of each other. These dipoles are normally the atoms or electrons of the material and the magnetic moment often called spin. Heisenberg proposed that the potential energy between two atomic dipoles with spins $\boldsymbol{S}_1$ and $\boldsymbol{S}_2$ can be written as

$$E_{\mathrm{p}} = -J\boldsymbol{S}_1 \cdot \boldsymbol{S}_2 \tag{3.1}$$

where J is the exchange energy, the energy associated with flipping one of the moments to point in the opposite direction. If J is positive, E_{p} is minimal when the two magnetic moments are aligned with each other leading to ferromagnetism whereas materials with negative J prefer antiferromagnetic order, where the spins ordered in alternating directions.

For a lattice of dipoles the same idea can be extended but the potential energy needs to be summed over all pairs of dipoles. Including the contribution from the external magnetic field,

total free energy of the system is

$$E_{\mathrm{p}} = -\sum_{\mathrm{i,j}} J_{\mathrm{i,j}} \boldsymbol{S}_{\mathrm{i}} \boldsymbol{S}_{\mathrm{j}} + g\mu_{\mathrm{B}} \sum_{\mathrm{i}} \boldsymbol{S}_{\mathrm{i}} \cdot \boldsymbol{B} \tag{3.2}$$

where g is the gyromagnetic ration and μ_{B} is the Bohr magneton. This is a many-body problem that cannot be solved analytically without any further approximations, although it is easy to see that the energy minimum still corresponds to the parallel alignment of all spins if the exchange energy is positive between any two dipoles. If the thermal energy $k_{\mathrm{B}}T$ is much larger than J, the thermal fluctuations dominate and the alignment of the dipoles is random. On the other hand, when the thermal energy is much below the dominant J values, magnetic ordering happens.

Summing over all pairs of atomic dipoles is computationally cumbersome. The equations can be simplified by noticing that E_{p} depends on the ith spin linearly, which allows us to factor out $\boldsymbol{S}_{\mathrm{i}}$. In this case the net effect of the other spins is equivalent of an external magnetic field. This field can be expressed in terms of the average spin $\bar{S}$ and the number of nearest neighbours z using the *mean field approximation*

$$E_{\mathrm{mf}} = g\mu_{\mathrm{B}} \sum_{\mathrm{i}} S_{\mathrm{i}}(h + B) \tag{3.3}$$

where h is the field experienced by the individual spins, often called the *exchange field*

$$h = -\frac{1}{g\mu_{\mathrm{B}}} \sum_{\mathrm{j}} J_{\mathrm{i,j}} S_{\mathrm{j}} \approx \frac{\bar{S} z J}{g\mu_{\mathrm{B}}}. \tag{3.4}$$

and S_{i} is the component of $\boldsymbol{S}_{\mathrm{i}}$ parallel to $\boldsymbol{B}$. The mean field approximation for ferromagnetism is also known as Weiss theory after Pierre Weiss who first published it in 1907 [37]. The approximation assumes that the fluctuations from $\bar{S}$ are small and that the energy only depends on the relative alignment of the spins, otherwise $\boldsymbol{S}_{\mathrm{i}}$ could not be factored out. h is proportional to the total magnetisation of the material (M) as both of them depend linearly on $\bar{S}$ so $h = \lambda M$. The advantage of the mean field theory is that the total free energy is the sum of single particle energy contributions, which allows us to write down the partition function (Z) and calculate the total magnetisation by minimising Z. The calculations lead to following equation between the normalised variables $m = M/M_{\mathrm{s}}$, $t = T/\Theta_{\mathrm{C}}$ and $b = B/\lambda M_{\mathrm{s}}$

$$m = \frac{2S+1}{2S} \coth\left(\frac{3}{2}\frac{2S+1}{S+1}\frac{m+b}{t}\right) - \frac{1}{2S}\coth\left(\frac{3}{2}\frac{1}{S+1}\frac{m+b}{t}\right) \tag{3.5}$$

where $M_s = ng\mu_B S$ is the saturation magnetisation, n is the number of dipoles in the lattice, S is the spin of each dipole and Θ_C is the Curie temperature given by

$$\Theta_C = \frac{g\mu_B(S+1)\lambda M_s}{3k_B} = \frac{S(S+1)zJ}{3k_B} \tag{3.6}$$

Both Θ_C and h are proportional to J therefore both the exchange field and the exchange energy can be easily estimated from the Curie point, which is easy to measure. (3.5) can only be solved numerically but plotting both sides offers some insight into the form of the solution (Fig 3.1). When $b = 0$ and $t > 1$ the only solution is $m = 0$ however, when $t < 1$ there are also finite solutions (one of them minimises Z the other one maximises it). Therefore the magnetic ordering happens at Θ_C in zero field when the gradient of the two sides of (3.5) are equal at $m = 0$. At low temperature ($t \approx 0$) or in a high magnetic field ($b \to \infty$), when the thermal fluctuations are negligible compared to the magnetic and exchange interactions ($k_b T \ll J$ or $k_b T \ll \mu_b B$), the solution is $m = 1$ so the saturation magnetisation is achieved. The energy required to flip an atomic dipole ($2JS + \mu_B B$) is much grater than the thermal energy ($k_B T$) so all the spins stay aligned. Fig 3.1 shows numerical solutions as a function of temperature for multiple field values.

M is continuous but not smooth at Θ_C meaning the transition is second order like the superconducting transition. Therefore the Landau theory is applicable to magnetism as well and many of the derivations in Section 1.1 hold if ψ is substituted with M.

When a magnetic field is present, M is finite at all temperatures. When $m + b$ is small, the right-hand side of (3.5) can be approximated from the Taylor expansion to find the magnetic susceptibility above Θ_C

$$\chi = \frac{\mu_0 M}{B} = \frac{\mu_0}{\lambda}\frac{\Theta_C}{T - \Theta_C}. \tag{3.7}$$

χ diverges at Θ_C and decreases inversely with the temperature difference.

The mean field theory provides a good approximation for the magnetic ordering. For $J > 0$ it explains the basic properties of ferromagnetism and the $J < 0$ case can be used to describe ferrimagnetism and antiferromagnetism. The theory is valid for any exchange interaction that only depends on relative alignments of the spins.

3.2 Origins of the magnetic coupling

In the previous section we presented how a general exchange interaction can lead to the formation of magnetic order below the Curie point. If the interaction was purely magnetic, J would be approximately $\mu_0 \mu_B^2 / 2\pi r^3$, where μ_0 is the vacuum permeability and r is the

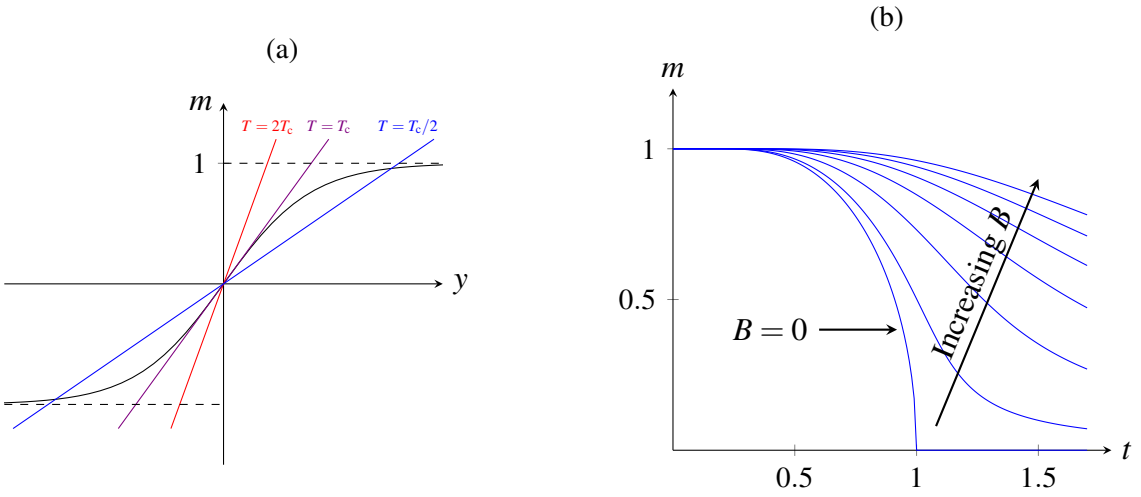

Fig. 3.1 The magnetisation in the Heisenberg model. (a) shows the graphical interpretation of (3.5) for spin-half system ($S = 1/2$) at zero field with $y = m/t$. At temperatures above Θ_C (red line) the only solution is $m = 0$, whereas for $T < \Theta_C$ there are two solutions with finite magnetisation, one of which corresponds to the maximum and the other one to the minimum depending on the direction of the field. The intercept at $m = 0$ is a saddle point. (b) shows the solution to (3.5) as a function of temperature for multiple field values. In zero field there is a sharp increase of magnetisation at Θ_C. In finite field the magnetisation is always finite.

distance between the two dipole [38]. This is much smaller than the experimentally observed exchange field in some materials and could only lead to magnetic ordering below 1 K. Ferromagnetism has been observed far above room temperature as well so the magnetic dipole interaction is not enough to explain the magnetism in these materials. The microscopic process resulting in the interaction between the atomic spins can vary from material to material. The three most common origins of exchange coupling are discussed in this section.

3.2.1 Localised spins

Let us consider a lattice of localised spins, where each site has one or more atomic orbitals that overlap slightly with neighbouring orbitals. Because of the overlap of orbitals from neighbouring sites, "hopping" is allowed, i.e. the electrons can move to neighbouring sites providing a way for interaction between sites.

For simplicity, let us intuitively consider the interaction between two electrons from two neighbouring sites. Electrons are fermions, therefore the overall wavefunction of these two electrons must be antisymmetric. If the spins of the electrons are in one of the three triplet configurations, which are all symmetric under electron exchange, the spacial wavefunction must be antisymmetric. Similarly, the antisymmetric spin singlet state requires a symmetric

spacial wavefunction. The antisymmetric spacial wavefunction must have a nod between the two sites leading to an increase in the average distance between the two electron and a lowering of the electrostatic repulsion. Therefore the spin singlet state has higher Coulomb energy than the triplet states. The singlet state has zero total spin whereas the triplet states have a total spin of 1 meaning that the parallel alignment of neighbouring spins is energetically more favourable.

John Hubbard formalised the arguments above using the second quantisation notation [39]. He wrote down the corresponding Hamiltonian which has six eigenvectors: three of which corresponding to the triplet states, one to the singlet states and the other two corresponds to the two electrons being localised on either one of the sites. When the Coulomb repulsion of two electrons on the same site (U) is much higher than the hopping term between the two sites (t), $U \ll t$, the doubly occupied states are practically unreachable energetically and the exchange coupling is the energy difference between the singlet and triplet states, which simplifies to $J = 4t^2/U$.

This process is called *direct exchange* as the interaction happens between nearest neighbours. In some materials the interacting spins are separated by other sites and the interaction is mediated by the atom in between. This process is called *super exchange* and was developed by Anderson to explain the antiferromagnetism in MnO [40]. The exact form of the exchange energy depends on details of the exchange but it is proportional to t^4 as opposed to t^2 because the electron needs four hops to interact with the electron on the other site and get back where it started.

The Hubbard model explains the exchange coupling in terms of Coulomb interactions and hopping terms, which can produce interactions strong enough for Θ_C above room temperature. It assumes that the spins are localised and the interaction between spins is via hopping between sites so it is most applicable for magnetic insulators such as MnO and NiO.

3.2.2 Itinerant ferromagnetism

In transition metals the d-electrons are delocalised over the whole lattice and the Hubbard model is not applicable to describe their magnetic behaviour. Stoner considered the rise of the exchange field from the point of view of the density of states [41]. Delocalised electrons can be described occupying the band states. In a non-magnetic metal the band structure has equal number electrons with each spins but in some metals spontaneous spin polarisation occurs.

Let us consider the effect of moving small number of electrons (δn) from the spin down band to the spin up band at $T = 0$ when all states are occupied below the Fermi energy (E_F) and all states are empty above (Fig 3.2). Taking the electrons with energies between $E_F - \delta E$

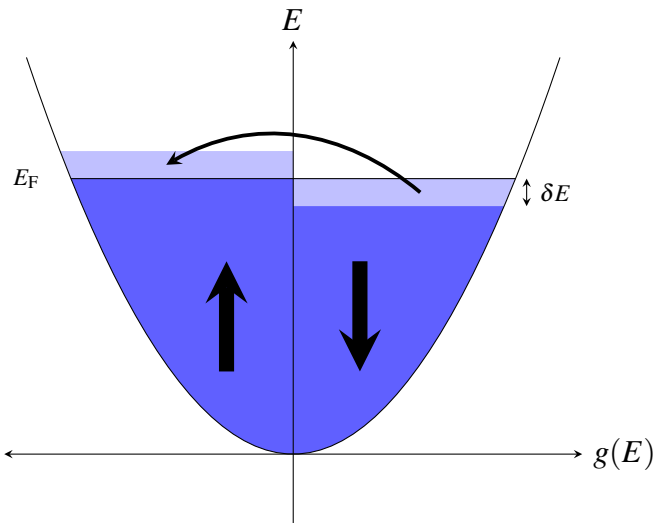

Fig. 3.2 Density of states in the Stoner model. Some electrons from the top of the spin-down band are moved over to the spin-up band

and E_F from the spin down band and placing them on top of the spin up band creases their energies by δE. The number of electrons transported is $\delta n = g(E_F)\delta E/2$, where $g(E_F)$ is the density of state at the Fermi energy. So the kinetic energy of the system increased by $\Delta E_{kin} = g(E_F)(\delta E)^2/2$.

The potential energy decreases due to Coulomb interaction. Electrons with opposite spin can occupy the same states and therefore increase the Coulomb energy. Moving some electrons over decreases the level of double occupation and hence the potential energy by $\Delta E_{pot} = -U(g(E_F)\delta E)^2/2$, where U is the Hubbard U given by

$$U = \iint \mathrm{d}^3\boldsymbol{r}\mathrm{d}^3\boldsymbol{r}' \frac{e^2}{4\pi\varepsilon_0|\boldsymbol{r}-\boldsymbol{r}'|}\left|\psi(\boldsymbol{r})\right|^2\left|\psi(\boldsymbol{r}')\right|^2, \tag{3.8}$$

The total change in energy is $\Delta E = \Delta E_{kin} + \Delta E_{pot} = (1 - Ug(E_F))g(E_F)(\delta E)^2/2$. If $\Delta E < 0$ moving electrons from one spin state to the other is energetically favourable so the condition for the spontaneous ferromagnetism to be stable is

$$Ug(E_F) > 1 \tag{3.9}$$

which is known as the *Stoner criterion*. The case of finite temperature can be treated similarly by including the Fermi-Dirac distribution to take into account the effect of thermal excitations.

Itinerant ferromagnetism typically occurs in transition metals, such as Fe, Co, Ni, where the magnetisation arises from the conduction electrons. In certain alloys of transition metals, like NiFe, the density of states have different shapes for up and down spins leading to

$g_\uparrow(E_\mathrm{F}) \neq g_\downarrow(E_\mathrm{F})$. These materials have higher Θ_C as moving electrons from the narrower band to the wider band require smaller increase in kinetic energy.

3.2.3 Indirect exchange

Many rare earth metals show very strong magnetic ordering at low temperatures. The magnetic moment per atom measured in experiments correlate strongly with the total spins of the electrons on the f-orbitals suggesting that the magnetism does not originate from the delocalised electrons. However, f-orbitals are very localised and the overlap between adjacent atoms is insignificant so direct exchange is unable to give rise to ferromagnetism. The magnetic order, therefore, must the result of an indirect exchange.

Rare earths have the highest magnetic moment per atom among the elements due to the unpaired electrons on their f-orbitals. The magnetic field from the atoms partially polarises the delocalised electron cloud in the vicinity of the atom. The polarised electrons can then interact with the neighbouring atoms mediating the exchange interaction between the magnetic moments.

The exchange coupling can be derived by considering the magnetic response of an electron gas to a magnetic field at zero temperature. Using perturbation theory, it can be shown a plane wave magnetic field in the form of $H(\boldsymbol{r}) = H_\mathrm{q}\cos(\boldsymbol{q}\cdot\boldsymbol{r})$ gives rise to a similarly oscillating magnetisation of the electron cloud

$$M(\boldsymbol{r}) = M_\mathrm{q}\cos(\boldsymbol{q}\cdot\boldsymbol{r}) = \chi_\mathrm{q} H_\mathrm{q}\cos(\boldsymbol{q}\cdot\boldsymbol{r}) = \chi_\mathrm{P} f\left(\frac{q}{2k_\mathrm{F}}\right) H_\mathrm{q}\cos(\boldsymbol{q}\cdot\boldsymbol{r}) \tag{3.10}$$

where

$$f(x) = \frac{1}{2}\left(1 + \frac{1-x^2}{x}\ln\left|\frac{x+1}{x-1}\right|\right) \tag{3.11}$$

and $\chi_\mathrm{P} = \mu_0\mu_\mathrm{B}^2 g(E_\mathrm{F})$ is the Pauli susceptibility [42]. In the limit of $q = 0$, $\chi_\mathrm{q} \to \chi_\mathrm{p}$ which is the magnetic response of the free electron model to a uniform applied field. The susceptibility drops down quickly over $2k_\mathrm{F}$ and even goes negative as shown in Fig 3.3a. This is a consequence of sharp drop in occupation above the Fermi energy. The electron cloud is ineffective in screening perturbations that oscillate faster than the electrons states with the highest available energies.

As the response in (3.10) is linear, the magnetisation induced by an arbitrary external field can be deduced by taking the Fourier transform of the magnetic field and multiplying it with χ_q. Therefore the real space magnetisation will be the convolution of $H(\boldsymbol{r})$ and the

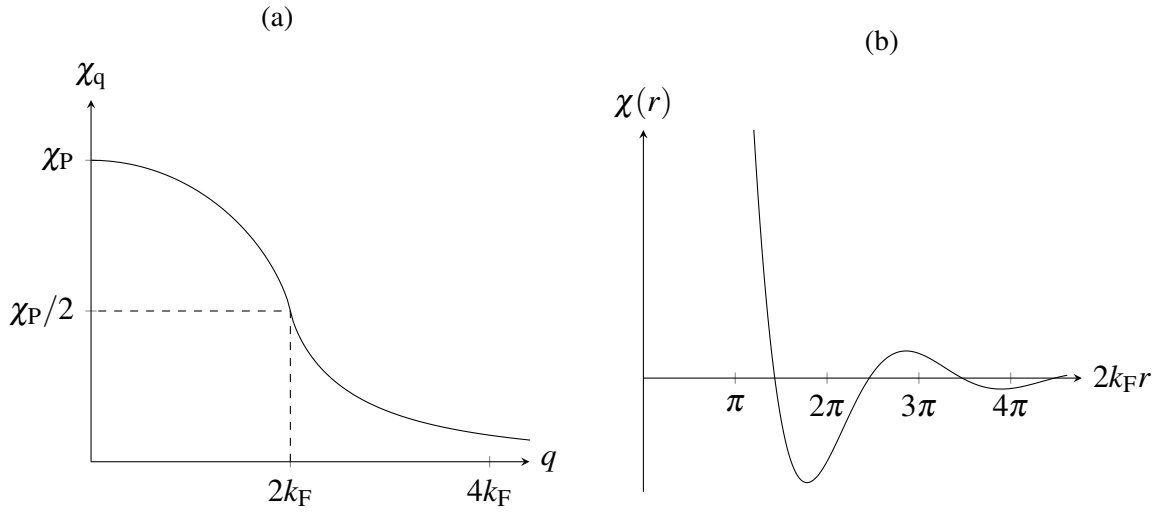

Fig. 3.3 The magnetic susceptibility of the conduction electrons as a function of wave vector (a) and in real space (b). χ_q drops down sharply at Fermi wave number as the screening is inefficient at short wave lengths. $\chi(r)$ changes signs and persist over a long distances.

real-space susceptibility, which is

$$\chi(\boldsymbol{r}) = \frac{2k_F^3\chi_P}{\pi}\frac{\sin(2k_Fr) - 2k_Fr\cos(2k_Fr)}{(2k_Fr)^4}. \tag{3.12}$$

The interaction between the conduction electrons and the atomic dipoles is local and proportional to the magnetisation of the electron cloud at the position of the dipole. Therefore the exchange coupling between atoms is proportional to $\chi(r)$ (plotted in Fig 3.3b) and strongly depends on the separation between the sites. In large distances $J \propto \cos(2k_Fr)/r^3$, which can lead to interactions over much longer range than direct exchange. It can also change sign so the depending on the separation between atoms it can lead to ferromagnetic or antiferromagnetic coupling. It can be used to change the coupling between thin magnetic layers by adjusting the spacer thickness between them. The interaction is often called the Ruderman-Kittel-Kasuya-Yosida (RKKY) coupling after the people who derived it and explained the magnetism of rare earth elements with it [43–45].

The above calculations were carried out for $T = 0$. At finite temperatures there are occupied states above the Fermi surface and the electrons are more effective at screening shorter oscillations. As temperature increases χ_q gets more spread out and therefore $\chi(r)$ is more localised and the RKKY coupling is shorter range. At very high temperatures, the electrons can screen any wavelength and the magnetisation of the electron cloud will be

proportional to the inducing field everywhere meaning that there is no coupling between atomic dipoles.

An important property of the RKKY coupling that it leads to much lower spin-polarisation of the conduction electrons than the spontaneous spin polarisation typical for transition metals. The magnetisation of the electron cloud induced by the magnetic moments of the atoms (m) fluctuates but its maximum value can be estimated as $M \sim \chi_{\mathrm{P}} m/4\pi r^3$, where r is the atomic radius. The magnetisation is proportional to the spin-polarisation $P = (n_\uparrow - n_\downarrow)/(n_\uparrow + n_\downarrow) = M/\mu_{\mathrm{B}} n = 3\mu_0 \mu_{\mathrm{B}} m/4\pi r^3 m_{\mathrm{e}} v_{\mathrm{F}}^2$. Substituting in values for Ho, who has the highest atomic moment, the spin-polarisation is $P \approx 1 \times 10^{-5}$. This is negligible compared to the spin-polarisation in transition metals, where it can be as high as 90 % [46].

3.3 Magnetic structure of Holmium and Dysprosium

In Part III superconducting structures with Ho and Dy are discussed so we shall have a look at their magnetic structure in further detail. Both of them are rare earth elements and the RKKY coupling is responsible for their magnetic ordering. As all lanthanoids, they are paramagnetic at room temperature but at lower temperatures they show a rich magnetic phase diagram including helical and conical magnetic structures.

3.3.1 Helimagnetism

In the previous sections we saw how nearest neighbour interactions can give rise to ferromagnetism and antiferromagnetism although more complex magnetic structures also exist. Most rare earth metals have a helical or spiral phase, where the magnetic moments in each atomic layer are parallel to each other but the magnetisation direction rotates from one plane to the next (Fig 3.4a). Helimagnetism can only be understood if the next nearest neighbour interactions are also taken into account. If α is the rotation angle between the planes and J_1 and J_2 are the exchange coupling between the nearest-neighbour and second nearest-neighbour planes, the energy of the interaction is

$$E_{\mathrm{ex}} \propto -J_1 \cos\alpha - J_2 \cos 2\alpha. \tag{3.13}$$

If $J_1 > 0$ and $J_2 > 0$, $\alpha = 0$ minimises E_{ex} and we returned to the ferromagnetic case. In general E_{ex} is minimal when

$$\frac{\partial E_{\mathrm{ex}}}{\partial \alpha} \propto J_1 \sin\alpha + 2J_2 \sin 2\alpha = 0 \tag{3.14}$$

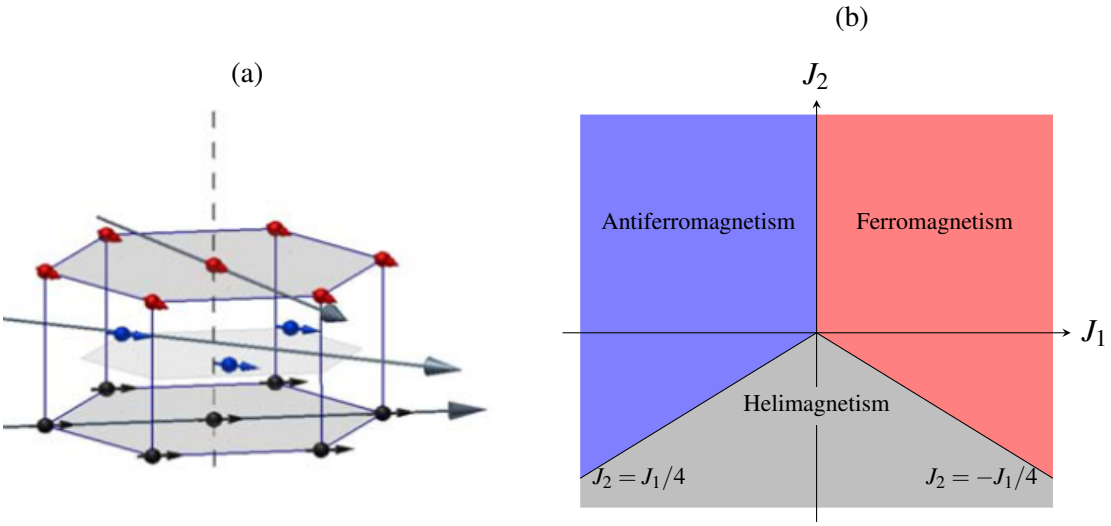

Fig. 3.4 (a) Illustration of the helimagnetic order. (b)The phase diagram for the model with nearest-neighbour coupling J_1 and next-nearest-neighbour coupling J_2

so when

$$\cos\alpha = -\frac{J_1}{4J_2} \qquad \text{or} \qquad \sin\alpha = 0 \tag{3.15}$$

From these conditions we find that if $J_1 > 0$ and $J_2 > -J_1/4$, $\alpha = 0$ and the ferromagnetic order is stable, if $J_1 < 0$ and $J_2 > J_1/4$, $\alpha = \pi$ and the system is antiferromagnetic, and finally if $J_2 < -\left|J_1/4\right|$, E_{ex} is minimal for $0 < \alpha < \pi$ resulting in helimagnetism (Fig 3.4b). When $J_2 \ll J_1$, the above derivation gives back the ferromagnetic and antiferromagnetic results from Section 3.1.

The RKKY coupling is long range and can change sign over distance therefore it can give rise to helimagnetic structures. The temperature affects the RKKY exchange energies because the thermal fluctuations weaken the spin polarisation of the electron cloud and because the lattice spacings change with temperature. Therefore, most rare earth metals have a rich magnetic phase diagram including helimagnetic and ferromagnetic phases as well.

3.3.2 Holmium

Ho has atomic number 67 with electron configuration [Xe]$4f^{1}16s^{2}$. Because of the high number or unpaired electrons on its f-orbitals it has an atomic magnetic moment of $10.34\mu_{\text{B}}$, which is the largest among the elements [38]. Ho has a hexagonal closed-packed (hcp) lattice structure.

As most rare earth elements, Ho has multiple magnetic phase transitions. It becomes helimagnetic at $\Theta_{\text{N}} = 133\,\text{K}$ with a rotation angle of $\alpha = 50°$ around the c-axis. Decreasing

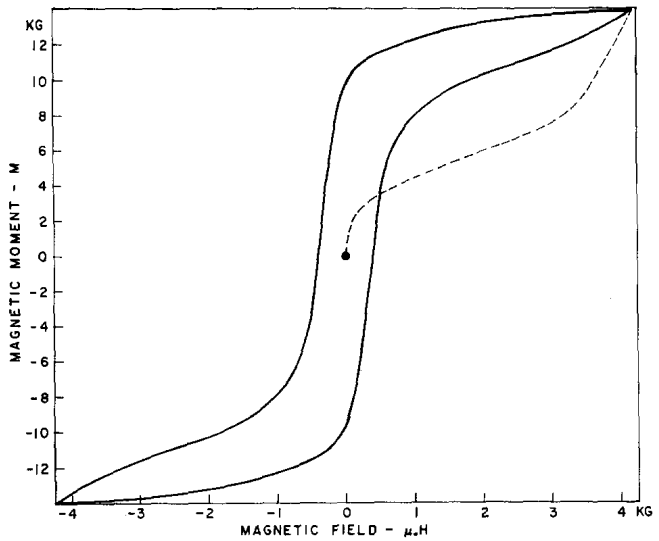

Fig. 3.5 Ho $M(H)$ curve measured at 4.2 K. H is applied perpendicular to the axis of the magnetic spiral. The virgin curve exists the hysteresis loop indicating the presence of the magnetic spiral. The graph is adopted from [50].

the temperature, the rotation angle decreases to 35° at 4.2 K. The magnetisation (M) also develops an out-of-plane component below $\Theta_C = 20$ K. However, the ferromagnetic component can easily be suppressed by strain and has not been observed in thin films [47, 48].

When an external field (H) is applied to Ho single crystals at 4.2 K, the magnetic spiral gradually distorts and unwinds to a ferromagnetic state. In small fields the distortion of the spiral is reversible, but a remnant ferromagnetic component develops in larger fields. Once the magnetisation is saturated, Ho remains ferromagnetic indicating that the spiral magnetic structure is metastable at low temperatures. The magnetisation process of Ho at low temperatures was studied extensively using neutron diffraction in [49].

The $M(H)$ curves also show signatures of the presence of the spiral state in Ho at low temperatures. The magnetisation curve of the virgin state exits the hysteresis loop of the fully magnetised ferromagnetic state (Fig 3.5). This can be understood by considering the magnetisation process again. As the magnetic spiral is metastable and has zero net magnetisation, M only increases slowly until H is large enough to unzip the spiral. Due to the energy barrier between the helimagnetic and ferromagnetic states, the field required to unzip the spiral is larger than the coercive field, which shows as the virgin curve going outside the hysteresis loop. A detailed examination of Ho $M(H)$ loops and their comparison to neutron scattering results is found in [50].

3.3.3 Helimagnetic-ferromagnetic transition

The simple explanation presented in Section 3.3.1 is insufficient to explain the irreversible helimagnetic-ferromagnetic transition and the third-nearest-neighbour interaction is also need to be considered. Ignoring the out-of-plane magnetisation, (3.13) modifies to

$$E_{\text{ex}} \propto -J_1 \cos\alpha - J_2 \cos 2\alpha - J_3 \cos 3\alpha. \tag{3.16}$$

By differentiating E_{ex} with respect to α, it can be seen that E_{ex} has three local minima when $J_2^2 > 3J_1J_3(J_1 - 3J_3)$. One of them is at $\alpha = 0$ and corresponds to the ferromagnetic state and the other two are the opposite of each other and correspond to the helimagentic state. The $E_{\text{ex}}(\alpha)$ curves are plotted for a range of J values in Fig 3.6.

Let us consider cooling our system from well above the transition to the helimagnetic state. Slightly above Θ_{N}, only J_1 and J_2 are significant and E_{ex} only has two minima symmetrical to 0 (blue curve). At Θ_{N} the thermal energy is equal to the energy lowering of these minima and the magnetic spiral forms. As the temperature lowers further, the range of the RKKY coupling increases and the value of J_3 also becomes significant resulting in lowering of the central peak (green curve). At even lower temperatures, J_3 is larger leading to a third minimum at $\alpha = 0$. If J_3 is large enough, the minimum at $\alpha = 0$ becomes the global minimum (purple curve) but the system cannot transition because of the energy barrier between the two minima, hence the helimagnetic state is metastable.

Applying an external magnetic field favours parallel alignment of the atomic spins therefore it increases the value of J_1 in relation to J_2 and J_3 (red curve). The external field lowers the energy of the ferromagnetic state as well as the energy barrier between the states until $\alpha = 0$ is the only minimum (orange curve). If $\alpha = 0$ is the global minimum in zero field, the ferromagnetic order is stable and persists when the external field is removed. If the external field increased only until the energy barrier is comparable to the thermal energy, a fraction of the system can transition into the ferromagnetic state resulting in a remnant ferromagnetic component when the field is removed. This simple model can illustrate the magnetic phase transitions observed in Ho, although detailed calculations based on the detailed Fermi-surface are needed to compute the magnetic phase diagram of Ho.

3.3.4 Dysprosium

Many properties of Dy are similar to Ho as they are adjacent elements in the periodic table. Dy has an atomic number of 66 and one fewer electrons on its f-orbitals than Ho. The atomic magnetic moment of Dy is $10.20\mu_{\text{B}}$, which is just slightly smaller than in Ho. Dy

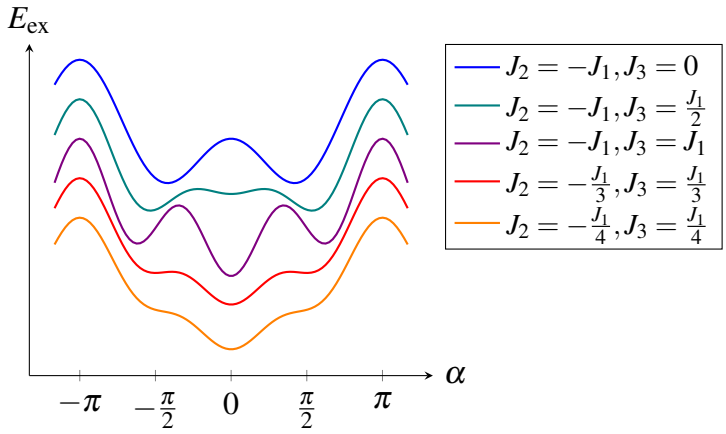

Fig. 3.6 Model for the helimagnetic-ferromagnetic transition. The $E_{ex}(\alpha)$ curves are vertically displaced for readability and normalised for comparison. At Θ_N the energy minimum is at a non-zero angle so the spiral state is stable (blue curve on top). As the temperature lowers a local minimum appear as at zero angle (green curve) and gradually grows until it becomes the global minimum (purple curve). The energy barrier between the minima prevents the spontaneous transition to the ferromagnetic state. An external magnetic field lowers the energy barrier (red curve) until it disappears and the system transitions into the ferromagnetic state (orange). When the magnetic field is removed, the system remains ferromagnetic as it is lower in energy.

also has a helimagnetic phase between 179 and 85 K with the rotation angle decreasing from 43° to 25° with temperature. Below 85 K Dy is ferromagnetic with its moment lying in the basal plain. The reported values for Θ_C and Θ_N vary slightly depending on the measurement technique and the crystal quality [51–55].

3.3.5 Ho-Dy alloys

Both Ho and Dy has a hexagonal closed-packed (hcp) lattice structure and they form a solid solution when alloyed together. Few studies have been done on the magnetic structure of Ho-Dy alloys using neutron diffraction and these results are summarised in [51]. The spiral phase has been observed for a temperature range in all compositions. The Neél temperature (Θ_N) varies linearly with the composition between the Neél temperature of Dy and Ho. The Curie temperature decreases quickly with Ho content and the ferromagnetic phase was not observed for Ho content above 25 % at 4.2 K, although there is a lack of data for compositions between 25 and 50 % Ho content.

Chapter 4

S/F structures

Superconductivity and ferromagnetism promote opposite spin ordering as discussed in the previous chapters so they tend to compete with each other. This competition can lead to novel phenomena when both states are present in the proximity of each other. Ferromagnetism is normally more stable than superconductivity because the energy gain per atom at the magnetic transition is approximately $k_B\Theta_C$ from (3.6) where as at the superconducting transition it is $\sim (k_B T_c)^2/E_F$ and $T_c < \Theta_C < E_F$ normally. Therefore the effect of the ferromagnet on the superconductor is more significant than the other way around. For this reason most research on S/F heterostructures focuses on the changes in S although there have been a few theoretical predictions and experimental observations implying that a superconductor can influence the domain size of an adjacent F layer and it can also couple F layers if placed between them [56, 57]. In this chapter we discuss the theoretical background ferromagnetic proximity effect and the generation of long-range triplet superconductivity, and review recent experiments on a few S/F heterostructures including magnetic Josephson junctions and superconducting spin valves.

4.1 Proximity effects in ferromagnets

The exchange field of the ferromagnet tries to align all magnetic moments. This leads to a quick dephasing and breaking of the Cooper pair entering a ferromagnetic material and the superconducting wave function decays much faster in ferromagnetic materials than in normal metals. If the spin-up direction is defined to be along the exchange field(h), the energy of the spin-up electrons lowers while the energy of the spin-down electrons increases. To compensate for this the spin-up electrons increase their kinetic energy while the spin-down electrons decrease, which results in the Cooper pairs acquiring a net momentum of $2\delta k_F = 2h/v_F$ so ψ oscillates with period $\pi v_F/h$.

We can use the Ginzburg-Landau formalism to get a simple picture of the proximity effect in a ferromagnet [58]. For a normal metal we used (1.8) to understand the decay of ψ close to the interface. To explain the experimental results for ferromagnetic proximity measurements, the second derivative term also needs to be included resulting in an equation in the form of

$$a\psi + b\nabla^2\psi + c\nabla^4\psi = 0 \tag{4.1}$$

where a, b and c are parameters that depend on the temperature and the exchange field. With the boundary conditions that $\psi = \psi_0$ at the interface and $\psi \to 0$ far from the interface, the solution for uniform boundary takes the form of

$$\psi(x) = \psi_0 e^{-\mathrm{k_1 x}}\cos(k_2 x) \tag{4.2}$$

where $k_1^2 + k_2^2 = b/a$ and $k_1^2 k_2^2 = c/a$. This means that the order parameter oscillates inside a ferromagnetic layer.

For more complex systems, the Usadel equation can be extended to magnetic materials as well by replacing ω with $\omega + ih$ in (1.24). Averaging the normal Green functions over the Fermi surface, we arrive to the linearised Usadel equation

$$\left(|\omega| + ih\,\mathrm{sgn}(\omega) - \frac{\hbar D}{2}\frac{\partial^2}{\partial x^2}\right) F(x,\omega) = \Delta(x) \tag{4.3}$$

In the F region $\Delta(x) = 0$ and normally $k_\mathrm{B}T_\mathrm{c} \ll h$ so the Matsubara frequency term can be neglected giving a simple second order differential equation

$$ih\,\mathrm{sgn}(\omega)F_\mathrm{f} - \frac{D}{2}\frac{\partial^2 F_\mathrm{f}}{\partial x^2} = 0. \tag{4.4}$$

The boundary conditions (1.26) are also applicable to S/F interfaces as long as $h \ll E_\mathrm{F}$. This criterion is satisfied for rare earth metals where the exchange field is generated by the RKKY coupling and h is relatively small. Under the boundary conditions the anomalous functions are complex exponentials therefore the order parameter has a damped oscillatory behaviour in the ferromagnet

$$\psi \sim \sum_\omega F_\mathrm{f}(x,\omega) \sim \Delta e^{-\mathrm{x}/\xi_\mathrm{f}}\cos\left(x/\xi_\mathrm{f}\right) \tag{4.5}$$

where $\xi_\mathrm{f} = \sqrt{\hbar D_\mathrm{f}/h}$ is the coherence length in F. Therefore we recovered the same oscillatory behaviour as from the Ginzburg-Landau formalism. The length scales of the oscillation

and the decay are the same because diffusion and elastic scatterings dominate the electron transport.

In the clean limit ($\xi_f \ll l$), the Usadel equation is not valid and another approach is needed. It can be shown that the oscillations are still present but the decay is non-exponential

$$\psi \sim \frac{1}{x} e^{-x/\xi_{1f}} \sin(x/\xi_{2f}), \tag{4.6}$$

where the two length scales are $\xi_{1f} = \hbar v_F / 2\pi k_B T$ and $\xi_{2f} = \hbar v_F / 2h$ [58]. The oscillations are governed by the exchange field and the decay is determined by the pair breaking of the Cooper pairs due to thermal fluctuations. Because usually $\xi_{1f} \gg \xi_{2f}$, close to the interface the decay is $\sim 1/x$, which is much slower than in the dirty limit. Unsurprisingly, the range of the proximity effect in ferromagnetic materials is longer in the clean limit than in the dirty limit, however, typically they are both shorter than in nonmagnetic metals.

The self-consistency equation (1.25) provides a way to predict T_c for S/F structures and hence connect the theoretical calculations of the anomalous Green functions to measurable quantities. The general method for S/F structure is solve the Usadel equation for the relevant boundary conditions for the system and use (1.25) to find T_c^*. This method has formed the basis of many theoretical calculations for multilayer structures investigating the effect of the layer thicknesses and interface transparency. One of the main predictions of these calculations is the non-linear dependence of the critical temperature on the F layer thickness (d_f) [59, 60]. The oscillations are due to the system switching between the 0 phase (ψ does not change sign in the F layer) and π phase (ψ changes sign in the F layer). Experimental observations confirmed this prediction first in Nb/Gd multilayers [61] and later in Nb/CuMn [62], Nb/Co [63] multilayers and Fe/Nb/Fe [64], Fe/Pb/Fe [65], Fe/V/Fe [66] trilayers as well as in Nb/Ni [67] bilayers. The theory suggests that the T_c oscillations quickly disappear with increasing interface transparency implying the importance of sample preparation. A demonstration of this effect is that the magnetron sputtered Nb/Gd multilayers show clear T_c oscillation with the Gd thickness [61], while similar structures grown with molecular beam epitaxy show step like decrease of T_c [68].

It is important to emphasise that the Usadel equation is only valid for weak ferromagnetic materials ($h \ll E_f$) as in strong magnetic materials the Green functions oscillate on the atomic length scale and our approximations break down. Rare earth metals, where the magnetism arises from the RKKY coupling, are ideal for testing predictions based on the Usadel equation due to their relatively low exchange energy.

4.1.1 Andreev reflection at S/F interfaces

As discussed in Section 1.3.2, electrons are reflected back as holes with opposite spin and vice versa on the S/N interfaces. This process is strongly spin dependent and involves both spin bands. In metals where the density of state for spin-up and spin-down electrons are unequal, Andreev reflection is suppressed and the interface resistance is increased. When the ferromagnet is fully polarised Andreev reflection is prohibited and the normal-supercurrent conversion is only possible via other dissipative processes. Spin-polarisation lowers the transparency of the interface (t, the fraction of the incoming electrons transmitted through the interface) and can decrease the interaction between the S and F layers. This is typical for transition metal ferromagnets where the origin of the magnetism is the spin imbalance among the delocalised electrons. In rare earth metals the magnetism originates from the spins of the ions in the lattice and the spin-polarisation of the conduction band is negligible so the interface transparency is only dependent on the Fermi energy mismatch and impurities at the interface.

4.2 π junctions

In the previous section, it was shown that ψ oscillates in a ferromagnetic layer. It is possible to design Josephson junctions with a ferromagnetic barrier, called π *junctions*, such that the phase shift across the junction is π instead of 0. The π phase shift corresponds to a change of sign in ψ and can be thought of as the junction having negative I_c. As the sign of ψ depends on convention, it cannot be measured so the basic properties of π junctions are the same as that of 0 junctions discussed in Chapter 2. However, if a π junction is inserted in a superconducting loop, ψ need to change along the superconducting wires connecting the two sides of the junctions resulting in supercurrent flowing through the circle [69]. Therefore, supercurrent is flowing in the ground state of a ring containing a π junction as opposed to a 0 junction, where the ground state has zero current. Moreover, the magnetic field dependence of the transport critical current of SQuID circuits containing π junctions shifted by half period compared to normal superconducting rings. Both the ground state current and the shift in the magnetic response has been measured in superconducting rings with π junctions [70–72].

The phase shift across the junction is determined by the thickness of the junction, the exchange field, the temperature and the transparency of the interfaces. It was shown theoretically that I_c displays damped oscillations as a function of thickness and exchange field with the minima corresponding to the 0 to π transitions and the temperature dependance is also non-linear [73, 74]. The critical thickness where the 0-π transition occurs (d_c) decreases with

temperature [32]. The first unambiguous demonstration of the existence of π junctions was done by observing the 0-π transition as a function of barrier thickness in $Nb/Cu_xNi_{1-x}/Nb$ Josephson junctions. [75]. The experiments used weak ferromagnets because d_c is normally around ξ_f, as seen from (4.5) and (4.6), or even lower in the case of low transparency. In strong ferromagnets, ξ_f is normally on the order of the lattice parameters and the oscillations can be washed out by the thickness fluctuations.

Considering (2.1), the phase difference Θ that minimises the free energy is either 0 or π depending on the sign of F_0. A more general expressions for the free energy take into account higher harmonics and allow for other values of Θ to minimise F and make the 0-π transition continuous. Theoretical calculations for different types of S/F/S junctions show that even in the presence of second and higher harmonic terms in (2.1) the transition is still discontinuous [76–78].The only effect of this extra terms is to prevent I_c from vanishing at d_c [73, 79]. There have been theoretical proposals suggesting that if the magnetic barrier thickness is exactly d_c the thickness fluctuations can create small regions with 0 and regions with π phase difference that could average out to an intermediary phase difference but this has not been experimentally realised [80, 32].

4.3 Triplet Cooper pairs

In conventional superconductivity, the superconductive gap field is isotropic and independent of the direction of the momenta of the electrons. This leads to zero orbital angular momentum (s-wave) and therefore the superconductive wavefunction having a symmetric spacial part. Electrons must obey Fermi statistics meaning that their overall wavefunction must be antisymmetric under the exchange of particles so Cooper pairs must have antisymmetric spin wave functions in s-wave superconductors. There are four possible ways to combine two spins: the spin-0 singlet state and the three spin-1 states. Only the singlet state is antisymmetric which is why Cooper pairs in conventional superconductors have zero total spin.

In strongly correlated system, which is the case for many high-temperature superconductors, the attraction between electrons tend to depend on the direction of the momentum and is not uniform along the Fermi surface which leads to the anisotropy of $\Delta(\boldsymbol{k})$. The number of planes in which $\Delta(\boldsymbol{k})$ is zero equals to the orbital angular momentum of the superconducting wavefunction (l). An odd vale of l represents an antisymmetric spacial wavefunction, which would lead to triplet Cooper pairs. Non-s-wave superconductivity has been observed in many cuprate superconductors although mostly d-wave, which requires antisymmetric spin wave function also.

Triplet Cooper pairs can also be induced in ferromagnets. As discussed in Section 4.1, when a Cooper pair enters a ferromagnet, the spin-up electron gains h energy while the spin-down electron decreases in energy by h. This leads to the following time evolution of the two wave functions

$$\begin{aligned} |\uparrow\rangle_{\mathrm{t}} &= |\uparrow\rangle \times \exp(i\omega t) \qquad \langle\uparrow|_{\mathrm{t}} = \langle\uparrow| \times \exp(-i\omega t) \\ |\downarrow\rangle_{\mathrm{t}} &= |\downarrow\rangle \times \exp(-i\omega t) \qquad \langle\downarrow|_{\mathrm{t}} = \langle\downarrow| \times \exp(i\omega t) \end{aligned} \tag{4.7}$$

where $\omega = h/4\pi\hbar$.Using the Dirac notation the singlet and the triplet states can be written as

$$\begin{aligned} \Psi^{\mathrm{s}} &= \langle\uparrow|\downarrow\rangle - \langle\downarrow|\uparrow\rangle \\ \Psi^{\mathrm{t}}_0 &= \langle\uparrow|\downarrow\rangle + \langle\downarrow|\uparrow\rangle \\ \Psi^{\mathrm{t}}_{+1} &= \langle\uparrow|\uparrow\rangle \\ \Psi^{\mathrm{t}}_{-1} &= \langle\downarrow|\downarrow\rangle \end{aligned} \tag{4.8}$$

Therefore the time evolution of the spin states of the Cooper pairs are

$$\begin{aligned} \Psi^{\mathrm{s}}(t) &= \langle\uparrow|\downarrow\rangle \times \exp(i\omega t) - \langle\downarrow|\uparrow\rangle \times \exp(-i\omega t) \\ &= \Psi^{\mathrm{s}} \cos(\omega t) + \Psi^{\mathrm{t}}_0 i \sin(\omega t) \\ \Psi^{\mathrm{t}}_0(t) &= \langle\uparrow|\downarrow\rangle \times \exp(i\omega t) + \langle\downarrow|\uparrow\rangle \times \exp(-i\omega t) \\ &= \Psi^{\mathrm{t}}_0 \cos(\omega t) + \Psi^{\mathrm{s}} i \sin(\omega t) \\ \Psi^{\mathrm{t}}_{+1}(t) &= \Psi^{\mathrm{t}}_{+1} \\ \Psi^{\mathrm{t}}_{-1}(t) &= \Psi^{\mathrm{t}}_{-1} \end{aligned} \tag{4.9}$$

Substituting $t = x/v_{\mathrm{F}}$, the time dependence can be easily converted into spacial variation. This oscillation is the same as that we observed in Section 4.1 but now we see that the Cooper pairs oscillate between the Ψ^{s} and Ψ^{t}_0.

Ψ^{t}_0 has total spin 1 with 0 component in the z-direction, which is chosen to be along the exchange field. It is a combination of both spin state so it decays in a ferromagnetic material at the same rate as Ψ^{s}. If the direction of h changes, the Cooper pairs will have a finite spin component in the direction of the exchange field. This way Ψ^{t}_0 can be converted to Ψ^{t}_1. As (4.9) shows, Ψ^{t}_1 is not oscillating in the ferromagnetic material and insensitive to the pair breaking process of the exchange field [81, 82]. The usual decay length of Ψ^{t}_1 is normally $\xi_{\mathrm{n}} = \sqrt{\hbar v_{\mathrm{F}} l/6\pi k_{\mathrm{B}} T}$ in the dirty limit and $\xi_{\mathrm{n}} = \hbar v_{\mathrm{F}}/2\pi k_{\mathrm{B}} T$ in the clean limit. Both length scales are much longer than ξ_{f} so the process is often called *long-range triplet conversion*. It has been shown that any magnetic inhomogeneity at the S/F interface can induce the triplet conversion [83].

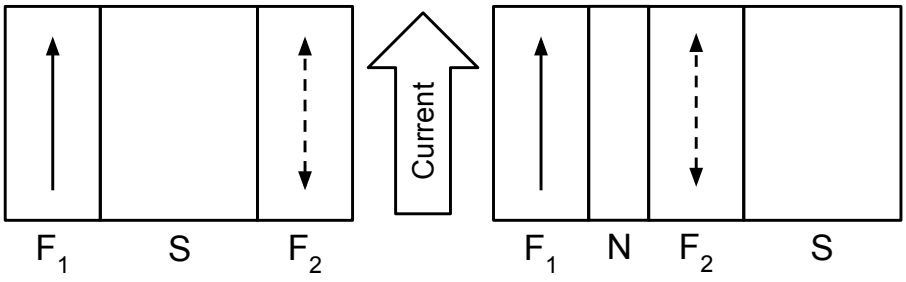

Fig. 4.1 The two most common SSV structures: F/S/F (left) and F/F/S (right). The arrows indicate the directions of the magnetisations of the F layers. In both cases F_1 is pinned or harder to switch, while F_2 is the free layer. Often a normal metal layer is placed between the F layers to decouple them and allow them to switch independently. Unlike in classical spin valves, the current flows along the layers indicated by the arrow in the middle.

The first experimental evidence of long range triplet generation was in magnetic CrO_2 Josephson junctions [84]. Supercurrent was observed to survive hundreds of nm in CrO_2, which is much longer than the expected range based on its ferromagnetic coherence length. The source of inhomogeneity generating the triplets is slightly unclear in this experiment but assumed to be due to impurities at the interface. More recent works either use multiple independent magnetic layers or intrinsically inhomogeneous magnetic materials like Ho to generate long range triplet pairs [85, 86].

4.4 Superconducting spin valves

Superconducting spin valve (SSV) are another trilayer structure commonly used in this field. They are similar to classical spin valves, that are often used in hard-drive readout heads and whose resistance can be controlled by an external field. The main difference is that while in classical spin valves the resistance is controlled through the number of tunnelling channels, the SSV effect is based on the suppression of the S layer by the adjacent F layers. The two main structures for SSVs, F/S/F and F/F/S, are illustrated in Fig 4.1. The proximity effect and hence the suppression of T_c varies with the relative alignment of the two F layers therefore if the temperatures is held between the maximum and minimum T_c, the superconducting phase can be turned on and off by changing the magnetisation of F. However, the exact physics is different for metallic ferromagnets and ferromagnetic insulators (FI). Some of the key SSVs experimetns are summarised in Table 4.1.

Table 4.1 Overview of superconducting spin valve experiments.

Type	Structure	ΔT_c/mK	Source
FI/S/FI	Fe_3O_4/In/Fe_3O_4	2400	[87]
	EuS/Al/EuS	>500	[88]
	GdN/Nb/GdN	1750	[57]
F/S/F	FeNi/In/Ni	200	[89]
	CoO/Py/Al_2O_3/Al/Al_2O_3/Fe	44	[90]
	Fe/V/Fe	30	[91]
	Ni/Nb/Ni	41	[92]
	CuNi/Nb/CuNi	6	[93, 94]
F/F/S	Ho/Nb/Ho	400	[95]
	Co/Cu/Py/Cu/Nb	120	[96]
	CoO/Fe/Cu/Fe/Pb	50	[97]

4.4.1 SSVs with ferromagnetic insulators

The first theoretical consideration of the F/S/F structures comes from de Gennes [31]. He considered SSVs with ferromagnetic insulators (FI) in the limit of $T \ll T_c$. In these systems the Cooper pairs cannot penetrate the FI layers so only the average exchange field $\tilde{h}$ experienced by he Cooper pairs influences T_c

$$\tilde{h} = h\frac{a}{d_s}\cos(\theta/2). \tag{4.10}$$

where h is the exchange field in the FI layers, a is the lattice parameter, d_s is the thickness of the S layer and θ is the angle between magnetisation of the two FI layers. The description only works when d_s is smaller than the coherence length of the superconductor. de Gennes derived that the presence of the exchange field suppresses the condensation energy (E_c), which is the difference between the normal phase energy (E_n) and the energy of the superconducting state ($E_s(\theta)$), which now depends on θ

$$E_c = E_s(\theta) - E_n = N(0)\left[-\frac{\Delta^2}{2} + \tilde{h}^2(\theta)\right] \tag{4.11}$$

where N(0) is density of states in the condensate at 0 K. This shows that if $h(0) > \frac{1}{2}\Delta$ the superconducting state is destroyed for some range of θ. If this is the case, the superconducting phase can be turned on and off by changing the relative alignments of the FI layers. The superconducting spin valve effect for ferromagnetic insulators was experimentally con-

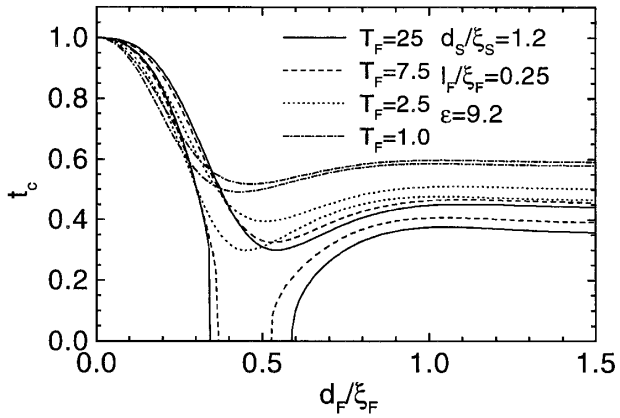

Fig. 4.2 The reduced temperature, $t_c = T_c/T_{c0}$, as a function of the reduced thickness of the ferromagnetic layers for a set of different interface transparency. For each curve style the higher curve corresponds to the AP state and the curve below to the P state. (Adopted from [99])

firmed soon after [87, 89] and more recently FI/S/FI structures were proposed for electronic applications [88, 90].

4.4.2 Metallic SSVs

In de Gennes' theory, the Cooper pairs only interact with the F layers through the interfaces. In metallic SSVs this assumption is unrealistic as Cooper pairs can enter F for ξ_f. The Usadel equation is commonly used to analyse metallic SSVs. Buzdin *et al.* considered metallic spin valves with perfectly transparent interfaces [98]. He studied the parallel (P, $\theta = 0$) and antiparallel (A, $\theta = \pi$) alignments and showed that the change decreases with increasing d_s, which agrees with de Gennes' findings. Tagirov examined the effect of the interface transparency [99]. His main results are summarised in Fig 4.2. The figure shows that for low transparency, when most of the electrons are reflected from the surface, there is hardly any change in T_c but for highly transparent interfaces the difference in T_c between AP and P (ΔT_c) can be much larger even up to $0.3T_c$, although this is still smaller than the prediction for FI SSVs. Tagirov also predicts that ΔT_c is the largest when the thickness of the F layers is around $0.4\xi_f$. For Nb, whose T_c in bulk is 9.2 K, this would mean a change of several K in the absolute transition temperatures of the AP and P states.

The experimental values are, however, significantly lower than the theoretical predictions, especially in transition metals [94, 93, 100, 92, 90, 101, 91, 97]. ΔT_c in spin-valves with transition metals is below 100 mK because the high spin polarisation suppresses the Andreev reflection and hence the proximity effect as well. Because the phase transition of the

superconducting layer is spread out over a temperature range comparable to ΔT_c, only a few of them achieves infinite magnetoresistance [91, 97]. In some cases inverse spin valve effects were reported, where $T_c^{AP} < T_c^{P}$ [100, 101]. This implies that for transition metal SSVs factors other than the exchange field also influence T_c. Theoretical calculations show that Cooper pairs leaking into the F layers also suppress T_c and can be responsible for the inverse spin valve effect [102]. The model also shows that the minimum T_c corresponds to the orthogonal alignment and not the P nor AP alignments due to the formation of triplet Cooper pairs. This effect was experimentally observed in Fe/Fe/Pb and Co/Py/Nb SSVs [97, 96].

As Table 4.1 show FI SSVs have higher ΔT_c than transition metal SSVs although rare-earth metals like Ho and Dy show promising properties. Ho/Nb/Ho and Dy/Nb/Dy spin valves were reported to have $\Delta T_c \approx 400\,\mathrm{mK}$ [95]. This is significantly higher than the values reported for transition metals and comparable to the properties of ferromagnetic insulators. Experiments suggest that the interface is crucial for SSVs and in systems where the Andreev reflection is suppressed, like in transition metals, ΔT_c is much smaller.

Part II

Experimental techniques

Chapter 5

Film growth and junction fabrication

The magnetic spiral of Ho rotates around the crystallographic c-axis. In polycrystalline or randomly oriented samples the behaviour of the helimagnetic state averages out therefore oriented samples are required to study the magnetic spiral. The crystallographic orientation of materials is determined by the sample preparation processes. In this chapter, we summarise the sample preparation techniques - including DC magnetron sputtering, optical lithography and focused ion beam microscopy - used in this work.

5.1 DC magnetron sputtering

All films are grown with DC magnetron sputtering, which is a form of Physical Vapour Deposition (PVD). All PVD techniques create a physical vapour phase and the atoms or molecules in the vapour diffuse towards and deposit onto the substrate without undergoing any chemical reaction. PVD is suitable for growing thin films with uniform thickness and low roughness.

The difference between the PVD techniques is the way the vapour phase is created. In case of sputtering the vapour phase is created by a glow discharge or plasma. At the start of the deposition the chamber is filled with a few Pa of sputtering gas, Ar is commonly used because it easily ionises. To start the plasma, several hundred volts of DC voltage is applied across the chamber to ionise the Ar gas. The large electric field accelerates the created electrons towards the anode and the Ar ions towards the cathode. The accelerated electrons and ions collide with neutral atoms and ionise them creating more charged particles. To maintain the plasma the number of charged particles neutralising at the cathode and the anode has to be the same as the number of charged particles being created in collisions. Both the higher pressure of the plasma gas and the longer distance between the cathode and anode increases the number of collisions and hence the number of new charged particles generated.

Using an electron beam or filament emitting electrons can generate more ions and stabilise a plasma at lower pressure. Electron sources are often used in plasma etching.

In sputtering, a plate of the source material, called the *target*, is placed on the cathode. The heavy positive ions bombard the target and knock off atoms or clusters of atoms creating the physical vapour. There are many possible processes happening on the surface of the target. including emission of sputtered atoms and secondary electrons, reflection et cetera. The average number of target atoms sputtered on the impact of an Ar ion depends on various parameters such as temperatures and mass, but it is approximately proportional to the energy of the incoming ions and hence the voltage between the electrodes. As the Ar ions carry charge, the number of incidences is proportional to the electric current flowing through the cathode. Therefore the sputtering rate, the number of atoms sputtered per unit time, is proportional to the electric power of the process $P = IV$.

The number of incidences and therefore the sputtering rate can be enhanced by using magnetic electrode, called *magnetrons*. The magnetic field traps light charged particles, mainly electrons, on a cycloidal path leading to more collisions and charged particle generation near the cathode. Deposition rates achieved by magnetron sputtering is typically an order of magnitude higher than other sputtering techniques [103].

If DC voltage is applied, there is a constant charge transfer between the electrodes. The accumulating charge on the cathode and the anode counteract the applied voltage and eventually stops the plasma unless the charge is depleted. Therefore DC sputtering is only efficient with conducting targets, typically metals. Radio frequency sputtering or pulsed laser deposition can be used to grow insulating thin films.

Once the sputtered atoms enter the vapour phase, they scatter around in the chamber and deposit on the walls and the substrate. The transport has no angular dependence as gravity is negligible compared to the kinetic energies of the atoms so the deposition rate (deposited atoms per area per time) decreases inversely with the square of the distance from the target.

The gas pressure has a complex effect on the deposited films. If the pressure is low the incidence rate at the cathode is also low resulting in a slow deposition rate. The sputtered particles have high kinetic energy when leave the target. In low pressure the mean free path of the sputtered particles is long and if it is comparable to the distance between the target and the substrate, particles do not thermalise and crash into the substrate with high energy leading to intermixing and lattice defects. High sputtering pressure decreases the efficiency of sputtering hence lowers the sputtering rate and can increases the amount of impurities deposited in the films. Therefore there is an optimal gas pressure which needs to be calibrated for the system and the material especially for high purity oriented films [104].

5.1.1 Depositions

A-plane sapphire ($11\bar{2}0$) substrates are used in this work because it promotes the growth of Nb (110) over the other orientations [105] and the c-orientation of Ho and Dy grow epitaxially on Nb (110) due to the small lattice mismatch of about 2 % [106]. The substrates are cut into 5 mm×5 mm and 5 mm×10 mm pieces with a dicing saw and cleaned with acetone and isopropanol for 10 min in an ultrasonic bath.

A photograph of the flange used for the depositions is shown on Fig 5.1. The substrates are placed on the Ta strip, which can be heated by passing a current through. There are three magnetrons on the flange allowing three targets to be sputtered without breaking vacuum. They are separated by metal sheets to prevent cross-contamination during deposition. The middle magnetron, which holds the Nb target, is situated right above the sample holder 68 mm higher. The other two are placed 70 mm out on each side of the heater, 100 mm away from the substrates. The magnetrons are isolated which makes it possible to apply different powers to each of them. Each magnetron has their own shutter, which can be closed independently so deposition from different targets can be started or stopped independently even without turning the plasma off.

In order to achieve high purity, the chamber is kept in ultra-high vacuum. It is pumped with a diffusion pump and baked with a heater strip wrapped around the chamber for at least 8 hours before each deposition. During deposition, the walls are cooled with liquid nitrogen so the remaining gases, especially water, freeze out from the gas space. With this procedure base pressure below 10^{-6} Pa and water partial pressure below 10^{-7} Pa are achieved (verified using an in-site residual gas analyser).

The substrates are heated to 900 °C for the Nb seed layer and the heating is lowered to 650 °C for the consecutive rare earth layers as suggested by Nakahara *et al.* [106]. The temperature of the heater is allowed to stabilise by waiting for 30 min before deposition. The Ar pressure is set around 8 Pa when igniting the plasma and decreased to 1.60 ± 0.05 Pa for the depositions. The targets are presputtered for 10 min at high power and for 3 min at the sputtering power with the shutters closed to allow the plasma to reach a steady-state and to clean any oxidation from the surface of the targest.

5.1.2 Growth rate and temperature calibration

The deposition rates are calibrated for every material by a simple lift-off method. An about 1 mm-wide line is drawn with a marker pen on the substrate and an approximately 100 nm-thick layer is deposited on top of it at room temperature without liquid nitrogen cooling. The liquid nitrogen cooling lowers the base pressure and removes impurities, and

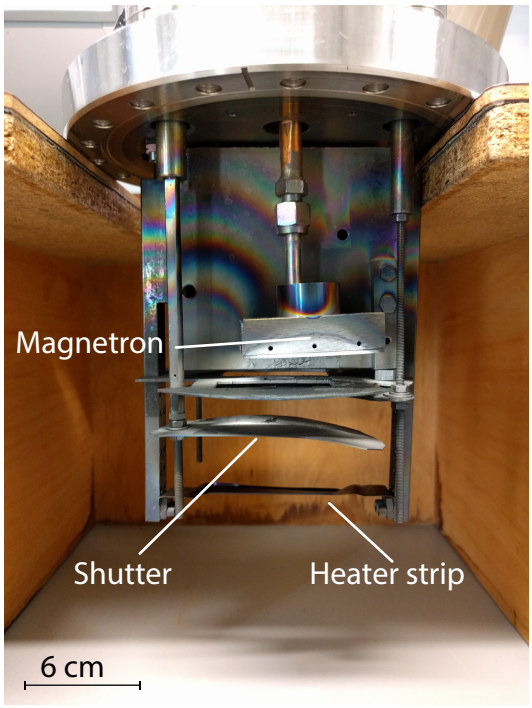

Fig. 5.1 Photograph of the flange used in the depositions.

heating promotes the epitaxial growth so neither changes the deposition rate significantly. For the calibration of the Ho and Dy growth rate, 10 nm Nb base and capping layers are also deposited to prevent oxidation. After deposition the samples are cleaned with acetone in an ultrasonic bath. The acetone dissolves the ink from the marker and removes the deposited layer above it. Measuring the step height at the edge gives the thickness of the layer from which the deposition rate is obtained.

The step height is measured by both a Dektak profilometer and an atomic force microscope (AFM). The height profile is taken along 2000 µm-long line perpendicular to the step edge with the profilometer. Using the AFM, a 30 µm×30 µm scan of the edge was taken at different positions on both sides of the line (Fig 5.2). AFM gives high accuracy measurements in a small area and the Dektak is able to measure the height profile over a longer distances, but with a higher noise level. The step height was measured at five different positions and the deposition rates are calculated from the average and error from the standard deviation of the values. Both techniques agreed on the step sizes within the margin of error and the deposition rates were found to be $\Gamma_{\mathrm{Nb}} = 3.0 \pm 0.2\,\mathrm{nm\,min^{-1}}$ for Nb, $\Gamma_{\mathrm{Ho}} = 3.9 \pm 0.2\,\mathrm{nm\,min^{-1}}$ for Ho and $\Gamma_{\mathrm{Dy}} = 3.6 \pm 0.2\,\mathrm{nm\,min^{-1}}$ for Dy at 10 W.

The temperature of the heater strip is controlled by a current passing through it. The heater strip is calibrated on a flange with a glass window using a pyrometer. The substrate temperatures suggested by Nakahara *et al.* [106] are achieved using 38 and 24 A.

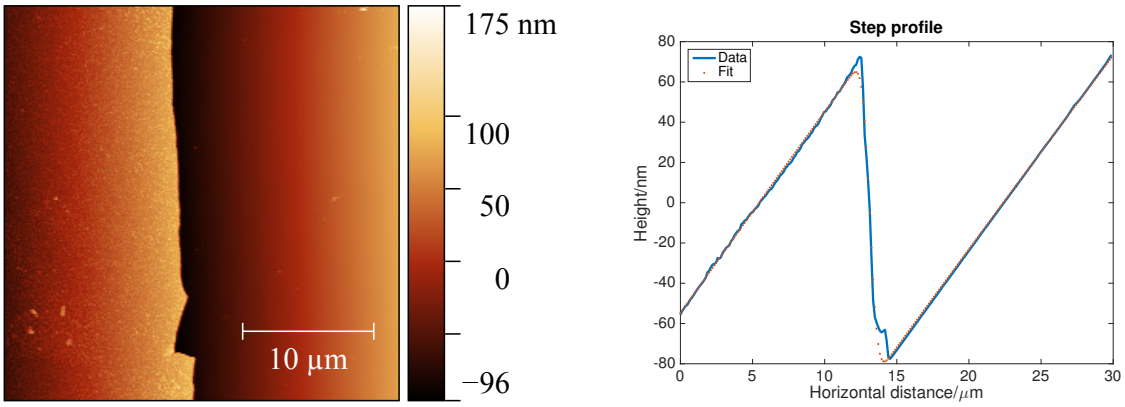

(a) (b)

Fig. 5.2 (a) example of an AFM scan at the edge of the step. (b) the step profile from averaging the height along the step. A Heaviside step function is fitted to the profile to obtain the step height.

5.2 Optical lithography

Optical lithography is a technique widely used in microfabrication and in semiconductor physics [107]. A thin layer of photosensitive polymer is deposited on top of the sample and is exposed to light through a mask that protects parts of the resist. The UV light changes the chemical structure of a positive resist such that it becomes more soluble in the areas exposed to light. These areas are removed by the developer agent and the same pattern is left as the pattern on the mask. Negative photoresists become more resistant to the developing agent resulting in the negative image of the mask being left on the sample. After developing, the sample can be etched or deposited on to achieve the desired structures. The process is illustrated in Fig 5.3.

To fabricate nanopillar Josephson junctions, 4-µm-wide wires are patterned on the sputter deposited films using optical lithography. The patterns are etched into the films using Ar plasma milling creating a 4 µm-wide wire with 18 pads connected to different points allowing 4-point measurements on 7 sections of the wire.

5.3 Focused ion beam etching

The basic principle of a focused ion beam microscope (FIB) is the same as scanning electron microscopy (SEM) but the secondary electrons used for the imaging are the result of bombarding the surface with ions instead of electrons. Many different ion sources are possible but liquid gallium sources are used most commonly because Ga has a low melting

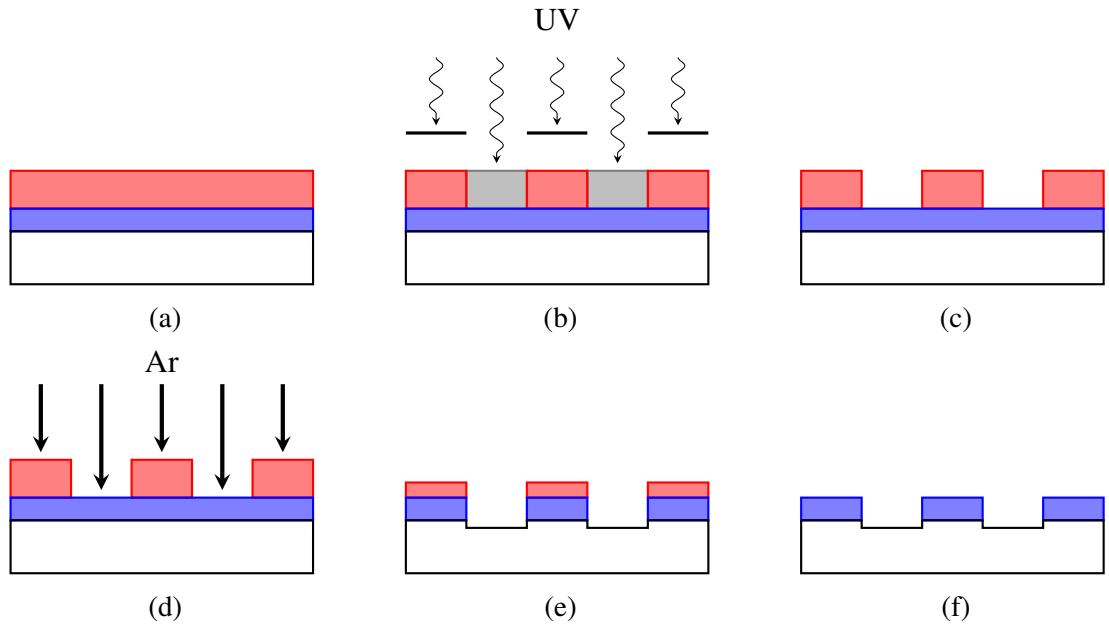

Fig. 5.3 Schematic diagram of the optical lithography process: (a) spin coating the resist (red) on the sputter deposited film (blue), (b) UV exposure through the mask, (c) developing, (d) Ar ion etching, (e) after milling, (f) final pattern.

point and not very reactive [108]. Also, Ga is molten for a wide temperature range, which makes operation easier. Ga^+ ions are extracted from the molten reservoir and accelerated through the column. The beam is shaped and focused on the sample by a series of electrostatic lenses and apertures. Besides using the secondary electrons from the impact of Ga^+ ions, the ion beam can be used to etch the sample if the current and the beam energy is increased. The etching process resembles the sputtering process or plasma etching but the etched area is much smaller in FIB therefore it is significantly slower. The main advantage of FIB etching over other lithography techniques is that it requires no mask and it can be tailored to the sample. FIB is ideal to finish and refine sub-micron features after the larger scale structures have been created.

After patterning 4 µm-wide tracks from the Nb/Ho/Nb films using optical lithography and Ar ion milling, the nanopillar Josephson junctions are fabricated as described in [109–111]. The track is narrowed to about 500 nm along a 2 µm path with a 100 pA beam. The high current beam can implant significant amount of Ga near the edges so the edges were cleaned with a 10 pA beam leaving a wire 200 to 400 nm in width.

The sample is mounted on a holder in a way that allows it to be rotated so the Ga beam is at 85° to the normal of the substrate. Two 100 nm-wide incisions are made 300 to 700 nm apart such that one of them cuts down to the bottom third of the wire and above and the

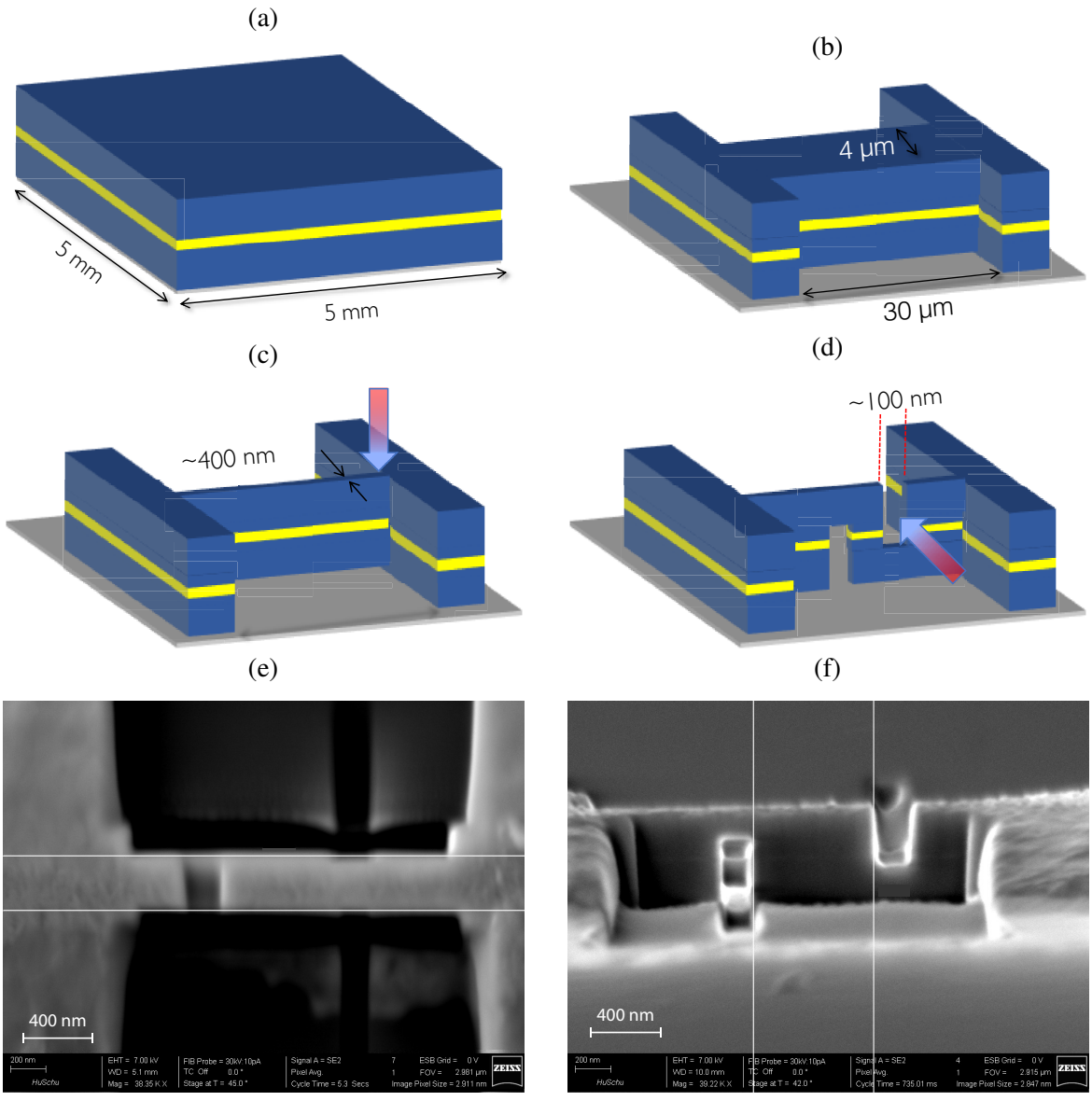

Fig. 5.4 Diagrams of the junction fabrication process (a-d) and SEM micrographs of the nanopillar Josephson junctions from the top (e) and from the side (f) after FIB fabrication.

other incision cuts the bottom two thirds leaving a superconducting bridge on the top. The nanopillar created this way forces the current through the middle barrier layer creating a Josephson junction. During fabrication, the sample is monitored via an SEM and images of the structures are shown on Fig 5.4.

The advantage of this technique is to allow the fabrication of fixed cross-section junction on the sub-micron scale. FIB has the capability to make nanopillars down to 100 nm for conducting substrates. Insulating substrates, like sapphire, can accumulate charge from both the Ga beam and the electron beam, which can distort the beam and cause a shift during etching resulting in lower precision. The beam shift is experienced during the fabrication of our samples preventing the creation of nanopillars below 200 nm in dimensions.

Chapter 6

Characterisation and measurement

The crystal and magnetic structure of each layer hugely influences superconductivity so the samples are characterised using X-ray diffraction and vibrating sample magnetometry. After characterisation, the electric properties are studied at cryogenic temperatures to understand the proximity and Josephson effects in rare earth - niobium heterostructures. This chapter briefly outlines the background and specifics of these techniques used to characterise and measure bilayers and Josephson junctions.

6.1 X-ray diffraction

X-ray diffraction (XRD) is widely used to characterise the phase and crystallographic orientation of materials. The spacings between the atomic layers of a crystalline materials are comparable to the wavelength of X-ray radiation, therefore crystals act as diffraction gratings for X-ray beams. If the material is crystalline, the reflected X-ray beams interfere giving rise to a material specific diffraction pattern. The diffraction angle (2θ) for which the interference is constructive is determined by the distance (d) between crystallographic planes and the wavelength of the X-ray beam (λ) according to Bragg's law:

$$n\lambda = 2d\sin(\theta) \tag{6.1}$$

In high angle XRD measurements, or $2\theta - \omega$ scans, the X-ray source and the detector are moved simultaneously to keep the incidence angle (ω) half of 2θ (Fig 6.1). If the sample is well-oriented, one crystallographic orientation dominates throughout the sample so only peaks from the corresponding set of planes appear in the diffractogram as beams reflected from the other planes never reach the detector. Therefore the missing peaks from the diffraction pattern is a signature of well-oriented samples.

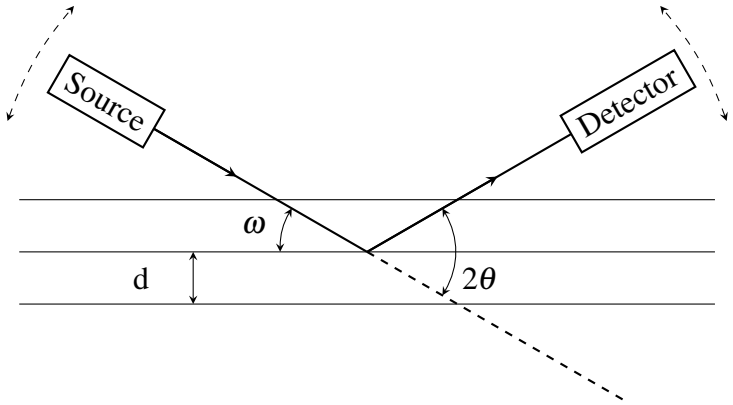

Fig. 6.1 Illustration of the XRD setup. The incident angle, the diffraction angle and the lattice spacing are labelled on the diagram.

The width of the peak also hold information about the sample. In a thick single crystal ($t \gg \lambda$, where t is the thickness) without any crystal defects measured in a perfectly narrow and perfectly collimated beam, the peaks are infinitely narrow and the full width half maximum (FWHM) is practically 0. However, in practice measurements are not perfect and there for the XRD peaks widen. Some sources of the peak broadening are instrumental like the finite size and the divergence of the beam. The other sources of the peak broadening originate in the sample such as non-uniform stress, grain boundaries and thickness. In think films the thickness, or rather the thinness, of the film is often the most important factor. When the thickness of the material is comparable to the wavelength of the X-ray, which is $\lambda = 1.54\,\text{Å}$ for Cu Kα radiation used in this work, the interference changes slowly from constructive to destructive as moving away from the diffraction angle and therefore making the peak wider. The peak widening from the thickness of the layer is given by the Scherrer formula [112]

$$\text{FWHM} = \frac{K\lambda}{t\cos\theta}, \tag{6.2}$$

where K is the shape factor, which is usually close to unity therefore in this work it is approximated as $K = 1$.

To determine the degree of epitaxy the sharpness of the peaks need to be examined with rocking curves, where 2θ is fixed at one of the peak values from the examined layer while the sample is rotated and ω is varied. This technique is similar to X-ray topography as a rocking curve is essentially a line section of an X-ray topograph. If the sample is highly epitaxial, the beams diffracted from different planes are highly coherent and they cancel each other if ω slightly differ from $2\theta/2$, therefore the peak in the ω scan is very sharp. On the other hand, if the sample is not well-oriented, layers are not perfectly parallel to each other, or there are multiple grains, the rocking curves broaden giving essentially flat rocking curves

for polycrystalline samples. Measuring the FWHM of the rocking curves gives a quantitative description of the level of epitaxy. If the FWHM is close to the value expected from the instrumental broadening estimated from the substrate peak and the thickness broadening than the sample is epitaxial. However, if the FWHM is larger than expected other broadening effects, like strain or grain boundaries, are present in the sample suggesting the sample is only highly-textured.

6.2 Vibrating Sample Magnetometry

A vibrating sample magnetometer (VSM) is used to measure magnetic properties. The VSM consists of a sample holder, a pick-up coil and an electromagnet, see in Fig 6.2a. The sampler holder vibrates the sample along the axis of the pick-up coils at a given frequency. The periodic motion of the sample induces an AC voltage in the pick-up coil according to Faraday's law. The amplitude of the induced voltage is proportional to the magnetic moment of the sample, therefore the magnetic moment of the sample can be obtained from the signal once the device is calibrated. Because the signal has the same frequency as the vibration of the sample, the background noise at any other frequency can be easily filtered out. The electromagnet can induce an external magnetic field to measure $M(H)$ curves. The changes in the external field have a much lower frequency than the vibration of the sample so it does not affect the measurement. The set-up can be used for in-plane and out-of-plane measurements as well.

All the magnetic measurements were carried out in a He fridge at 10 K. The temperature was kept above the Nb $T_c = 9.2\,\mathrm{K}$ as the signal from a superconducting layer can disturb the signal from the ferromagnetic layers. Neither Ho nor Dy has any phase transition below 10 K therefore the magnetic structure can be assumed to remain the same.

To characterise the magnetic properties of the films, the saturation magnetisation (M_s) and remnant magnetisation (M_r), and the coercive field (H_c) are obtained from the $M(H)$ loops. H_c is the field value where the magnetisation is zero therefore it is defined as the H-axis intercept of the curve. M_r is the magnetisation value in zero field, which corresponds to the M-axis intercept of the curve. M_s is the magnetisation of the fully saturated sample. Due to the slight diamagnetic background signal from the substrate and the sample holder, the saturated $M(H)$ curve is rarely flat. The value for M_s is obtained by fitting a line to the saturated region and the constant term of the line gives M_s. An example of an $M(H)$ loop for a Nb(20 nm)/$Ho_{73}Dy_{27}$(40 nm) bilayer is shown in Fig 6.2b illustrating the above definitions.

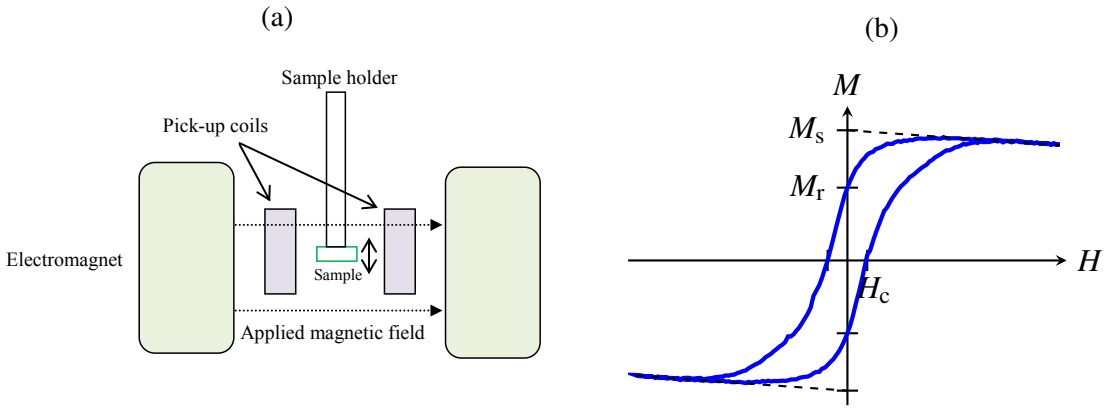

Fig. 6.2 (a) Schematic diagram of the VSM. The sample holder vibrates the sample in the middle of the pick-up coils. The changing magnetic flux from the vibrating sample induces AC voltage in the pick-up coils. The electromagnet is used to induce magnetic field in the sample space.(Adapted from [113]). (b) Illustration of the parameters of $M(H)$ loops. H_c and M_r are the intersections with the H- and M-axes. M_s is the constant term of the line fitted to the saturated region.

6.3 Electric measurements

Two types of transport measurements are carried out in this work to measure T_c for Nb/HoDy bilayers and I_c for Josephson junctions both using a 4-point configuration. In a 4-point measurement, four different contact pads are wire-bonded to four different points on the sample. The current is driven between two of these leads and the voltage is measured between the other two. Four-point measurements exclude the resistance of the probe and provide more accurate results.

6.3.1 Critical temperature

The critical temperature of films is obtained from measuring the resistance as a function of temperature ($R(T)$). The resistance is measured in a 4-point reverse-polarity measurement set-up. In a reverse polarity measurement the current is reverted at certain time intervals and the resistance is the average of the two values measured in the different polarities. This method cancels any constant potential and systematic error from temperature or chemical potential differences at the contacts and interfaces.

The temperatures is swept across the superconducting transition and T_c is defined as the temperature where the resistance is half of R_n (Fig 6.3). Fitting a suitable function, such as $\tanh(x)$, was considered to obtain T_c, although the shape of the $R(T)$ curves varies slightly between samples and the previous definition of T_c gives more consistent results than fitting.

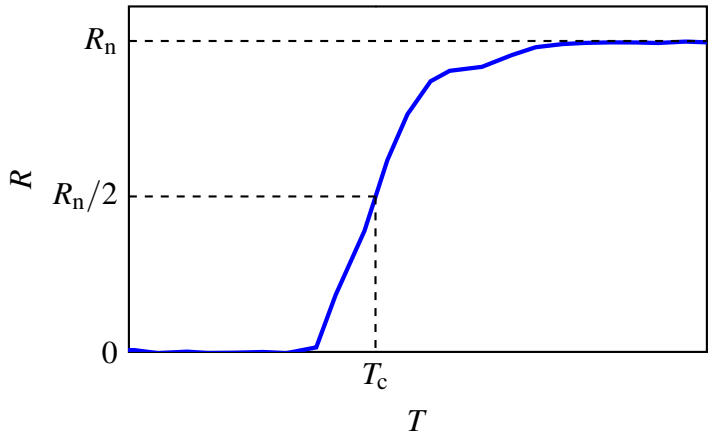

Fig. 6.3 A typical $R(T)$ curve measured in a Nb/$Ho_{80}Dy_{20}$ bilayer in zero set magnetic field showing the definition of T_c as $R(T_c) = R_n/2$.

The 4-point measurement is performed among four points in a line on the surface of the films meaning the measured value of R_n depends on the relative positions of the four points and holds little meaning by itself. The set up excludes the resistance from the probe and the contacts and is suitable for monitoring changes in resistance and measuring T_c.

The magnitude of the electric current can hugely impact critical current measurements. If the current value is too large, the superconducting state can be suppressed near T_c when the critical current density is low resulting in the measured T_c value being lower than the actual value for the film. Decreasing the current, however, lowers the signal-to-noise ratio and increases the uncertainty of the measurements. For our bilayer films the optimal current value is found to be 10 µA.

The measurements are run in a cryogenic system using He cooling. The base temperature is 1.5 K and with a built-in heater coil the temperature of the sample can be controlled. The system is chosen for its temperature stability and ability to go below 4.2 K. The system also includes an electromagnetic coil that can induce a magnetic field up to 8 T allowing T_c to be measured in magnetic field or for different magnetic histories.

6.3.2 Critical current

The electric properties of Josephson junctions are measured in a liquid He dewar at 4.2 K. A current signal oscillating at about 1 Hz is driven across the junction while the voltage across is measured in a four-point configuration providing the current-voltage IV characteristics for the junction. The oscillation frequency is far off from the Josephson frequency, which is in the GHz range, so the Shapiro effect does not affect the measurements. By fitting the

resistively shunted junction model from Section 2.3 to the *IV* characteristics, I_c and R_n values are obtained.

The amplitude of the current signal is controlled over multiple orders of magnitude using an amplifier. Due to the small cross-section of the junctions, relatively low currents in the normal state can lead to significant heating melting the junctions. To avoid destroying the nanopillars, the current is increased manually from 0 A until I_c is found. For the same reasons, extra care is taken to avoid stray currents by earthing the samples all times possible and wearing insulating gloves when handling the samples and the probe.

Using the electromagnetic coil of the probe, an external magnetic field up to 500 mT can be applied. $I_c(H)$ can be measured by slowly swiping the magnetic field. For magnetic field measurements up to 1 T, junctions are loaded into a helium fridge and $I_c(H)$ is measured at 2.5 K. The lower temperature is chosen for an temperature stability of the He fridge.

Part III

Results

Chapter 7

Proximity effects in Nb/HoDy bilayers

Many of the applications of superconductivity involves heterostructures with not only superconducting material that exploit the proximity effect [5, 114]. Even though research into the proximity effect started around 1950s, there are still missing pieces in our understanding of the phenomenon. The band gap is smaller near the interface than in the bulk of the superconductor (S) but short range superconductivity can also be induced on the non-superconducting (N) side. The suppression of superconductivity in S and the appearance of a band gap in N have been experimentally demonstrated by tunnelling density of state measurements [115–117]. A good understanding of the proximity effect is the basis of all superconducting devices.

The Eilenberg and Usadel equations provide a powerful tool to model the proximity effect. They are applicable not only to normal metals but also to ferromagnetic interfaces, where they predict an oscillating decay of the superconducting wavefunction [58]. These theories are supported by experimental measurements of density of state (DOS) oscillations in bilayers [118, 119], and the non-linear critical temperature dependence is also confirmed in S/F bilayers [67], F/S/F trilayers [66, 64, 120, 65] and multilayers [61–63].

The stronger the magnetic exchange field (h), the faster the decay and the oscillations of superconducting wavefunction are in the F layer, which can make the observation of the proximity effect difficult in strong ferromagnets. Another important factor is the spin-polarisation. High spin-polarisation suppresses the Andreev reflection leading to only a few Cooper pairs entering F. Transition metals often have significantly spin-polarised conduction bands and strong exchange fields arising from itinerant ferromagnetism, which reduces the proximity effect. In rare earth (RE) metals, on the other hand, the magnetism originates from the Ruderman-Kittel-Kasuya-Yoshida (RKKY) coupling, where the magnetic moments from the f-orbitals interact via the polarisation of the conduction electrons. Even though the RKKY coupling is propagated by the delocalised electrons, the polarisation of conduction

band in REs is negligible compared to transition metals and their exchange field is also typically an order of magnitude lower. These properties make REs ideal candidates to study the proximity effect.

One of the main consequences of the proximity effect is the suppression of T_c, which is easily measurable experimentally [121]. The T_c shift strongly depends on the type of scattering processes causing the Cooper pairs to dephase outside the superconductor but also influenced by other factors like the interface transparency and material thickness. The formation of long-range triplet pairs also lowers T_c as the triplet pairs can leak into F and weaken the superconductive condensate [102, 97, 96]. The preparation technique has a huge influence on the proximity effect, which is demonstrated well by the fact that magnetron sputtered Nb/Gd multilayers exhibit clear T_c oscillation with Gd thickness [61], while molecular beam epitaxy grown samples show step-like decrease in T_c [68].

Recently other REs, such as Ho and Er, have also been included superconducting devices exploiting their helimagnetic structure in the pursuit to generate long range triplet pairs [86, 122]. Most REs exhibit helimagnetism over some temperature range. By applying large enough external field, the magnetic spiral can be unwound irreversible in single crystal, while in polycrystalline material the transition is never fully completed [49]. The helimagnetic-ferromagnetic transition has been used to study the proximity effect in epitaxial Ho bilayers [48]. We conduct similar measurements on highly textured Nb/Ho_xDy_{1-x} bilayers, and their results are presented and discussed in the chapter.

7.1 Sample preparation

Highly-textured Nb(8 nm)/HoDy(40 nm)/Nb(20 nm) films are grown with DC magnetron sputtering on a-plane sapphire substrates as explained in Section 5.1. The intake in Fig 7.1a illustrates the structure. The purpose of the thin Nb capping layer layer on top is to protect the rare earth alloy from oxidation. It is too thin to superconduct therefore it acts as a normal metal layer and should have no significant influence on the proximity effect in the bottom Nb layer.

The rare earth alloy layers are deposited by simultaneously sputtering a Ho and a Dy target. The composition is controlled by adjusting the sputter rate via the sputtering powers on each target. This method is based on the assumption that the deposition rate of each element is proportional to the sputter power and it is the same when sputtered individually and simultaneously. To validate this assumption the total thickness of one sample in each deposition round is measured by wrapping a 1 mm-wide Ta strip around one of the substrates. After deposition, the strip is removed and the step height of the edge is measured using the

Dektak profilometer. The measured thicknesses show good agreement with the expected values suggesting the deposition rate do not influenced by whether one or two target is sputtered.

The composition is varied between 20 and 47 % Dy content. Depositing alloys with less than 20 % Dy either requires either the sputtering power on the Dy target to be too low to maintain a stable plasma or the Ho deposition rate to be high, which lowers the crystal quality. The composition of the rare earth layers is also checked using energy dispersive X-ray (EDX) spectroscopy. The composition values from the EDX measurements agree with the calculated values from the deposition rates within the margin of error, however the Ho and Dy emission lines are very close to each other and close to the noise level that the uncertainty from the fitting of the spectral scans is similar to the uncertainty in the deposition rates.

7.2 Characterisation

The sputtered films are examined by XRD to determine the orientation of the crystal lattice. An example scan for 43 % Dy is shown in Fig 7.1. The only peaks corresponding to the rare earth layer are the (002) and (004) peaks at 31.8 and 66.3°. The lack of other peaks confirms that the magnetic layer is oriented with its c-axis out-of-plane. The Nb (110) peak is near the Al_2O_3 peak where the background signal is high and samples containing only 28 nm of Nb in total show only a small bump next the substrate peak. The small peak around 29° is from the oxide layer. The FWHM of the HoDy (002) peaks vary between 0.8 and 1.5°, which higher than expected from the instrumental and thickness broadening (0.1°) as well as the values seen in previous work [95] suggesting that the films are highly textured but not epitaxial.

7.3 Magnetic measurements

The in-plane magnetic properties of each Ho_xDy_{1-x} composition are studied using a VSM at 10 K. The samples are cooled in zero field and the virgin curve was measured from 0 to 1.5 T followed by a full hysteresis loops between 1.5 and -1.5 T. To compare the magnetic properties of the different compositions, characteristic field and magnetisation values are compared including the saturation magnetisation (M_s) and remnant magnetisation (M_r), and the coercive field (H_c). The variation of these parameters with composition is plotted in Fig 7.2.

The saturation magnetisation for Ho and Dy and the slight increase of M_s is in agreement with the previously reported values [52, 55]. The remanent magnetisation shows a non-

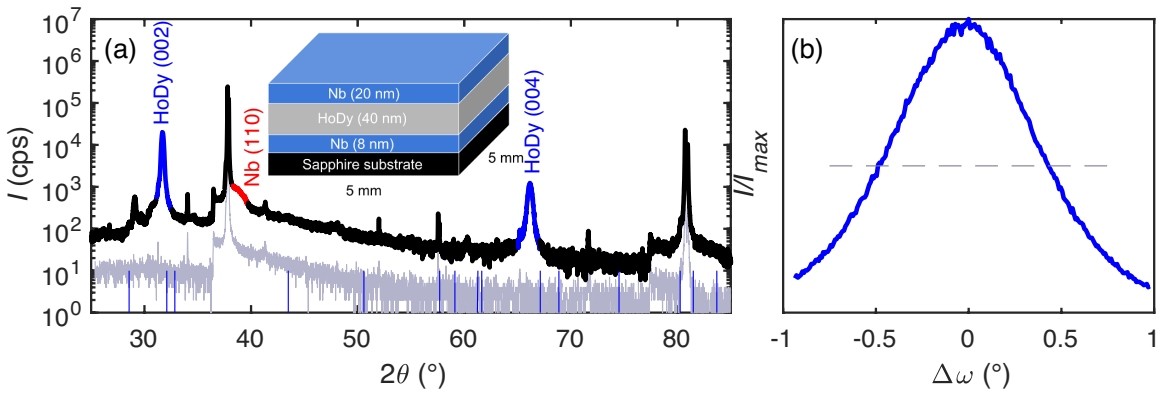

Fig. 7.1 Typical XRD scans for Nb/Ho_xDy_{1-x}/Nb. (a) $2\theta - \omega$ scan of a film containing 43 % Dy (black) with the scan of the bare substrate (grey) for comparison. The position of the XRD peaks from Ho powder are indicated with blue lines on the bottom for comparison. The intake shows the structure of the bilayer films (b) the rocking curve of the $Ho_{57}Dy_{43}$ (002) peak at 31.8° with FWHM of 0.912° indicated by the grey line.

monotonic behaviour with composition as M_r for the alloys is significantly lower than for either element. The lower remanent magnetisation can be an indication of the formation of magnetic domains in the alloys as magnetic domains broaden the magnetic reversal and lower M_r [38]. H_c monotonically increases between Ho and Dy, which is common for alloys with similar crystal structure.

The virgin curve exiting the hysteresis loop (demonstrated in Fig 7.3a) is an indication of a metastable helimagnetic state transitioning to a stable ferromagnetic state. The spiral state was observed in every alloy up to 43 % Dy content. The unwinding field (H_u), where the slope of the virgin curve is the highest, was defined to compare the magnetic spiral in different compositions. H_u was obtained by differentiating the virgin curve and finding the maximum of dM/dH. The FWHM of the peak in dM/dH is a good measure of how quickly the spiral unwinds. The definitions of these two parameters are illustrated with their values for Ho_xDy_{1-x} alloys in Fig 7.3.

Both H_u and the FWHM increases with the Dy content meaning that Dy broadens the helimagnetic-ferromagnetic transition and shifts it to higher fields. The higher FWHM in the alloys means that the transition starts at lower field than in Ho. Dy lowers the energy barrier between the helimagnetic and ferromagnetic state leading to the transition starting at lower field but also decreases the energy difference between the two states leading to a wider transition.

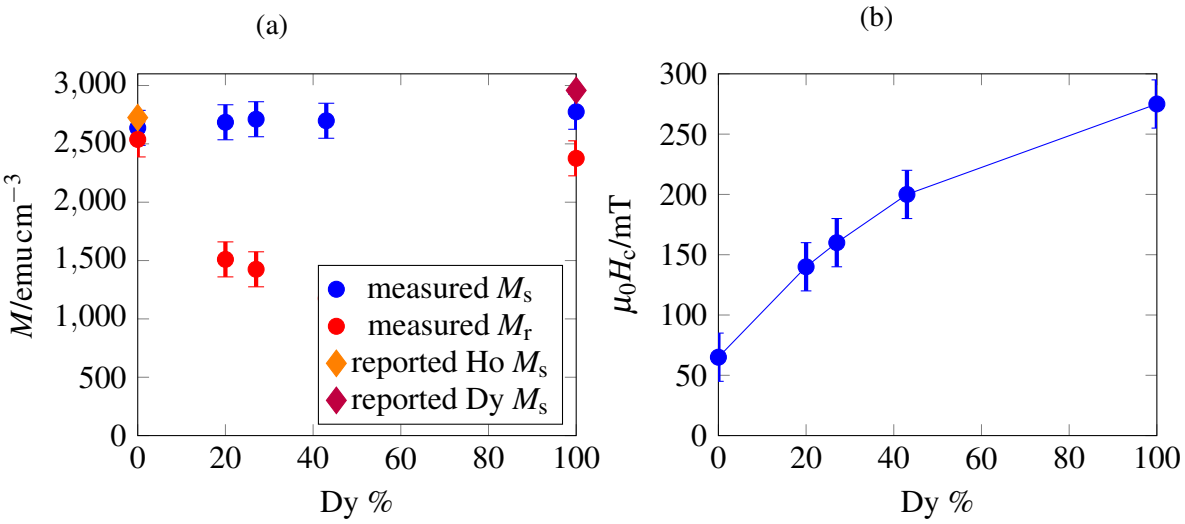

Fig. 7.2 Variation of the characteristic magnetisation values (a) and the coercive field (b) with composition. Previously reported values of saturation magnetisation for Ho and Dy are added for comparison [52, 55]. The error in the magnetisation is the combination of the uncertainty in the thickness and the noise from the VSM measurement while the error in H_c originates in the step size of the field sweep.

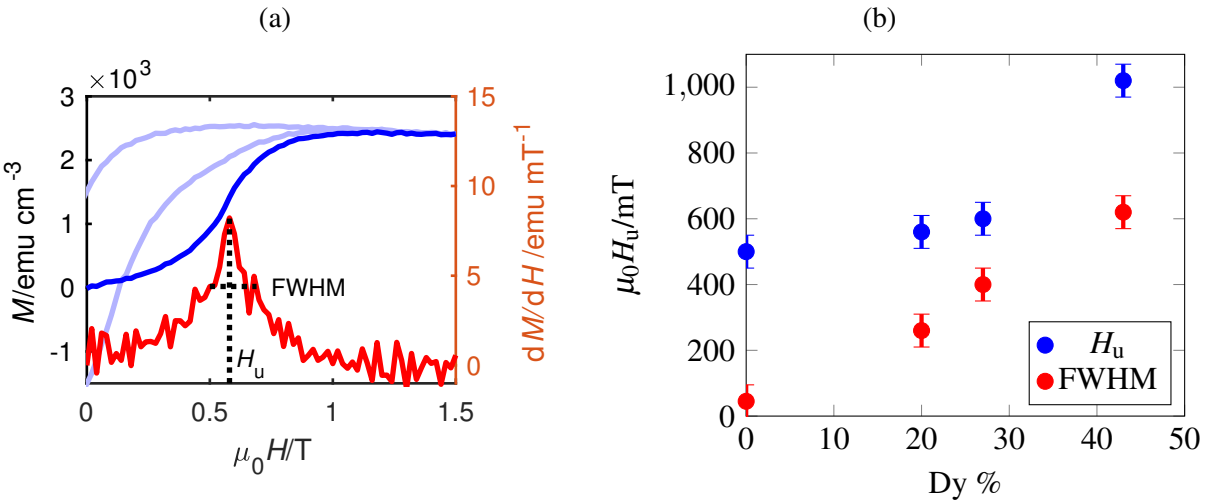

Fig. 7.3 Characterisation of the spiral state of the rare earth alloys. (a) The virgin curve (dark blue) exits the hysteresis loop (light blue) when the spiral state is present in the as-cooled bilayer. To find where the helimagnetic-ferromagnetic transition happens, M is differentiated with respect to H for the virgin curve (right axis). The position of the peak (H_u) and its full width at half maximum (FWHM) are illustrated. (b) The variation of H_u and FWHM with composition. The error bars are equal to the step size of the field sweep in the VSM measurement.

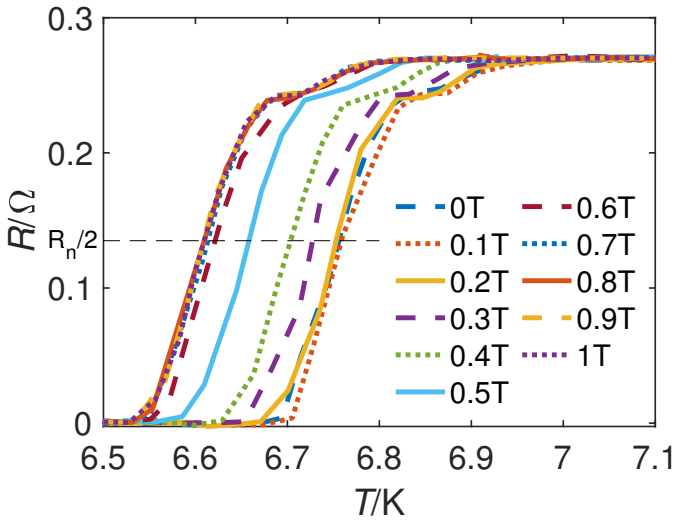

Fig. 7.4 Typical $R(T)$ curves measured in Nb/$Ho_{80}Dy_{20}$ bilayers after applying different set fields. $R(T)$ is measured in zero magnetic field after removing the given H_{set}. T_c is defined as $R(T_c) = R_n/2$. The curves start to shift when H_{set} reaches 0.3 T and finish the transition around 0.6 T.

7.4 Critical temperature measurements

The critical current measurements are carried out in a liquid helium fridge in a 4-point configuration as described in Section 6.3.1. The $R(T)$ curves are measured in zero field for a range of set magnetic fields (H_{set}). Each cycle starts at a temperature above the transition temperature of the sample and before each temperature cycle, the applied magnetic field is increased to H_{set} and is removed after 1 min. H_{set} is applied when Nb is in the normal state to avoid any screening from Meissner effect. Once the external field is removed, the temperature is gradually lowered below T_c then increased to the starting temperature while measuring R. This cycle is repeated for each H_{set} value. The temperature range for each sample is adjusted depending on their T_c. The $R(T)$ curves during warming are used in the analysis as they show higher temperature stability. A set of $R(T)$ curve is shown in Fig 7.4. The plateau just above the superconducting transition is a sign of the superconducting peak effect, which is typical for type-II superconductors like Nb. It is originates in the formation of vortices and appears as non-monotonic behaviour in the $R(T)$ and $I_c(T)$ curves or as a peak in the $I_c(H)$ curve near the superconducting transition [123, 124].

The $T_c(H_{set})$ curves for each composition are presented in Fig 7.6. The superconducting transition decreases when H_{set} is increased above a threshold. The set field values where T_c drops show a good agreement with H_u from the magnetic measurements confirming that the change in T_c is due to the helimagnetic-ferromagnetic transition. The exchange field in the

helimagnetic state averages to zero over the full period of the spiral (P_s). When $P_s \ll \xi_n$, the helimagnetic rare earth layer is equivalent to a non-magnetic layer and the superconductivity is more suppressed when the rare earth layer is in the ferromagnetic state than when in the helimagnetic state. This agrees with previous work done on Nb/Ho bilayers [48].

The zero field critical temperature T_{c0} and the difference in T_c between the spiral and ferromagnetic states (ΔT_c) are plotted as functions of the Dy content in Fig 7.6a. T_{c0} varies significantly between samples so the reproducibility of the measurements is needed to be tested so a $Nb/Ho_{80}Dy_{20}$ bilayer is remeasured multiple times. After the first set of measurements, the sample is heated to room temperature without breaking the vacuum of the cryogenic system, re-cooled then measured again. After the second measurement it is heated to 100 °C in air for 15 min and measured again. Finally, it is remeasured after keeping it at room temperature for 12 days. The resulting $T_c(H_{set})$ data is shown in Fig 7.6b. T_c shows no significant difference between the first two measurements. After keeping the sample at 100 °C for 15 min, T_c drops by 65 mK and it decreases by a further 25 mK after 12 days. The decrease of T_c with time suggest that the samples slowly oxidise, which suppresses the superconductivity. It is worth noting that the shapes of the $T_c(_{set})$ curves in Fig 7.6b are the same meaning that the effect of oxidation on H_u and ΔT_c is negligible. The change of the samples over time makes reproducibility more difficult especially in the absolute T_c values. Only one of the two samples measured are presented here for each set.

The variation in T_{c0} is greater than 1 K and cannot be explained solely with the effect of oxidation. The other causes are most likely to be originated in small variations on the preparation of the films, such as fluctuations in the thicknesses, electron mean-free-path and the quality of the interfaces that is affected by multiple factors such as the total deposition rate and the vacuum base pressure during deposition. These influences does seem to have no significant effect on ΔT_c, which decreases with Dy content.

The main effect of adding Dy to Ho is decreasing the electron-mean-free path and hence the coherence length $\xi_{RE} = \sqrt{\hbar v_F l / 6\pi k_B T}$ as the Dy atoms can act as impurities in the Ho matrix. This ultimately decreases the proximity effect as the Cooper pairs penetrate the RE layer less far and therefore changes in the RE layer affect the condensate less. If ξ_{RE} becomes very short, the magnetisation of the interface determines the proximity effect.

The increased Dy content can also affect the magnetic spiral. The period of the magnetic spiral in HoDy alloys has not been measured, though it would be expected to increase with Dy content as Dy is ferromagnetic at 10 K. If ξ becomes comparable to or smaller than the period of the spiral (P_s), the Cooper pairs experience a non-zero $\tilde{h}$ in the spiral state, which increases the suppression of T_c. For high Dy content, l can drop to the interatomic distances around ($l \sim 1$ nm) resulting in $\xi_n \approx 10$ nm (from (1.23) and using $v_F = 1 \times 10^6\,\mathrm{m\,s^{-1}}$ [125]).

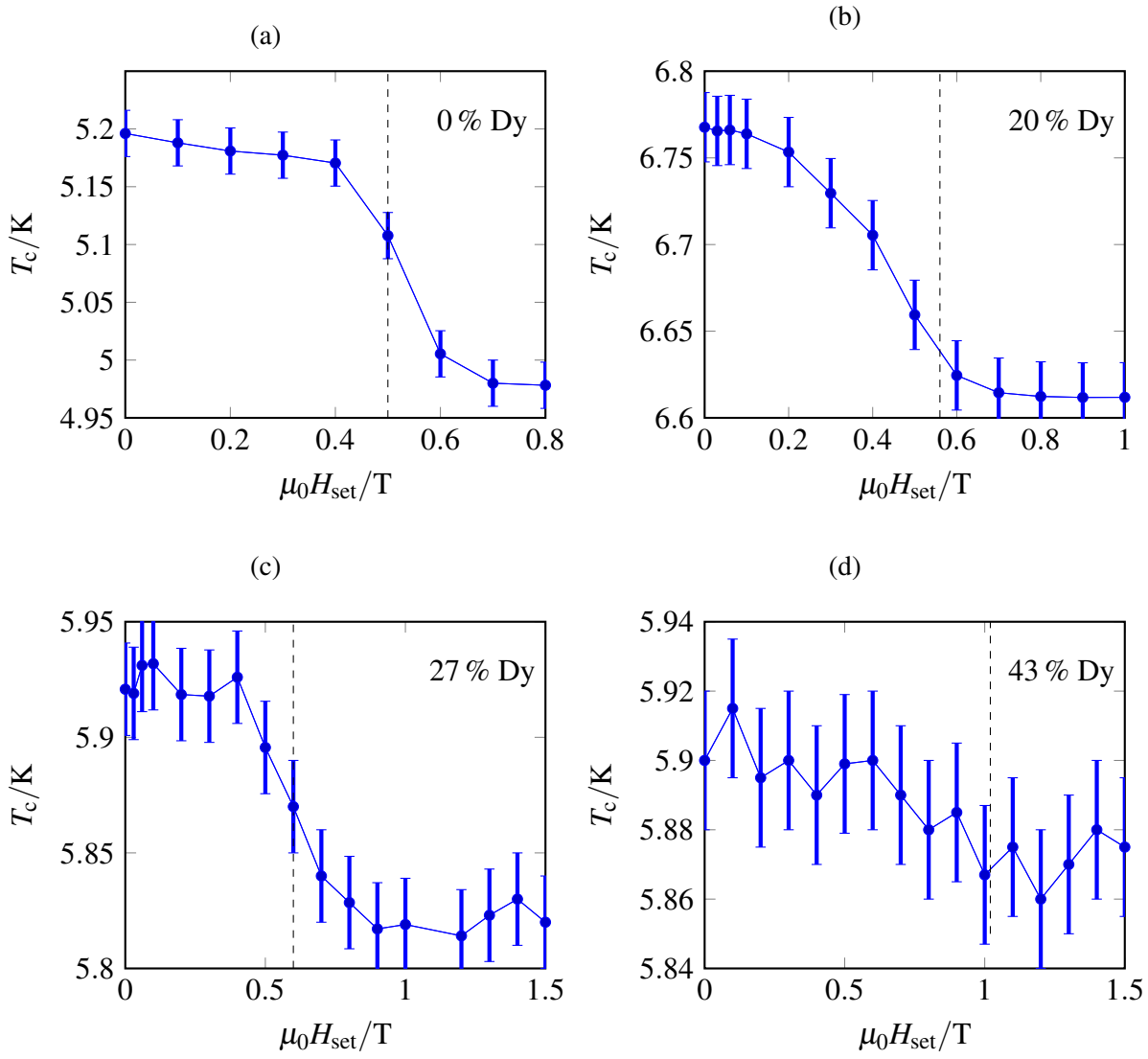

Fig. 7.5 $T_c(H_{set})$ curves for (a) 0 % (b) 20 % (c) 27 % (d) 43 % Dy content. The vertical dashed line indicates the H_u value for the given composition from Fig 7.3b. The error in each T_c measurement is estimated from the step size near the superconducting transition.

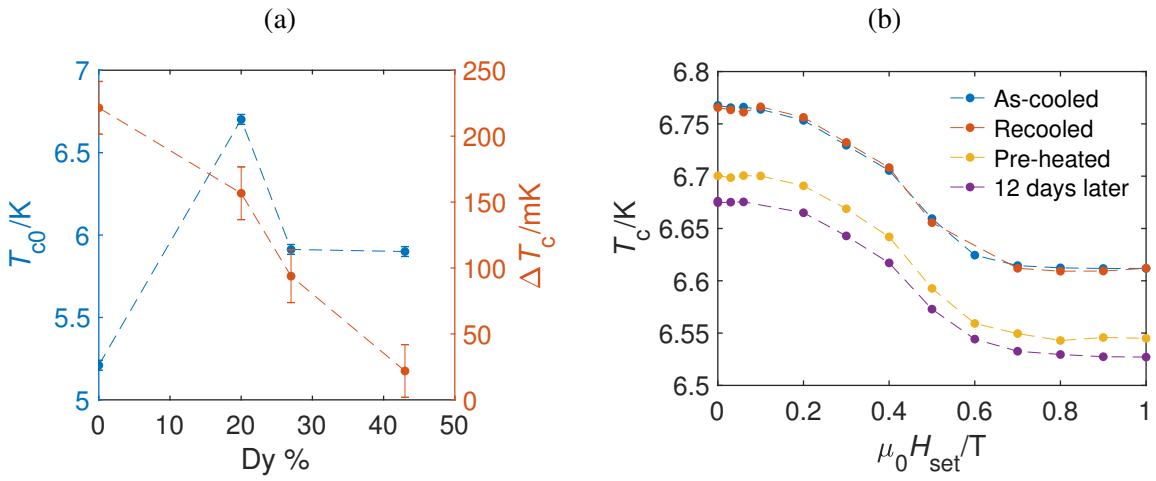

Fig. 7.6 (a) T_{c0} (left axis) and ΔT_c (right axis) as functions of composition. (b) Repeated $T_c(H_{set})$ curves for $Ho_{80}Dy_{20}$. The procedure is explained in the text.

This is about $2P_s$ in Ho therefore adding Dy can make P_s and ξ_n comparable leading to a non-zero $\tilde{h}$ and the suppression of T_c in the spiral state. This effect lowers T_{c0} as well as ΔT_c but unlikely to explain the variation seen in Fig 7.6a. Because of the many factors influencing T_{c0}, it is impossible to justify the above process from the results.

Dy can also affect T_c in the ferromagnetic state. The magnetic measurements show that M_r decreases with Dy content. If the magnetic domains are smaller than ξ_n, the smaller M_r means that the average exchange field is lower. If $\tilde{h}$ is lower, the proximity effect is also smaller resulting in higher T_c in the ferromagnetic state. Both effects are responsible of decrease of ΔT_c with Dy content.

7.5 Conclusions

In summary, the magnetic properties of highly textured Nb/Ho_xDy_{1-x} bilayers, including the unwinding of the magnetic spiral, is studied for up to 43 % Dy content. The saturation magnetisation is consistent with the previously reported values for Ho and Dy but the remanent magnetisation of the alloys is lower than the elements and decreases with Dy content in the measured samples. The magnetic spiral is observed up to 43 % Dy content. Dy broadens the helimagnetic-ferromagnetic transition and shifts it to higher field.

The transport properties of the bilayers are studied and a drop in T_c is found at increasing set field consistently with measurements on Nb/Ho bilayers. The field value where T_c drops correlates well with H_u indicating that the change in T_c is related to the rare earth layer transitioning from the helimagnetic state to the ferromagnetic state. The magnitude of the

T_c drop decreases with increasing Dy content and possible explanations are discussed. One is related to the Dy content decreasing the electron mean-free-path and time Cooper pairs spend in the RE layer, hence the effect of the change of magnetic state is smaller. The increased Dy content also decreases the remnant magnetision of the films so the zero-field average exchange field is lower in the alloys. The variation of the zero-field T_c cannot be fully explained by the composition and other potential factors such as oxidation are discussed.

Chapter 8

Highly textured Nb/Ho/Nb Josephson junctions

There has been significant developments over the past decade and half in the understanding of the interaction between superconductivity and ferromagnetism at superconductor/ferromagnet interfaces involving spin-singlet superconductors and transition metal ferromagnets (TMFs) [5, 126, 127]. In a TMF there is an exchange splitting in the density of states for the up- and down-spin electrons of the order 1 eV, which manifests as a spin-polarisation of the d-band electrons at the Fermi energy and a bulk magnetisation as explained in Section 3.2.2. The spin-polarisation suppresses the Andreev reflection increasing the interface resistance and the exchange field leads to a short-range oscillating decay of ψ into the TMF. This results in I_c decaying rapidly while oscillating between 0 and π states in Josephson junctions with TMF barriers. Typical decay length for these systems is on the order of 1 nm [75, 128–131].

The RKKY coupling leads to no spin-polarisation and results in weaker exchange field in rare earth ferromagnets (REF) compared to TMFs, which makes them desirable for spintronic applications. The spiral state of REFs, such as Ho and Er, can also provide the magnetic inhomogeneity for long-range triplet generation. Recent experimental works include the observation of large critical temperature shift in Ho/Nb/Ho superconducting pseudo-valves [95], study of the proximity effect in the helimagnetic and ferromagnetic states of Nb/Er and Nb/Ho bilayers [122, 48] and triplet Josephson junctions [132, 86].

Oscillations between 0 and π states can be controlled in Josephson junctions with multilayer F barriers - for example in SFNFS junctions. The exchange field in both F layers are additive meaning that the total exchange field is lower (higher) in the antiparallel (parallel) state, meaning that I_c can in principle be enhanced (suppressed). Misaligning the exchange

field between the two F layers can also lead to conversion of single to triplet pairs as recently demonstrated in [85, 86, 132–136].

0 to π transitions can in principle be manipulated in a Josephson junction with a single F layer via temperature if the exchange energy is of the order of the thermal energy [73]. Alternatively, 0-π transitions can be achieved with a single F barrier in which the magnetic state is magnetic-field-tuneable. Rare-earth elements, such as Ho or Er, are promising candidates since at low temperature they have a complex magnetic phase diagram [38].

In this chapter, experimental results are reported for textured Nb/Ho/Nb nanopillar Josephson junctions. The decay length of I_c is over 100 nm and the maximum critical current through the junctions is independent of the magnetic phase. We observe unusual features in the magnetic field dependence of critical current [$I_c(H)$] which relate to the unwinding of Ho. A theoretical model indicating that I_c is determined by magnetised and demagnetised regions in the junctions is presented in Chapter 9.

8.1 Fabrication and characterisation

Textured Nb(250 nm)/Ho(d)/Nb(250 nm) trilayers are deposited by DC magnetron sputtering onto 5 mm × 5 mm heated a-plane sapphire substrates in Ar plasma in a chamber with a base pressure better than 10^{-8} Pa as detailed in Section 5.1.1. The bottom Nb layer was grown at 900 °C to initiate epitaxial growth after which the temperature was decreased to 650 °C for the deposition of Ho and the top Nb layers. The Ho barrier thickness (d) is variable between 7 and 30 nm. High-angle X-ray diffraction (XRD) (Fig 8.1) confirms (110) and (001) orientations for Nb and Ho respectively. The FWHM of the ω-scan around the Ho (002) peak is around 1° and 0.6° for Nb (110) peak (inset of Fig 8.1).

The in-plane M(H) loops of a Nb/Ho/Nb trilayer at 10 K are shown in Fig 8.2a. The magnetic spiral in the as-cooled films is metastable so the magnetisation from the virgin state (dark blue curve) saturates in 0.8 T magnetic field, which is higher than the saturation field for the magnetised sample (0.6 T). Once fully saturated, the films remain ferromagnetic and display hysteresis in $M(H)$ (light blue curve). The saturation magnetisation is $M_s = 2660 \pm 150\,\mathrm{emu\,cm^{-3}}$, the remnant magnetisation is $M_r = 700 \pm 10\,\mathrm{emu\,cm^{-3}}$ and the magnetic susceptibility at 0 T is $\chi_{Ho} = 21.5 \pm 1.9$ which are consistent with previous measurements [48].

The films are patterned into a 4 µm-wide wire structure with optical lithography and Ar-ion etching (Section 5.2). Nanopillar junctions around 400 nm in dimension are fabricated using FIB according to Section 5.3 (Fig 8.2b). The beam shift from the substrate charging up causes low success rate of only about 1 in 7 junctions working. The faulty junctions

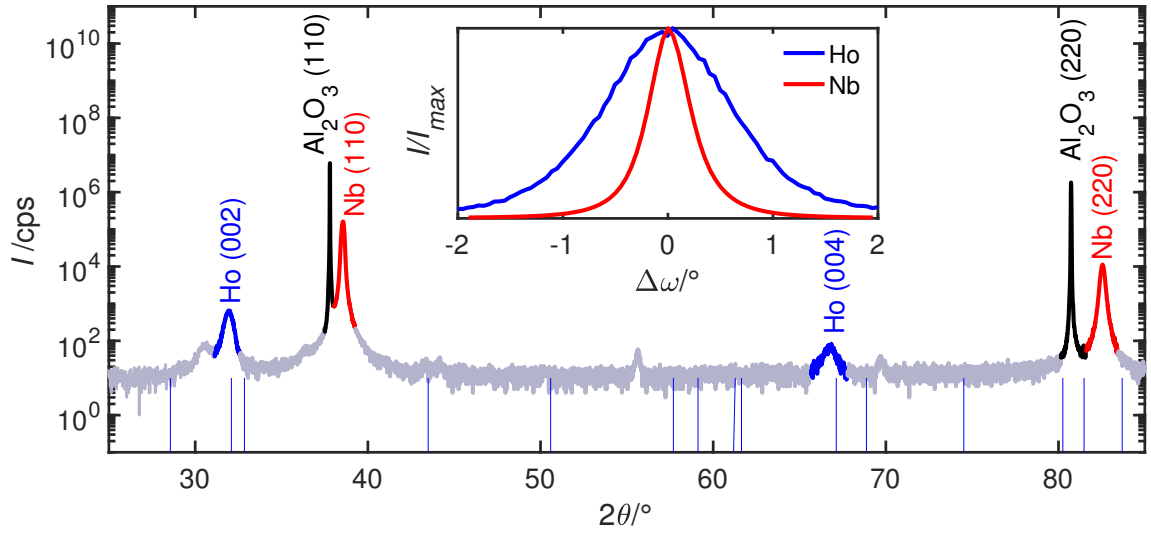

Fig. 8.1 A high angle X-ray diffraction trace of a Nb(250 nm)/Ho(30 nm)/Nb(250 nm) trilayer showing *c*-axis texture with well-defined Ho (002) and Nb (110) peaks. The inset shows rocking curves for Ho (002) (blue) and Nb (110) (red) with FWHM values of 1° and 0.5° respectively.

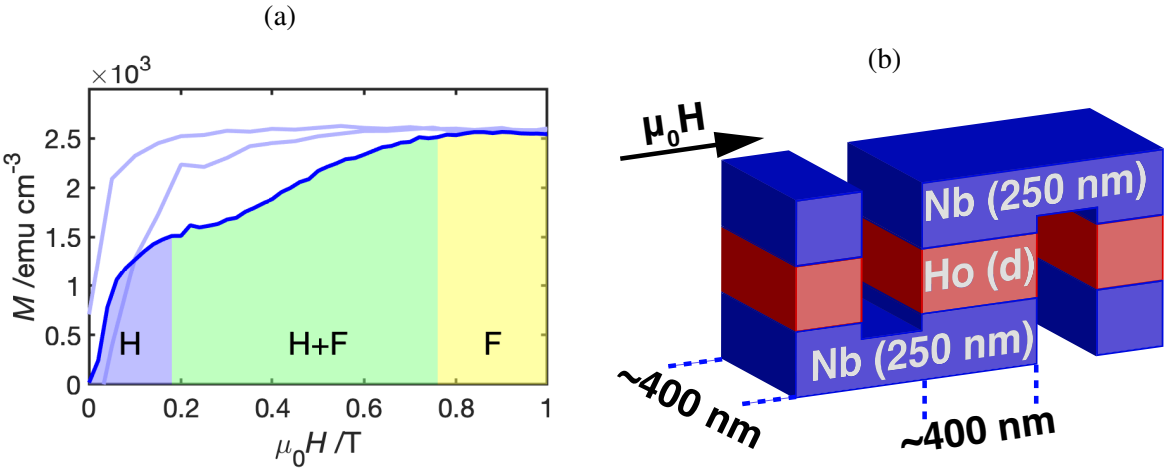

Fig. 8.2 (a) In-plane $M(H)$ curves for a 5 mm × 5 mm Nb(250 nm)/Ho(30 nm)/Nb(250 nm) trilayer at 10 K. The dark blue line shows the virgin curve following zero field cooling. The light blue curve shows part of the ferromagnetic loop following magnetic saturation. The coloured regions illustrate the magnetic phases of Ho and the possible magnetic structures in zero field: (blue) helimagnetic (H) region that is reversible with magnetic field, (green) above +0.15 T H and F regions coexist when the magnetisation is partially reversible, (yellow) beyond +0.75 T the Ho saturates to a ferromagnetic state (F) and the spiral cannot be recovered without heating above Néel temperature. The unwinding process of Ho is detailed in [49]. See also Fig 3.5 (b) Illustration of the structure of the junctions. The typical dimensions are labelled

either remain resistive at 4.2 K suggesting the superconducting bridge connecting the pillar to the superconducting leads is either too thin or completely cut through, or the $I_c(H)$ curve decreases monotonically away from zero implying the presence of a superconducting short and that the incisions creating the pillar are not deep enough.

8.2 Zero field measurements

Electrical properties of Josephson junctions are measured using an oscillating current in a liquid He dewar at 4.2 K using a four-point-measurement set-up. The current-voltage (IV) characteristics are well-described by the resistively shunted junction model (Section 2.3). We use this model to extract I_c and the normal state resistance (R_n). The variation of I_c and R_n with the Ho thickness is shown in Fig 8.3.

R_n is the sum of the contributions from the resistivity of Ho (ρ) and the interfacial resistance (R_{int}) from the two Nb/Ho interfaces, $R_n = \rho d/A + R_{int}/A$. Both contributions are inversely proportional to the area of the junction A, therefore the R_nA product (Fig 8.3a) depends on d. By fitting a line to R_nA *vs.* d, we estimate $\rho = 160 \pm 40\,\mathrm{n\Omega\,m}$ with $R_{int} = 20.6 \pm 1.6\,\mathrm{f\Omega^2\,m}$. ρ is lower than the values reported for equivalent junctions with polycrystalline Ho as the higher crystal quality decreases electron scattering [133, 137]. The large R_{int} relative to ρd indicates that the interfacial term dominates in R_n. A potential reason for the high R_{int} value is the mismatching band structure although that affects the polycrystalline samples as well. Another explanation is that the deposition was stopped for almost 1 h after the bottom Nb layer to lower the heater temperature. This time is significantly longer than the wait between depositions for polycrystalline samples and can induce higher concentration of impurities at the first Nb/Ho interface increasing R_{int}.

We estimate an electron mean-free-path in Ho of $l = v_F m e/\rho n e^2 = 11 \pm 3\,\mathrm{nm}$ and a diffusivity of $D = v_F l/3 = 5.9 \pm 1.5 \times 10^{-3}\,\mathrm{m\,s^{-1}}$, where $v_F = 1.6 \times 10^6\,\mathrm{m\,s^{-1}}$ is the Fermi velocity in Ho [125], m_e is the effective electron mass, n is the free electron density and e is the electric charge. The l value is in agreement with previous measurement in epitaxial Ho/Nb/Ho SSVs [95]. The coherence length in the clean limit would be $\xi_n = \hbar v_F/2\pi k_B T \approx 460\,\mathrm{nm}$, which is much larger than l implying that the junctions are in the dirty limit, for which the appropriate coherence length is $\xi_{Ho} = \sqrt{\hbar v_F l/6\pi k_B T} = 46\,\mathrm{nm}$.

In Fig 8.3b, we have plotted the characteristic voltage (I_cR_n) *vs.* d for our textured junctions and polycrystalline Josephson junctions from previous experiments [137]. The textured junctions show higher I_c values than polycrystalline junctions for equivalent values of d and I_c has a much longer decay length. Fitting an exponential function to the data an estimate of $250 \pm 100\,\mathrm{nm}$ for the coherence length is obtained, which is between the

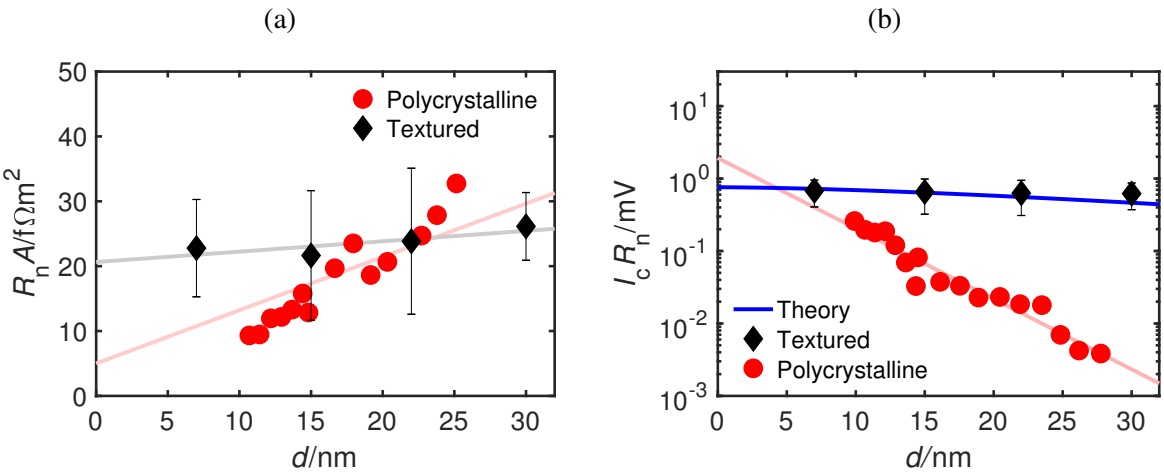

Fig. 8.3 (a) R_nA *vs.* d and (b) I_cR_n *vs.* d in zero magnetic field at 4.2 K for a series of Nb/Ho/Nb Josephson junctions. The black data points correspond to the textured junctions and the red data is from polycrystalline junctions [137]. For each thickness two junctions were measured and the average values plotted. The error bars are the combination of the uncertainty from fitting to the *IV* curves combined with the spread of the values measured at the same thickness.

theoretical values for the clean and the dirty limit suggesting that our junctions on the border between the two regimes. This is in contradiction with the electron mean-free-path implying that the junctions are well in the dirty limit indicating that an exponential decay model from (2.5) is too simplistic for our Josephson junctions.

To Usadel equation is more appropriate to model these junctions with. The corresponding boundary conditions give $F_s = \Delta/\sqrt{\omega^2+\Delta^2}$ at the boundary of the barrier [77]. With this anomalous Green's function the self-consistency equation (1.25) becomes

$$\Delta \ln\frac{T_c}{T} - 2\pi k_B T \sum_{\omega>0}\left(\frac{1}{\hbar\omega} - \frac{1}{\sqrt{\Delta^2+\hbar^2\omega^2}}\right). \tag{8.1}$$

Using $T_c = 9.2\,\mathrm{K}$ for the bulk Nb critical temperature and $T = 4.2\,\mathrm{K}$ the self-consistency equation gives $\Delta = 1.19\pi k_B T = 1.36\,\mathrm{meV}$. This is the theoretical band gap value at 4.2 K.

The characteristic voltage can be expressed from (2.8) in terms of $d_0 = d + R_{int}/\rho$, $k = \sqrt{2\omega/D}$ and $\Gamma = R_{int}\sqrt{\Delta^2+\hbar^2\omega^2}/\hbar\omega\rho$ as

$$eI_cR_n = \pi k_B T d_0 \sum_{\omega}\left(\frac{\Delta}{\hbar\omega}\right)^2 \frac{2k/\cosh(2kd)}{\tanh(2kd)(1+\Gamma^2k^2)+2k\Gamma}. \tag{8.2}$$

Fig 8.3b includes the curve from the Usadel equation for ρ. The curve from this equation by substituting the measured values of $\rho = 160\,\mathrm{n\Omega\,m}$, $R_{\mathrm{int}} = 20.6\,\mathrm{f\Omega^2\,m}$ and $\Delta = 1.36\,\mathrm{meV}$. The theoretical curve shows excellent agreement with the measured $I_{\mathrm{c}}R_{\mathrm{n}}$ values, which confirms that the Ho junctions can be considered non-magnetic when the Ho is in the spiral state. The close fit of the experimental data with the theoretical prediction also shows that Ho is a good candidate for testing models based on the Usadel equations.

Extrapolating to $d = 0$, the point of intersection is $I_{\mathrm{c}}R_{\mathrm{n}} = 0.758\,\mathrm{mV}$, which is a factor of 2 lower than the superconducting gap of Nb calculated above. This is a consequence of the low interface transparency ($t = 1/(1 + R_{\mathrm{int}}/\rho\xi_{\mathrm{Ho}}) \approx 0.25$). In the low transparency regime, many of the Cooper pairs and electrons are reflected from the interface suppressing the Andreev reflection and the supercurrent through the boundary. Our results show the important role interfaces play in superconducting devices.

8.3 Magnetic field dependence

We now discuss the $I_{\mathrm{c}}(H)$ behaviour in the reversible field regime. Up to 500 mT external field is applied in-plane to the junctions while continuously measuring the critical current obtaining the $I_{\mathrm{c}}(H)$ behaviour. For a rectangular Josephson junction, $I_{\mathrm{c}}(H)$ should follow a Fraunhofer-type behaviour according to (2.23). We observe three characteristic $I_{\mathrm{c}}(H)$ behaviours (Fig 8.4) which do not match standard Fraunhofer behaviour, including split peaks at $|H| > 0$ (Fig 8.4a), a concave central peak at H = 0 (Fig 8.4b) or a convex central peak at H = 0 with non-zero minima Fig 8.4c). The curves stay the same over time and when sweeping the magnetic field in either direction excluding the possibility of the unusual features originating from noise. None of these behaviours seem to be correlated to d. The deviation from the Fraunhofer-like $I_{\mathrm{c}}(H)$ curve indicates that the magnetisation and the critical current density are not uniform inside the barrier. Chapter 9 outlines a model that explain the $I_{\mathrm{c}}(H)$ behaviour of the junction. It assumes that the magnetisation increases faster near the edges of the nanopillar as the the Ho atoms have fewer nearest neighbours and the exchange field is weaker. The high magnetisation region propagates propagates towards the centre of the barrier as the external magnetic field increases. This creates a magnetic field dependent non-uniform magnetisation profile within the barrier that can reproduce the features observed in our junctions. The sharp central peak and the concave central peak shown in Fig 8.4 can only be reproduced by the model if the supercurrent flows in the opposite direction in the two regions meaning the junction is in a simultaneous 0 and π state.

To investigate the $I_{\mathrm{c}}(H)$ behaviour in the regime where the magnetic spiral is irreversibly unwound, junctions are measured in a liquid He fridge, where an external field up to 1 T

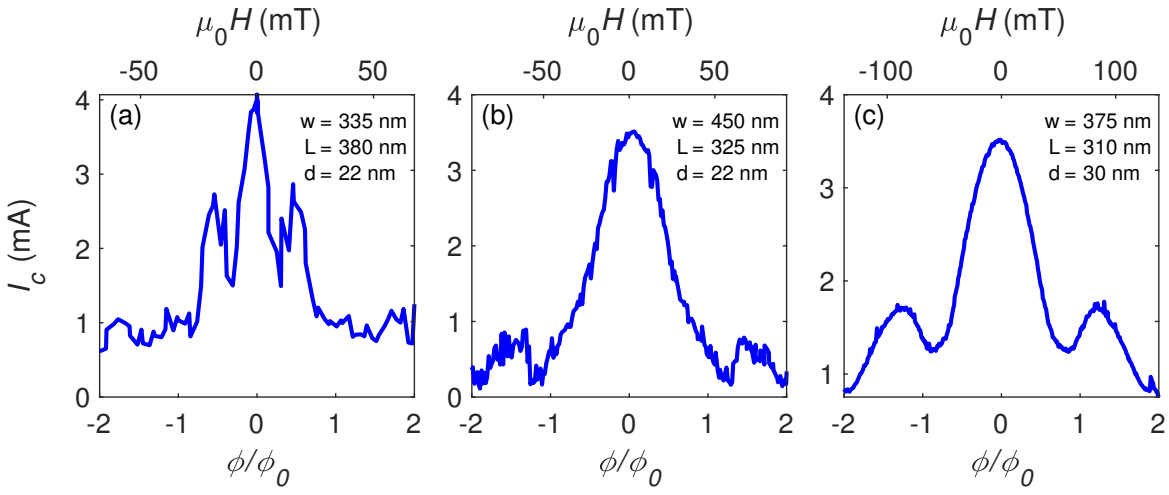

Fig. 8.4 Measured $I_c(H)$ behaviours in the reversible field regime normalised to $\phi_0 = 2.07 \times 10^{-15}$ Wb. The barrier thickness (d) and the width (w) and length (L) of the junction are labelled.

can be applied. Increasingly large set field is applied in-plane to the junction and $I_c(H)$ is measured in the -150 to 150 mT range. This protocol enables us to systematically investigate the form of Ic(H) across the magnetic phase diagram. Typical results are shown in Fig 8.5.

One key observation is that for larger H_{set} values the $I_c(H)$ curves become increasingly hysteretic with the central peak in I_c shifting from zero magnetic field. The shift of the central peak is proportional to H_{set} indicating that the unwinding of the Ho spiral is increasingly irreversible. The largest observed separation between the maxima in I_c (ΔH) is 55.7 mT, which close to the coercive field of Ho of about 65 mT in an unpatterned film. A second key finding is that the maximum value of I_c ($I_{c,max}$) is found to be independent of the magnetic phase diagram implying that the coherence length is longer than the domain size when the magnetisation direction switches. The is also a consequence of the low interface transparency. As the transport properties are dominated by the interface, the change in the magnetic phase of the Ho has negligible effect. The exchange field in Ho is estimated to be 1 meV in epitaxial SSVs [95]. Substituting this value into (4.5), the ferromagnetic coherence length of Ho can be estimated as $\xi_{Ho,f} = \sqrt{\hbar D/h} = 30$ nm, which is comparable to the barrier thickness. $I_{c,max}$ remaining the same indicates that the magnetisation fluctuate over a length scale shorter than $\xi_{Ho,f}$ at H_c therefore $\tilde{h}$ is zero and $I_{c,max}$ is independent of the magnetic history of the junction.

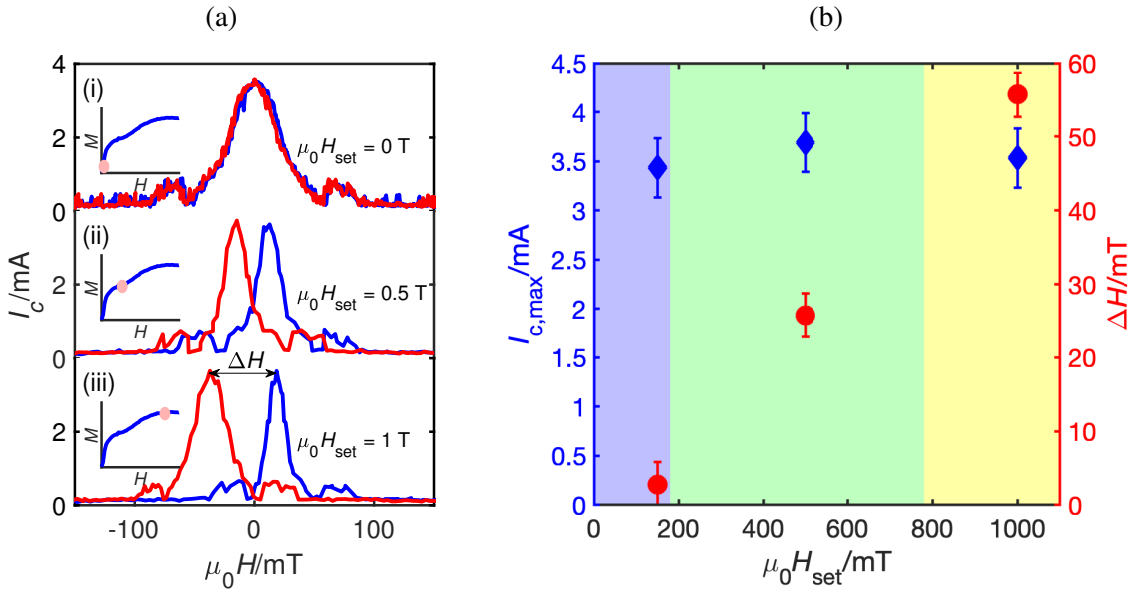

Fig. 8.5 $I_c(H)$ curves across the magnetic phase diagram. (a) $I_c(H)$ curves for set fields of 0 mT (i), 500 mT (ii) and 1000 mT (iii). Red (blue) curves show I_c in increasing (decreasing) field. The insets show H_{set} on the Ho $M(H)$ curve. The definition of ΔH is illustrated in (iii). (b) $I_{c,max}$ (blue) and ΔH (red) *vs.* $\mu_0 H_{set}$. The error in Ic,max is estimated from the signal fluctuation and the error in ΔH originates from the step size of the measurement.

8.4 Conclusions

In summary, we observe transport properties of highly textured Ho Josephson junctions with barrier thicknesses in the range of 7 to 30 nm. The electron mean-free-path is more than an order of magnitude longer in highly textured Josephson junctions than in polycrystalline junctions due to the high crystal quality, although the interface resistance is also increased due to the longer wait time between depositions of layers.

Even this increased l is much less than the thermal coherence length implying the transport processes are diffusive. The measured characteristic voltage values are in good agreement with the theoretical values from the Usadel equation. The coherence length is 46 nm, which is an order of magnitude higher than the coherence length in polycrystalline Ho [137]. The extrapolated characteristic voltage at $d = 0$ is half of the band gap energy of Nb indicating the significant influence of the interfaces on the Josephson effect.

Applying H_{set} up to 1 T, the $I_c(H)$ curves show hysteretic behaviour indicating that parts of the magnetic spiral are irreversibly unwound. The separation of the I_c peaks increases with H_{set} although the maximum value of I_c remains unchanged meaning the magnetisation of the barrier is not fully saturated. The shape of the $I_c(H)$ curves is unusual which implies that the magnetisation is non-uniform inside the barrier and discussed further in the next chapter.

Chapter 9

Theoretical model for Josephson junctions with non-uniform barrier magnetisation

S-wave singlet superconductivity and ferromagnetism are competing phases. Over the past half century considerable research has been undertaken in order to understand the interaction between these phenomena at superconductor/ferromagnet (S/F) interfaces [5, 138, 81, 126, 127, 58, 139]. A key experimental development was the demonstration of F-thickness-dependent oscillations in the Josephson critical current I_c in S/F/S junctions, first using weak ferromagnets (CuNi and PdNi [75, 129, 140–142]) and then strong ferromagnets (Fe, Co, Ni and NiFe [130, 131, 143–146]). This behaviour is a manifestation of the magnetic exchange field acting differentially on the spins of the singlet pairs, which induces oscillations in the superconducting order parameter in F superimposed on a rapid decay with a singlet coherence length of $\xi_f < 3\,\mathrm{nm}$ [130, 143, 145, 147]. The superconductivity in F can also be detected via tunnelling density of states (DoS) measurements [115, 116] and point contract Andreev spectroscopy [148, 149]. Furthermore, the magnetic exchange fields from F induces a Zeeman-like splitting of the DoS in S close to the S/F interface [5, 117, 150].

Recently there is a focus on Josephson junctions with inhomogeneous barrier magnetism, involving misaligned F layers [85, 151, 152] and/or rare earth magnets such as Ho or Gd [133, 153], in order to transform singlet pairs into spin-aligned triplet pairs [126, 154, 138]. Triplet pairs are spin-polarised and stable in a magnetic exchange field and decay in Fs over length scales exceeding ξ_f [139, 138]. However, the relatively large (total) magnetic barrier thickness in triplet junctions introduces significant flux which, in combination with magnetic inhomogeneity, creates a complex dependence of I_c on external magnetic field [155, 135].

A complication for junctions with magnetically inhomogeneous rare earths such as Ho (or Er) relates to the fact that the magnetic ordering and local magnetic susceptibility (χ) depends on a competition between Ruderman-Kittel-Kasuya-Yosida (RKKY) coupling between localised moments and shape anisotropy. This competition leads to the formation of the helimagnetic spiral as discussed in Chapter 3. At the edges of Ho, however, RKKY coupling is reduced which, in combination with shape anisotropy, may favour easy magnetisation alignment along edge regions. This translates to localised enhancements in χ at edges and thus an inhomogeneous magnetic induction in the junction.

In this chapter we calculate the magnetic-field-dependence of the Josephson critical current (i.e. Fraunhofer patterns) in S/F/S junctions with a position- and magnetic-field-dependent-χ (Fig 9.1). The model predicts anomalous Fraunhofer patterns due to spatial variations in χ and magnetic induction in which local minima in $I_c(H)$ can be nonzero and non-periodic due to interference between highly magnetised and demagnetised regions.

9.1 Magnetisation process

The S/F/S junction geometry under consideration is sketched in Fig 9.1 which summarises the magnetisation process (Fig 9.1a-d). We consider the case of a Josephson junction with a width L that is smaller than the Josephson penetration depth (which is usually the case for experiments [35]), so the applied magnetic field (H) fully penetrates the barrier. Following standard procedures outlined in Chapter 2, we calculate the phase variation across the S/F/S barrier taking into account the contribution from the magnetic moment to the total flux through the junction during the magnetisation process as summarised in Fig 9.1e. Applying H parallel to y causes the magnetisation M along junction edges parallel to y to propagate inwards towards the junction centre until magnetic saturation $H = H_s$. The expansion of the magnetised region is assumed to be reversible with a width that depends on H and not the magnetic field history. The propagation rate of the magnetised region is linear with H in our model and the position of the boundary between magnetised and demagnetised regions is $a = L/2 - PH$ (where P is the propagation parameter). The magnetisation is uniform in the y direction and position-dependent in the x direction with $M(x) = \chi(x)H$. We note that for certain materials the propagation rate of the magnetised region with H may not be linear, but as a first approximation we choose a linear form here which is likely to apply more broadly to magnetic materials in nanopillar Josephson junctions.

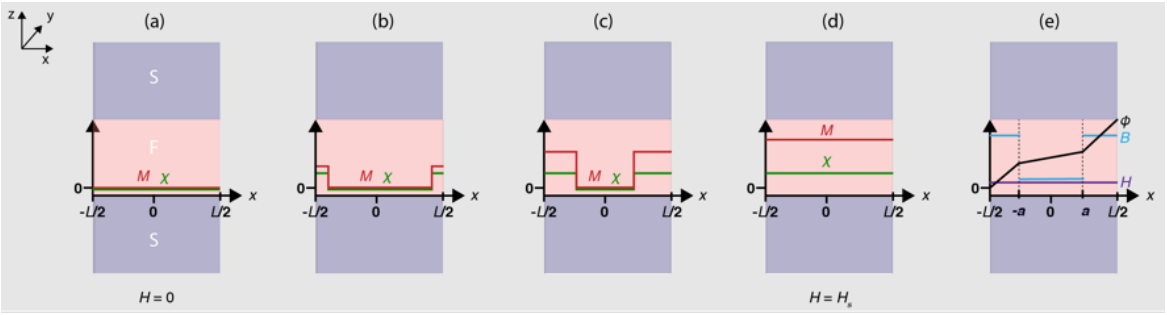

Fig. 9.1 Magnetisation process for an S/F/S Josephson junction with a position (x) and magnetic field (H) dependent magnetic susceptibility $\chi(x,H)$ and magnetisation $M(x,H)$. (a) For $H=0$ the net barrier moment is zero everywhere but on increasing H (b-d), M increases faster at the junction edges and propagates inwards until the magnetic barrier saturates ($H=H_s$) (d). (e) Spatial variation of magnetic induction B and superconducting phase difference Θ for $0<H<H_s$. The external field H is always applied in the y direction. The variables (M, Θ, H, B) plotted on the z-axis are labelled.

9.2 Critical current calculation

The spatial variation $M(x)$ means that the magnetic induction $B(x)$ is non-uniform. The line integral of B(x) across the junction gives the spatial gradient of the superconducting phase according to (2.16)

$$\frac{\partial\Theta}{\partial x}=2\pi\frac{\int B_\perp \mathrm{d}l}{\phi_0}=2\pi\mu_0\frac{\bar{d}H+\chi_\mathrm{m}dH}{\phi_0}, \tag{9.1}$$

where χ_m is the magnetic susceptibility in the magnetised region.The first term in (9.1) is from the external field penetrating both the barrier and the superconductor over the London penetration depth therefore $\bar{d}=d+2\lambda$. The second term rises from the magnetisation of the material. Hence, $\Theta(x)$ in the magnetised ($a<x<L/2$) and demagnetised ($|x|<a$) regions is given by

$$\Theta(x)=\begin{cases}2\pi\dfrac{\phi}{\phi_0}\dfrac{x}{L}+\Theta_0 & |x|<a\\[2ex] 2\pi\dfrac{\phi}{\phi_0}\dfrac{x-a}{L}\left(1+\chi_\mathrm{m}\dfrac{d}{\bar{d}}\right)+2\pi\dfrac{\phi}{\phi_0}\dfrac{a}{L}+\Theta_0 & a<x<L/2,\end{cases} \tag{9.2}$$

where $\phi=\mu_0 HLd$ is the magnetic flux through the junction and Θ_0 is set to minimise the free energy and maximise I_c. The second term in (9.3) ensures $\Theta(x)$ is continuous. The spatial variation of the magnetic parameters and the superconducting phase difference are sketched in Fig 9.1e.

From (9.3), the position-dependent current density is

$$j(x) = \begin{cases} j_c \sin\left[2\pi\dfrac{\phi}{\phi_0}\dfrac{x}{L} + \Theta_0\right] & |x| < a \\ j_c Q \sin\left[2\pi\dfrac{\phi}{\phi_0}\dfrac{x-a}{L}\left(1+\chi_m\dfrac{d}{\bar{d}}\right) + 2\pi\dfrac{\phi}{\phi_0}\dfrac{a}{L} + \Theta_0\right] & a < x < L/2, \end{cases} \tag{9.3}$$

where j_c is the maximum critical current density in the demagnetised region and Q is the ratio of the critical current densities in the magnetised and demagnetised regions - i.e. $Q = j_{c,m}/j_c$. The net exchange field in the magnetised regions can favour a transition to a π-state [69, 73] and hence the directions of j_c and $j_{c,m}$ can be opposite to each other meaning Q can be negative.

The total critical current through the junction is the integral of $j(x)$ across the junction. As $j(x)$ is unifrom in the y direction, the integration over y gives a factor of w, the junction width in the y direction

$$I_c = \int_{-w/2}^{w/2}\int_{L/2}^{L/2} j(x)\mathrm{d}x\mathrm{d}y = w\int_{L/2}^{L/2} j(x)\mathrm{d}x. \tag{9.4}$$

As the model is symmetric in the x direction, it is easy to see that $\Theta_0 = \pi/2$ maximises I_c. Using the symmetry, it is enough to evaluate the integral from 0 to $L/2$

$$\begin{aligned} I_c = 2w\int_0^{L/2} j(x)\mathrm{d}x = 2wj_c\int_0^{a}\sin\left[2\pi\frac{\phi}{\phi_0}\frac{x}{L}+\frac{\pi}{2}\right]\mathrm{d}x + \\ +2wj_cQ\int_a^{L/2}\sin\left[2\pi\frac{\phi}{\phi_0}\frac{x-a}{L}\left(1+\chi_m\frac{d}{\bar{d}}\right)+2\pi\frac{\phi}{\phi_0}\frac{a}{L}+\frac{\pi}{2}\right]\mathrm{d}x. \end{aligned} \tag{9.5}$$

To illustrate the general features of our model, we introduce the following dimensionless parameters: the relative position of the boundary between the magnetised and demagnetised regions $l = a/L$, the effective permeability $q = \chi_m d/\bar{d} + 1$, and the normalised flux $f = \phi/\phi_0$. Substituting these parameters into equation (9.5) and using $\sin(x+\pi/2) = \cos(x)$ gives the following expression for I_c

$$I_c = 2I_{c0}\int_0^{l}\cos\left[2\pi f\tilde{x}\right]\mathrm{d}\tilde{x} + 2I_{c0}Q\int_l^{\frac{1}{2}}\cos\left[2\pi f(\tilde{x}-l)q + 2\pi f l\right]\mathrm{d}\tilde{x}, \tag{9.6}$$

where I_{c0} is the total critical current in zero field. The relation between a and H transforms into $l = \frac{1}{2} - pf$ in the normalised units, where $p = \frac{\phi_0}{\bar{d}L^2}P$. With these parameters, the above

integral can be evaluated to

$$I_c = \frac{I_{c0}}{\pi f}\left\{\sin\left[2\pi f\left(1/2-pf\right)\right]+\frac{Q}{q}\sin\left[2\pi f\left(1/2+pf(q-1)\right)\right]-\frac{Q}{q}\sin\left[2\pi f\left(1/2-pf\right)\right]\right\}$$
$$= \frac{I_{c0}}{\pi f}\left\{\sin\left[\pi f\left(1-2pf\right)\right]+2\frac{Q}{q}\sin\left(\pi f^2 pq\right)\cos\left[\left(\pi f 1+pf(q-2)\right)\right]\right\}. \tag{9.7}$$

At the magnetic saturation, f is $p/2$ meaning (9.7) is only valid for $|f| < p/2$. For $|f| \geq p/2$, the barrier is magnetised with a high effective permeability q so $I_c(f) = I_{c,m}\frac{\sin(\pi fq)}{\pi fq}$, where $I_{c,m}$ is the total critical current in the magnetised state and $I_{c,m} = Lwj_{c,m} = LwQj_c$.

As a sanity check, let us consider (9.7) for a few trivial case. For $p = 0$, meaning the junction is demagnetised for all values of H, we recover the standard Fraunhofer relation of (2.23). The solution takes the same form when the magnetised and the demagnetised regions are equivalent — i.e. $Q = 1$ and $q = 1$ for all values of p. Both of these agree with the expectations.

9.3 Discussion of the result

The shape of $I_c(f)$ is determined by Q, p and q and its magnitude by j_c and the junction area. The junction area depends on the fabrication and j_c mainly depends on the material therefore we focus on the general shapes of $I_c(f)$ curves different parameter sets can produce. Fig 9.2 shows a few examples for $I_c(f)$ patterns.

When the susceptibilities in the magnetised and demagnetised regions are different, we observe an interference in the critical current. However, due to the movement of the boundary between the magnetised and demagnetised regions with field, $I_c(f)$ is more complicated than simply the superposition of two $\mathrm{sinc}(f)$ functions. Due to phase oscillations in the magnetised regions, the field position and number of local minima and maxima that appear in $I_c(f)$ deviate from a non-magnetic junction with non-periodic behaviour. Furthermore, the magnitudes of I_c at local minima are not always 0 and I_c at local maxima do not decrease inversely with f as in (2.23) but can even increase. Once the barrier is fully magnetised ($f > p/2$), we recover standard $I_c(f)$ behaviour with periodic minima and peaks in $I_c(f)$ with peak heights decreasing inversely with f.

The parameters q, p and Q, influence $I_c(f)$ in different ways. For Q close to 1, j_c in the magnetised and demagnetised regions closely match, but in the magnetised regions the superconducting phase oscillates faster resulting in small waves on the side of the central peak. In the magnetised regions I_c quadratically decreases with f for small H ($f \ll 1$) and the central peak is rounded, resembling a sinc-type function (Fig 9.2b). For Q far

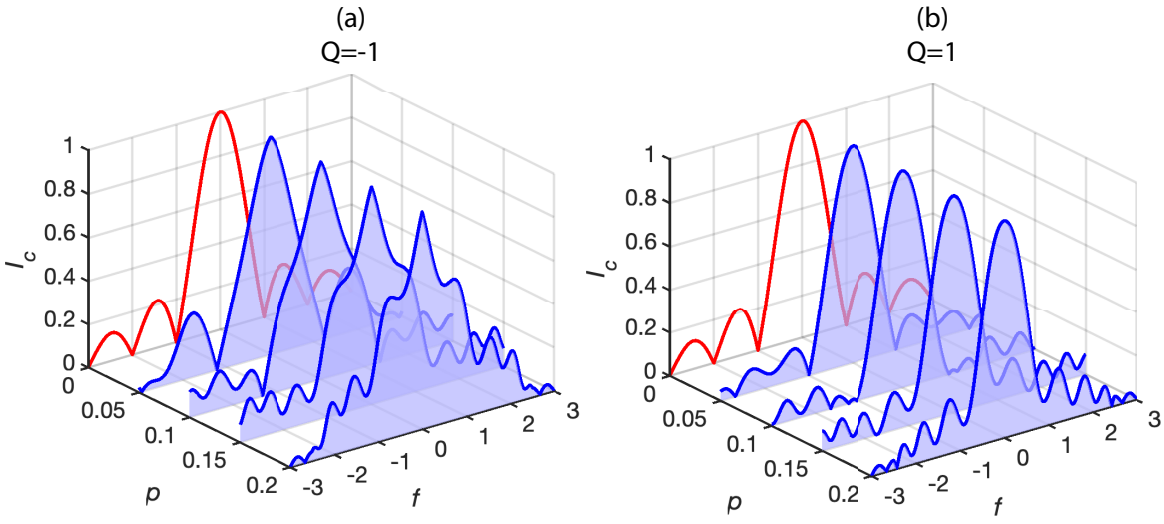

Fig. 9.2 $I_c(f)$ *vs.* p and f for positive and negative values of Q. The blue curves show $I_c(f)$ for $q = 3$, $Q = -1$ (a) and $Q = 1$ (b). The red curves show standard Fraunhofer patterns for a demagnetised junction ($p = 0$).

from 1 or negative, j_c differs in the magnetised and demagnetised regions. For small H ($f \ll 1$), I_c is mainly determined by the propagation of the magnetised region and, because the demagnetised region shrinks linearly, I_c decreases linearly and the central peak is sharp and concave. The difference in the shape of the central peak for $Q = 1$ and $Q = -1$ is demonstrated on Fig 9.2.

The other two parameters p and q affect the position of the minima and maxima as illustrated in Fig 9.3 which shows the position of the local minima and maxima of $I_c(f)$ for multiple sets of parameters. The plots are obtained by calculating $I_c(f)$ numerically for a set of parameters and finding the extrema of the curve. For each plot one of the parameters is treated as a free parameter and varied slowly. If two peaks are very close to each other or if their position changes rapidly with the free parameter, arithmetic limitations can lead to the breaking of lines even for high sampling frequency as can be seen on Fig 9.3d near $f = 2.5$ and $q = 0.03$.

The value of q determines how fast the phase oscillates with f in the magnetised region which influences the spacings between peaks. In general, higher values of q bring minima and maxima closer to the origin ($f = 0$) since the higher permeability in the junction causes the superconducting phase to oscillate faster with f in the magnetised regions. This is illustrated on Fig 9.3a-b. For positive Q, the curves at $q \sim 1$ resemble to Fraunhofer patterns but as q increases, neighbouring minima converge and they merge together making the maximum between them disappear. For negative Q, the peaks are shifted towards the origin and merging of minima is not observed.

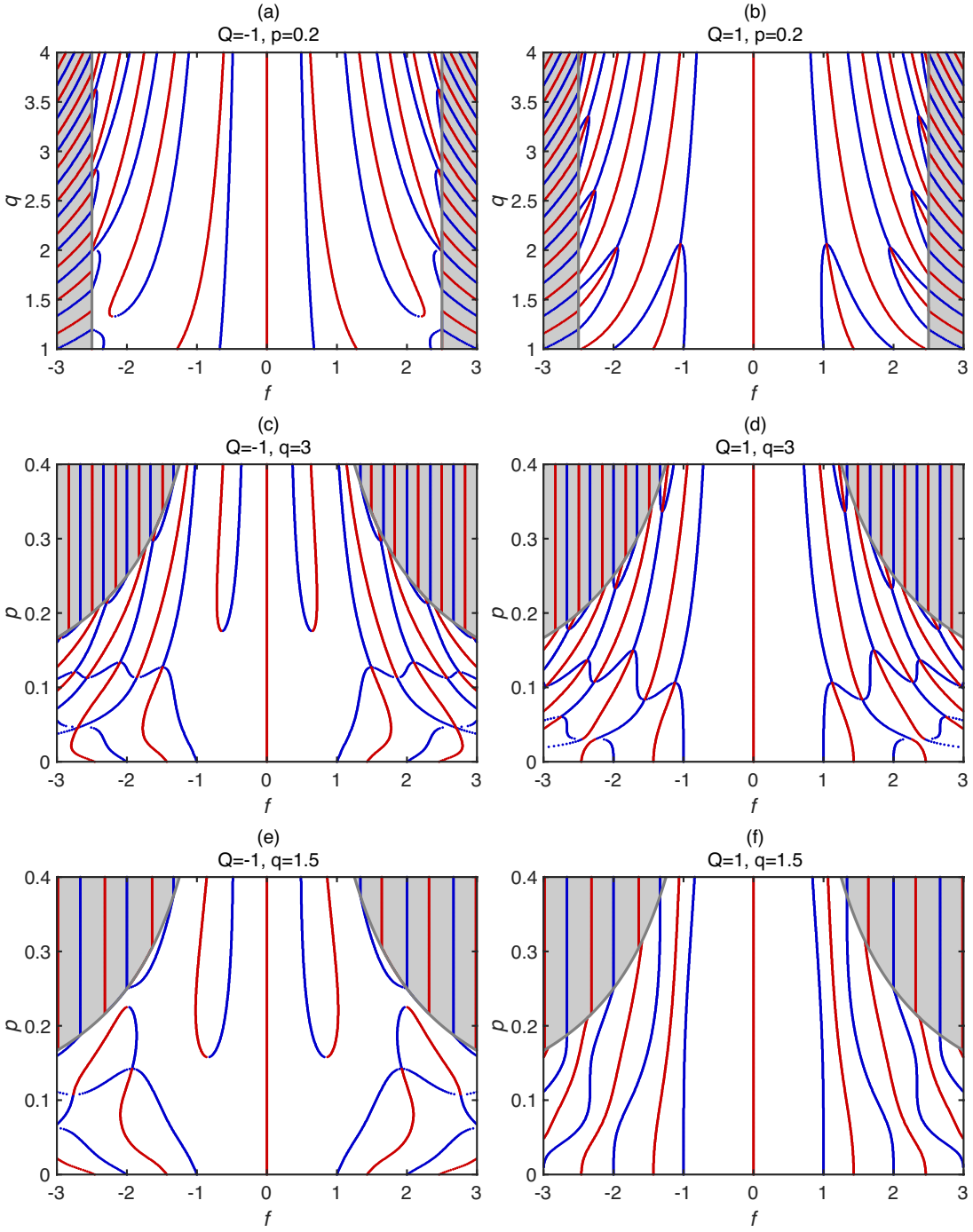

Fig. 9.3 The positions of local maxima and minima in $I_c(f)$. (a) and (b) show the positions of the minima (blue) and the maxima (red) of $I_c(f)$ with increasing q. (c-f) illustrate the movement of the minima and the maxima as p changes for $q = 3$ (c-d), and $q = 1.5$ (e-f). The grey lines indicate the field values where the barrier is magnetised fully. In the fully magnetised regions (shaded grey), a standard $I_c(f)$ Fraunhofer behaviour is recovered.

The effect of p on the shape of $I_c(f)$ is more complex as it affects the speed of the magnetisation process and hance at what field the magnetised region becomes significant. If $p \sim 0$, the propagation of the magnetised region is very slow and its contribution only because important in high fields, where I_c is suppressed. This is the non-magnetic junction limit. If p is large ($p > 1/2$), the barrier saturates for less than one flux quantum and $I_c(f)$ is dominated by the saturated behaviour. This is the case for most ferromagnetic Josephson junctions. The most unusual patterns, such as non-zero minima and concave peaks, emerge in the middle region ($0.05 < p < 0.2$).

Fig 9.3c-f illustrates the effect of p for four sets of values of q and Q. Multiple minima in $I_c(f)$ combine and some minima split into two minima forming a maximum. For $Q < 0$, there is a minimum-maximum pair forming just below $p = 0.2$ (exact value depends on q and Q). This new peak is below 1 and has no equivalent in a Fraunhofer pattern. For the higher value of q, a series of peaks split and combine at low p values. However when $p > 0.2$, the shape of $I_c(f)$ only weakly depends on p since the magnetised regions propagate rapidly with H and the magnetised regions dominate $I_c(f)$.

This model can produce $I_c(f)$ curves with a variety of features including split peaks, concave central peak and non-zero minima. It is most relevant for systems with relatively slow magnetisation process and stable non-magnetic state such that p is below 0.2. The observation of similar pattern is most likely in metals with high susceptibility, especially for positive values of Q.

9.4 Fitting to experimental data

The helimagnetic state of Ho is metastable, which can lead to a slow magnetisation process with low p value. The Josephson penetration depth for the junctions in Chapter 8 is $\Lambda_J \approx 1\,\mu m$, which is over the dimensions of the nanopillars meaning that the screening effects are negligible in the barrier. The sub-micron size of the junctions also enhances the influence of the surface and makes the magnetisation process plausible. Therefore, the junctions in Chapter 8 meet the conditions for our model.

The model is fitted to the measured $I_c(H)$ curves by manually adjusting the parameters as the high noise level of the measurements makes the automated fitting difficult. The main examples are presented in Fig 9.4. The fitted curves match the dominant features of the experimental curves such as the sharp central peak and shoulder peaks (Fig 9.4a), the concave central peak (Fig 9.4b) and the non-zero minima (Fig 9.4c). The fitted values for q are in good agreement with the estimate from the slope of the $M(H)$ curve near the origin in Fig 8.2a, which gives $q \approx 3$ for $\lambda \approx 45\,nm$ in Nb [156, 157].

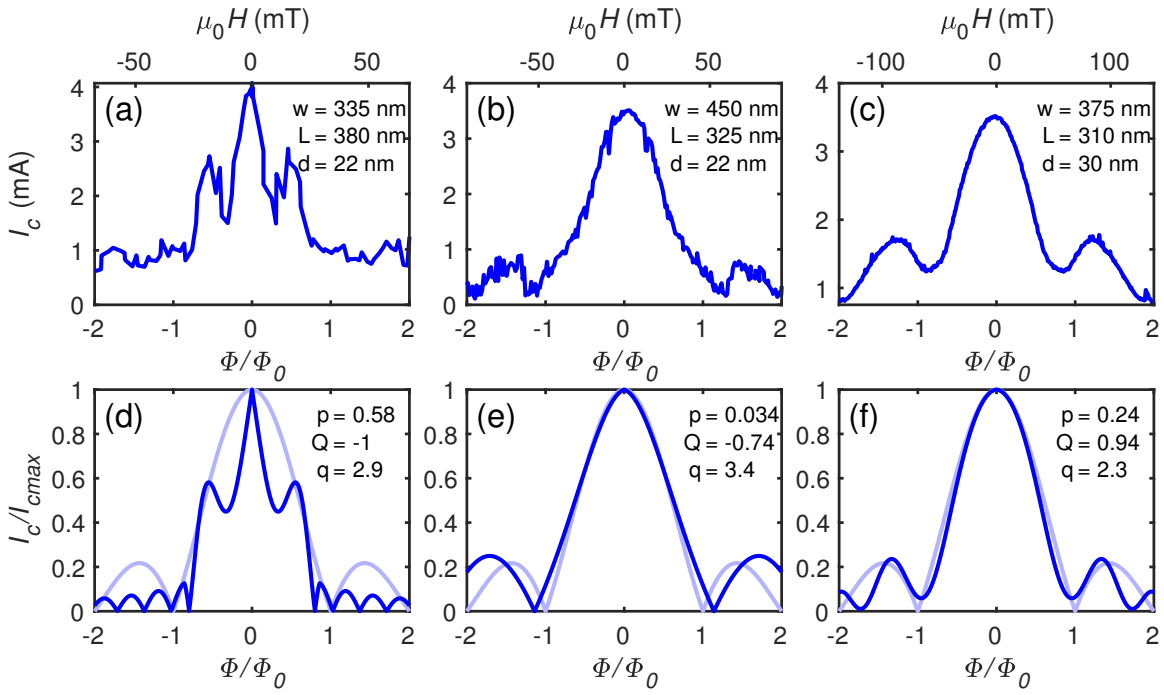

Fig. 9.4 Experimental (a-c) and calculated (d-f) $I_c(H)$ patterns normalised to $\phi_0 = 2.07 \times 10^{-15}$ Wb. The light blue curve in d-f show the standard Fraunhofer patter for comparison. The junction dimensions in a-c and the fitting parameters in d-f are labelled.

For the $d = 22$ nm junctions, fitting to $I_c(H)$ requires negative Q, which suggests that the supercurrent is flowing in the opposite directions in the ferromagnetic regions with respect to the antiferromagnetic region meaning the junction is in a simultaneous 0-π state. Previously, 0-π junctions were only created by varying the thickness of the magnetic layer in the barrier, where the change in barrier thickness changes the superconducting phase difference across the junction from 0 to π [158, 159]. The thickness change creates two fixed regions with 0 and π phase differences, whereas this model implies that these regions are magnetic field tuneable in Ho junctions.

9.5 Conclusions

A generalised model is presented to predict the behaviour of $I_c(H)$ patterns in magnetic Josephson junctions with a non-uniform magnetic susceptibility that peaks at junction edges. An analytical expression for $I_c(H)$ is derived and the key parameters which describe the shape of $I_c(H)$ are identified: the effective magnetic permeability q of the magnetised region; the propagation rate p of the magnetised region into the demagnetised region; and Q, the ratio of the local critical current density in the magnetised and demagnetised regions. The

calculations can be easily applied to understand the $I_c(H)$ behaviour magnetically complex Josephson junctions with simultaneous 0 and π states.

The model is fitted to experimental $I_c(H)$ patterns from highly-textured Nb/Ho/Nb junction. The theoretical curves manage to capture the main features of the measured data. The fitted value for q is close to the estimate from the magnetic measurements. The model implies that the $d = 22\,\text{nm}$ junctions are in a simultaneous 0-π state that is tuneable with the external magnetic field.

Part IV

Conclusions

Chapter 10

Summary

The interaction between superconductivity and magnetism provides a wealth of new physics and is a rapidly developing field of physics. The interaction hugely varies with the properties of each material as well as the interface and theoretical and experimental studies have been done on numerous systems. This thesis focuses on the Josephson coupling and the proximity effects through rare earth helimagnetic interfaces. The main results are summarised below.

A systematic study of the proximity effect in Nb/HoDy bilayers is presented in Chapter 7. The bilayers are successfully grown along the Nb (110) and RE (002) direction. The magnetic properties of the rare earth alloys are characterised at 10 K. The saturation magnetisation values agree with previously reported values for epitaxial Ho and Dy. Signs of the metastable magnetic spiral is observed up to 43 % Dy content, although the stability of the spiral varies with the Dy content. Increasing the Dy content broadens the magnetic field induced helimagnetic-ferromagnetic transition and shifts it towards higher field value indicating that Dy lowers the energy barrier and also decreases the energy difference between the two states in the low Dy content regime.

By applying increasingly large set magnetic fields, the transition temperature measured in zero field is suppressed. The field at which the T_c shift occurs is consistent with the field required to unwind the magnetic spiral of the rare earth alloy confirming that it is related to the helimagnetic-ferromagnetic transition. The magnitude of the shift decreases with Dy content. The remnant magnetisation of the alloys is significantly lower than the elements, which is most likely to be responsible for the majority of the reduction in the transition temperature shift. The Dy content can also shorten the electron mean-free-path and hence the superconducting coherence length in the rare earth layer. As the Cooper pairs only penetrate the rare earth layer over the coherence length, shortening it can reduce the effect of the

change of the magnetic state on the Nb layer contributing to the lowering of the transition temperature drop.

Chapter 8 presents measurements on textured Ho Josephson junctions and compares the results to previous measurements on polycrystalline junctions. Texturing the junctions decreases their resistivity and leads to a longer electron mean-free-path but it is still shorter than the normal metal coherence length meaning that the system is diffusive. The characteristic voltage of the textured junctions is an order of magnitude higher than that of the polycrystalline junctions and it decays with the barrier thickness much slower. The decay length is consistent with the dirty limit coherence length estimated for Ho.

The magnetic field dependence of the critical current shows some unusual behaviour including split peaks, concave central peaks and non-zero minima. To understand the origins of the $I_c(H)$ curves, a theoretical model is developed. The model assumes non-uniform magnetisation in the junction, that is higher near the edges and zero in the centre of the junction. The magnetised region penetrates towards the centre with increasing external field until the junction is fully magnetised. The model successfully reproduces the unusual features observed in the textured junctions. The fitting of the model suggests that the critical current flows in the opposite direction in the magnetised and demagnetised regions of the junctions with 22 nm barrier thickness. This implies that these junctions are in a magnetic field tuneable simultaneous 0-π state, which could be employed in superconducting logic gates.

In summary, we demonstrate that rare earth materials exhibit versatile magnetic properties at low temperatures that can benefit applications in superconducting devices. The low exchange field and negligible spin-polarisation makes it easy to study the proximity effect and make theoretical predictions using the Usadel equation. The interface is crucial in both the bilayers and the Josephson junctions. Moreover, texturing rare earth devices increases the Josephson effect and can lead to novel phenomena. Although the Usadel equation describes the spiral state well, the influence of the magnetic exchange field is lower in the magnetised state than expected, which requires further theoretical consideration.

Chapter 11

Future work

To further understand the interaction between the helimagnetic structures and superconductors, further research is required. A few potential directions are outlined below.

- **Magnetic characterisation of HoDy alloys using neutron diffraction**
  We use vibrating sample magnetometry for the magnetic characterisation of the rare earth layers. Neutron diffraction measurements could complement the VSM measurements and provide insight into the effects of Dy on the magnetic spiral and unwinding process.

- **Superconducting spin valves with HoDy alloys**
  Previously epitaxial Ho/Nb/Ho spin valves showed large change in T_c depending on the relative alignment of the magnetic layers. Adding Dy to the Ho layers of the spin valve most likely increases the resistivity. Measurements on spin valves with varying resistivity could help understand the reasons for the larger change in T_c in spin valves with ferromagnetic insulators.

- **Measure highly textured Ho Josephson junctions with higher barrier thicknesses**
  The high critical current measured in or junctions suggest that functioning Josephson junction can be fabricated with thicker barrier. The wider range of barrier thickness can help us better understand the effects of the magnetic spiral on the Josephson effect. However, the higher Ho thickness can also make it harder to grow highly textured junctions.

- **Investigate the magnetic properties of the nanopillar structures**
  The magnetic properties of the nanopillar structures can differ significantly from the unpatterned films measured in this work. Measuring the magnetic moment of a nanopillars on the sub-micron scale is difficult due the small signal. A possibility is

to fabricate an array of nanopillars using electron beam lithography and measure the magnetisation of the array using X-ray magnetic circular dichroism (XMCD). The size of the XMCD beam is normally around 1 mm in diameter therefore it could not be used to confirm the magnetisation process proposed in Chapter 9, however, it could highlight differences in coercive field and saturation magnetisation between the film and nanopillar.

- **Relate the parameters of the theoretical model to physical parameters**
  Systematically varying physical parameters, such as temperature, barrier thickness and junction dimensions, and relating them to the theoretical parameters p, q and Q from the $I_c(H)$ fits can show insight to the physics of helimagnetic junctions and build knowledge to design structures for computing purposes. Adding Dy to the Ho barrier can also be used to control the resistivity and exchange field of the magnetic layer.

- **Study highly textured Ho junctions in perpendicular magnetic field**
  A magnetic field perpendicular to the barrier layer induces an out-of-plane magnetisation component to magnetic spiral of Ho making it a conical magnetic structure. The conical structure introduces chirality to the junction therefore breaking the symmetry between the two current direction. This asymetry might affect junction properties such as I_c and deform the IV curves.

References

[1] Thomas, H. *et al.* Superconducting transmission lines - Sustainable electric energy transfer with higher public acceptance? (2016).

[2] Holmes, D. S., Ripple, A. L. & Manheimer, M. A. Energy-Efficient Superconducting Computing—Power Budgets and Requirements. *IEEE Transactions on Applied Superconductivity* **23**, 1701610–1701610 (2013).

[3] Chen, W., Rylyakov, A., Patel, V., Lukens, J. E. & Likharev, K. K. Rapid Single Flux Quantum T-flip flop operating up to 770 GHz. *Applied Superconductivity, IEEE Transactions on* **9**, 3212–3215 (1999).

[4] Yamashita, T., Tanikawa, K., Takahashi, S. & Maekawa, S. Superconducting π qubit with a ferromagnetic Josephson junction. *Physical Review Letters* **95** (2005).

[5] Linder, J. & Robinson, J. W. A. Superconducting spintronics. *Nature Physics* **11**, 307–315 (2015). URL http://www.nature.com/articles/nphys3242.

[6] Robinson, J. W. A., Witt, J. D. S. & Blamire, M. G. Controlled Injection of Spin-Triplet Supercurrents into a Strong Ferromagnet. *Science* **329**, 59–61 (2010).

[7] Onnes, H. K. The resistance of pure mercury at helium temperatures. *Commun. Phys. Lab. Univ. Leiden* **12**, 1 (1911).

[8] Meissner, W. & Ochsenfeld, R. Ein neuer effekt bei eintritt der supraleitfähigkeit. *Naturwissenschaften* **21**, 787–788 (1933).

[9] Ginzburg, V. L. & Landau, L. D. On the theory of superconductivity. *Zh. Eksp. Teor. Fiz.* **20**, 1064 (1950).

[10] Bardeen, J., Cooper, L. N. & Schrieffer, J. R. Theory of Superconductivity. *Phys. Rev.* **108**, 1175–1204 (1957). URL http://link.aps.org/doi/10.1103/PhysRev.108.1175.

[11] Landau, L. D. On the theory of phase transitions. I. *Zh. Eksp. Teor. Fiz.* **11**, 19 (1937).

[12] London, F. & London, H. The electromagnetic equations of the supraconductor. *Proceedings of the Royal Society of London. Series A - Mathematical and Physical Sciences* **149**, 71–88 (2006). URL http://www.royalsocietypublishing.org/doi/10.1098/rspa.1935.0048.

[13] W.Clark, R. *Einstein : the life and times* (Hodder and Stoughton, 1973).

[14] London, F. The λ-Phenomenon of Liquid Helium and the Bose-Einstein Degeneracy. *Nature* **141**, 643–644 (1938).

[15] Bogoliubov, N. N. On the theory of superfluidity. *J. Phys.(USSR)* **11**, 23–32 (1947).

[16] Bogoliubov, N. N. On a New method in the theory of superconductivity. *Nuovo Cim.* **7**, 794–805 (1958).

[17] Gor'kov, L. P. Microscopic Derivation of the Ginzburg-Landau Equations in the Theory of Superconductivity. *Zh. Eksp. Teor. Fiz.* **9**, 1364–1367 (1959).

[18] Meissner, H. Superconductivity of contacts with interposed barriers. *Physical Review* **117**, 672–680 (1960). URL https://link.aps.org/doi/10.1103/PhysRev.117.672.

[19] Deutscher, G. & De Gennes, P. G. Proximity Effects. In Parks, R. D. (ed.) *Superconductivity vol 2*, 1005–1033 (Marcel Dekker, 1969).

[20] De Gennes, P. G. *Superconductivity of Metals and Alloys* (CRC Press, 1999). URL https://www.taylorfrancis.com/books/9780429497032.

[21] Usadel, K. D. Generalized Diffusion Equation for Superconducting Alloys. *Phys. Rev. Lett.* **25**, 507–509 (1970). URL https://link.aps.org/doi/10.1103/PhysRevLett.25.507.

[22] Kuprianov, M. Y. & Lukichev, V. F. Influence of boundary transparency on the critical current of "dirty". *Sov. Phys. JETP* **67**, 1163 (1988). URL http://www.jetp.ac.ru/cgi-bin/e/index/e/67/6/p1163?a=list.

[23] Andreev, A. F. The thermal conductivity of the intermadiate state in superconductors. *Soviet Physics JETP* **19**, 1228 (1964). URL http://www.jetp.ac.ru/cgi-bin/dn/e_019_05_1228.pdf.

[24] Josephson, B. Possible new effects in superconductive tunnelling. *Physics Letters* **1**, 251–253 (1962). URL https://www.sciencedirect.com/science/article/pii/0031916362913690?via%3Dihubhttp://linkinghub.elsevier.com/retrieve/pii/0031916362913690https://www.sciencedirect.com/science/article/pii/0031916362913690https://linkinghub.elsevier.com/retrieve/pii/0031.

[25] Anderson, P. W. & Rowell, J. M. Probable Observation of the Josephson Superconducting Tunneling Effect. *Physical Review Letters* **10**, 230–232 (1963). URL https://link.aps.org/doi/10.1103/PhysRevLett.10.230.

[26] Rowell, J. M. Magnetic field dependence of the Josephson tunnel current. *Physical Review Letters* **11**, 200–202 (1963). URL https://link.aps.org/doi/10.1103/PhysRevLett.11.200.

[27] Yanson, I., Svistunov, V. & Dmitrenko, I. Experimental observation of Cooper pair tunneling between thin layers of superconducting tin. *Sov. Phys. JETP* **165**, 650–652 (1965). URL http://www.jetp.ac.ru/cgi-bin/e/index/e/20/6/p1404?a=listhttp://www.jetp.ac.ru/cgi-bin/dn/e_020_06_1404.pdf%5Cnhttp://www.jetp.ac.ru/cgi-bin/dn/e_021_03_0650.pdf.

[28] Waldram, J. R. *Superconductivity of metals and cuprates* (CRC Press, 1996).

[29] Cohen, M. H., Falicov, L. M. & Phillips, J. C. Superconductive Tunneling. *Physical Review Letters* **8**, 316–318 (1962). URL https://link.aps.org/doi/10.1103/PhysRevLett.8.316.

[30] Ambegaokar, V. & Baratoff, A. Tunneling Between Superconductors. *Physical Review Letters* **10**, 486–489 (1963). URL https://link.aps.org/doi/10.1103/PhysRevLett.10.486.

[31] De Gennes, P. G. Boundary Effects in Superconductors. In *Reviews of Modern Physics*, vol. 36, 225–237 (American Physical Society, 1964). URL https://link.aps.org/doi/10.1103/RevModPhys.36.225.

[32] Buzdin, A. & Koshelev, A. E. Periodic alternating 0- and π-junction structures as realization of φ-Josephson junctions. *Phys. Rev. B* **67**, 220504 (2003). URL https://link.aps.org/doi/10.1103/PhysRevB.67.220504.

[33] Tinkham, M. *Introduction to superconductivity* (Dover Publications, 1994). URL https://books.google.co.uk/books/about/Introduction_to_Superconductivity.html?id=JOQoAwAAQBAJ&printsec=frontcover&source=kp_read_button&redir_esc=y#v=onepage&q&f=false.

[34] Yanson, I. Effect of Fluctuations on the Dependence of the Josephson Current on the Magnetic Field. *Soviet Journal of Experimental and Theoretical Physics* **31**, 800 (1970). URL http://jetp.ac.ru/cgi-bin/e/index/e/31/5/p800?a=list.

[35] Barone, A. & Paternò, G. *Physics and Applications of the Josephson Effect* (Wiley and Sons Inc, Weinheim, 1982). URL http://doi.wiley.com/10.1002/352760278X.

[36] Heisenberg, W. Zur Theorie des Ferromagnetismus. *Zeitschrift für Physik* **49**, 619–636 (1928). URL http://link.springer.com/10.1007/BF01328601.

[37] Weiss, P. L'hypothèse du champ moléculaire et la propriété ferromagnétique. *Journal de Physique Théorique et Appliquée* **6**, 661–690 (1907). URL http://www.edpsciences.org/10.1051/jphystap:019070060066100.

[38] Chikazumi, S. *Physics of magnetism* (R.E. Krieger Pub. Co, 1978).

[39] Hubbard, J. Electron correlations in narrow energy bands. *Proceedings of the Royal Society of London. Series A. Mathematical and Physical Sciences* **276**, 238–257 (1963). URL http://www.royalsocietypublishing.org/doi/10.1098/rspa.1963.0204.

[40] Anderson, P. W. Antiferromagnetism. Theory of superexchange interaction. *Physical Review* **79**, 350–356 (1950). URL https://link.aps.org/doi/10.1103/PhysRev.79.350.

[41] Stoner, E. C. Collective electron specific heat and spin paramagnetism in metals. *Proceedings of the Royal Society of London. Series A - Mathematical and Physical Sciences* **154**, 656–678 (1936). URL http://www.royalsocietypublishing.org/doi/10.1098/rspa.1936.0075.

[42] Blundell, S. *Magnetism in condensed matter* (Oxford University Press, 2001).

[43] Ruderman, M. A. & Kittel, C. Indirect Exchange Coupling of Nuclear Magnetic Moments by Conduction Electrons. *Physical Review* **96**, 99–102 (1954). URL https://link.aps.org/doi/10.1103/PhysRev.96.99.

[44] Kasuya, T. A Theory of Metallic Ferro- and Antiferromagnetism on Zener's Model. *Progress of Theoretical Physics* **16**, 45–57 (1956). URL https://academic.oup.com/ptp/article-lookup/doi/10.1143/PTP.16.45.

[45] Yosida, K. Magnetic Properties of Cu-Mn Alloys. *Physical Review* **106**, 893–898 (1957). URL https://link.aps.org/doi/10.1103/PhysRev.106.893.

[46] Soulen, R. J. *et al.* Measuring the spin polarization of a metal with a superconducting point contact. *Science* **282**, 85–88 (1998).

[47] Witt, J. D. S. *et al.* Strain dependent selection of spin-slip phases in sputter deposited thin-film epitaxial holmium. *Journal of Physics: Condensed Matter* **23**, 416006 (2011). URL http://stacks.iop.org/0953-8984/23/i=41/a=416006?key=crossref.c6de799946ef0114186924b9c91de18a.

[48] Gu, Y. *et al.* Magnetic state controllable critical temperature in epitaxial Ho/Nb bilayers. *APL Materials* **2**, 046103 (2014). URL http://aip.scitation.org/doi/10.1063/1.4870141.

[49] Koehler, W. C., Cable, J. W., Child, H. R., Wilkinson, M. K. & Wollan, E. O. Magnetic Structures of Holmium. II. The Magnetization Process. *Physical Review* **158**, 450–461 (1967). URL https://link.aps.org/doi/10.1103/PhysRev.158.450.

[50] Safrata, R. S., Fisher, T. R. & Shelley, E. G. Magnetic Hysteresis of Holmium Metal at 4.2°K. *Journal of Applied Physics* **37**, 4869–4872 (1966). URL http://aip.scitation.org/doi/10.1063/1.1708153.

[51] Koehler, W. C. Magnetic Structures of Rare Earth Metals and Alloys. In *Magnetic Properties of Rare Earth Metals*, 81–128 (Springer US, Boston, MA, 1972). URL http://link.springer.com/10.1007/978-1-4757-5691-3_3.

[52] Behrendt, D. R., Legvold, S. & Spedding, F. H. Magnetic Properties of Dysprosium Single Crystals. *Physical Review* **109**, 1544–1547 (1958). URL https://link.aps.org/doi/10.1103/PhysRev.109.1544.

[53] Wilkinson, M. K., Koehler, W. C., Wollan, E. O. & Cable, J. W. Neutron Diffraction Investigation of Magnetic Ordering in Dysprosium. *Journal of Applied Physics* **32**, S48–S49 (1961). URL http://aip.scitation.org/doi/10.1063/1.2000493.

[54] Jordan, R. G. & Lee, E. W. Low-temperature magnetic properties of dysprosium single crystals. *Proceedings of the Physical Society* **92**, 1074–1082 (1967). URL http://stacks.iop.org/0370-1328/92/i=4/a=331?key=crossref.79dc0e80a518f6a865ee5ee9c1f0900c.

[55] Strandburg, D. L., Legvold, S. & Spedding, F. H. Electrical and Magnetic Properties of Holmium Single Crystals. *Physical Review* **127**, 2046–2051 (1962). URL https://link.aps.org/doi/10.1103/PhysRev.127.2046.

[56] Dubonos, S. V., Geim, A. K., Novoselov, K. S. & Grigorieva, I. V. Spontaneous magnetization changes and nonlocal effects in mesoscopic ferromagnet-superconductor structures. *Physical Review B - Condensed Matter and Materials Physics* **65**, 1–4 (2002).

[57] Zhu, Y., Pal, A., Blamire, M. G. & Barber, Z. H. Superconducting exchange coupling between ferromagnets. *Nature Materials* **16**, 195–199 (2017). URL http://www.nature.com/articles/nmat4753.

[58] Buzdin, A. I. Proximity effects in superconductor-ferromagnet heterostructures. *Reviews of Modern Physics* **77**, 935–976 (2005). URL https://link.aps.org/doi/10.1103/RevModPhys.77.935.

[59] Buzdin, A. I. & Kupriyanov, M. Y. Transition temperature of a superconductor-ferromagnet superlattice. *JETP Letters* **52**, 487–491 (1990).

[60] Radović, Z., Ledvij, M., Dobrosavljević-Grujić, L., Buzdin, A. I. & Clem, J. R. Transition temperatures of superconductor-ferromagnet superlattices. *Phys. Rev. B* **44**, 759–764 (1991). URL https://link.aps.org/doi/10.1103/PhysRevB.44.759.

[61] Jiang, J. S., Davidović, D., Reich, D. H. & Chien, C. L. Oscillatory Superconducting Transition Temperature in Nb/Gd Multilayers. *Phys. Rev. Lett.* **74**, 314–317 (1995). URL https://link.aps.org/doi/10.1103/PhysRevLett.74.314.

[62] Mercaldo, L. V. *et al.* Superconducting-critical-temperature oscillations in Nb/CuMn multilayers. *Phys. Rev. B* **53**, 14040–14042 (1996). URL https://link.aps.org/doi/10.1103/PhysRevB.53.14040.

[63] Obi, Y., Ikebe, M., Kubo, T. & Fujimori, H. Oscillation phenomenon of transition temperatures in Nb/Co and V/Co superconductor/ferromagnet multilayers. *Physica C: Superconductivity and its Applications* **317-318**, 149–153 (1999).

[64] Mühge, T. *et al.* Possible Origin for Oscillatory Superconducting Transition Temperature in Superconductor/Ferromagnet Multilayers. *Phys. Rev. Lett.* **77**, 1857–1860 (1996). URL https://link.aps.org/doi/10.1103/PhysRevLett.77.1857.

[65] Lazar, L. *et al.* Superconductor/ferromagnet proximity effect in Fe/Pb/Fe trilayers. *Phys. Rev. B* **61**, 3711–3722 (2000). URL https://link.aps.org/doi/10.1103/PhysRevB.61.3711.

[66] Garifullin, I. A. Proximity effects in ferromagnet/superconductor heterostructures. *Journal of Magnetism and Magnetic Materials* **240**, 571–576 (2002).

[67] Sidorenko, A. *et al.* Oscillations of the critical temperature in superconducting Nb/Ni bilayers. *Annalen der Physik* **12**, 37–50 (2003).

[68] Strunk, C., Sürgers, C., Paschen, U. & Löhneysen, H. v. Superconductivity in layered Nb/Gd films. *Phys. Rev. B* **49**, 4053–4063 (1994). URL https://link.aps.org/doi/10.1103/PhysRevB.49.4053.

[69] Bulaevskii, L. N., Kuzii, V. V. & Sobyanin, A. A. Superconducting system with weak coupling to the current in the ground state. *Journal of Experimental and Theoretical Physics Letters* **25**, 290–294 (1977). URL http://www.jetpletters.ac.ru/ps/1410/article_21163.pdf.

[70] Bauer, A. *et al.* Spontaneous supercurrent induced by ferromagnetic π junctions. *Physical Review Letters* **92** (2004).

[71] Ryazanov, V. V., Oboznov, V. A. & Veretennikov, A. V. Intrinsically frustrated superconducting array of superconductor-ferromagnet-superconductor πjunctions. *Physical Review B - Condensed Matter and Materials Physics* **65**, 1–4 (2001).

[72] Guichard, W. *et al.* Phase Sensitive Experiments in Ferromagnetic-Based Josephson Junctions. *Physical Review Letters* **90**, 4 (2003).

[73] Buzdin, A. I., Bulaevskil, L. N. & Panyukov, S. V. Critical-current oscillations as a function of the exchange field and thickness of the ferromagnetic metal (F) in an S-F-S Josephson junction. *Journal of Experimental and Theoretical Physics Letters* **35**, 178 (1982). URL http://jetpletters.ac.ru/ps/1314/article_19853.pdf.

[74] Buzdin, A. I. & Kupriyanov, M. Y. Josephson junction with a ferromagnetic layer. *Journal of Experimental and Theoretical Physics Letters1* **53**, 321–326 (1991).

[75] Ryazanov, V. V. *et al.* Coupling of two superconductors through a ferromagnet: Evidence for a πjunction. *Physical Review Letters* **86**, 2427–2430 (2001). URL https://link.aps.org/doi/10.1103/PhysRevLett.86.2427. 0008364.

[76] Radović, Z., Lazarides, N. & Flytzanis, N. Josephson effect in double-barrier superconductor-ferromagnet junctions. *Phys. Rev. B* **68**, 14501 (2003). URL https://link.aps.org/doi/10.1103/PhysRevB.68.014501.

[77] Golubov, A. A., Kupriyanov, M. Y. & Il'ichev, E. The current-phase relation in Josephson junctions (2004).

[78] Cayssol, J. & Montambaux, G. Incomplete Andreev reflection in a clean superconductor-ferromagnet- superconductor junction. *Physical Review B - Condensed Matter and Materials Physics* **71** (2005).

[79] Chtchelkatchev, N. M., Belzig, W., Nazarov, Y. V. & Bruder, C. π-0 transition in superconductor-ferromagnet-superconductor junctions. *Journal of Experimental and Theoretical Physics Letters* **74**, 323–327 (2001). URL https://doi.org/10.1134/1.1421408.

[80] Zyuzin, A. & Spivak, B. Theory of $\pi/2$ superconducting Josephson junctions. *Phys. Rev. B* **61**, 5902–5904 (2000). URL https://link.aps.org/doi/10.1103/PhysRevB.61.5902.

[81] Bergeret, F. S., Volkov, A. F. & Efetov, K. B. Long-range proximity effects in superconductor-ferromagnet structures. *Physical Review Letters* **86**, 4096–4099 (2001). URL https://link.aps.org/doi/10.1103/PhysRevLett.86.4096. 0011425.

[82] Kadigrobov, A., Shekhter, R. I. & Jonson, M. Quantum spin fluctuations as a source of long-range proximity effects in diffusive ferromagnet-superconductor structures. *Europhysics Letters* **54**, 394–400 (2001). URL http://stacks.iop.org/0295-5075/54/i=3/a=394?key=crossref.a65976b8155d52553a1479a36a56987a. 0012437v1.

[83] Eschrig, M. Spin-polarized supercurrents for spintronics. *Physics Today* (2011).

[84] Keizer, R. S. *et al.* A spin triplet supercurrent through the half-metallic ferromagnet CrO 2. *Nature* **439**, 825–827 (2006). URL http://www.nature.com/articles/nature04499. 0602359.

[85] Khaire, T. S., Khasawneh, M. A., Pratt, W. P. & Birge, N. O. Observation of Spin-Triplet Superconductivity in Co-Based Josephson Junctions. *Physical Review Letters* **104**, 137002 (2010). URL https://link.aps.org/doi/10.1103/PhysRevLett.104.137002.

[86] Robinson, J. W. A., Witt, J. D. S. & Blamire, M. G. Controlled injection of spin-triplet supercurrents into a strong ferromagnet. *Science (New York, N.Y.)* **329**, 59–61 (2010). URL http://www.ncbi.nlm.nih.gov/pubmed/20538913.

[87] Hauser, J. J. Coupling Between Ferrimagnetic Insulators Through a Superconducting Layer. *Phys. Rev. Lett.* **23**, 374–377 (1969). URL https://link.aps.org/doi/10.1103/PhysRevLett.23.374.

[88] Li, B. *et al.* Superconducting Spin Switch with Infinite Magnetoresistance Induced by an Internal Exchange Field. *Phys. Rev. Lett.* **110**, 97001 (2013). URL http://link.aps.org/doi/10.1103/PhysRevLett.110.097001.

[89] Deutscher, G. & Meunier, F. Coupling Between Ferromagnetic Layers Through a Superconductor. *Phys. Rev. Lett.* **22**, 395–396 (1969). URL https://link.aps.org/doi/10.1103/PhysRevLett.22.395.

[90] Miao, G.-X., Yoon, K., Santos, T. S. & Moodera, J. S. Influence of Spin-Polarized Current on Superconductivity and the Realization of Large Magnetoresistance. *Phys. Rev. Lett.* **98**, 267001 (2007). URL http://link.aps.org/doi/10.1103/PhysRevLett.98.267001.

[91] Miao, G.-X., Ramos, A. V. & Moodera, J. S. Infinite Magnetoresistance from the Spin Dependent Proximity Effect in Symmetry Driven bcc - Fe/V/Fe Heteroepitaxial Superconducting Spin Valves. *Phys. Rev. Lett.* **101**, 137001 (2008). URL http://link.aps.org/doi/10.1103/PhysRevLett.101.137001.

[92] Moraru, I. C., Pratt, W. P. & Birge, N. O. Magnetization-dependent Tc shift in ferromagnet/superconductor/ferromagnet trilayers with a strong ferromagnet. *Physical Review Letters* **96** (2006).

[93] Potenza, A. & Marrows, C. H. Superconductor-ferromagnet CuNi/Nb/CuNi trilayers as superconducting spin-valve core structures. *Phys. Rev. B* **71**, 180503 (2005). URL http://link.aps.org/doi/10.1103/PhysRevB.71.180503.

[94] Gu, J. Y. *et al.* Magnetization-Orientation Dependence of the Superconducting Transition Temperature in the Ferromagnet-Superconductor-Ferromagnet System: CuNi/Nb/CuNi. *Phys. Rev. Lett.* **89**, 267001 (2002). URL http://link.aps.org/doi/10.1103/PhysRevLett.89.267001.

[95] Gu, Y., Halász, G. B., Robinson, J. W. A. & Blamire, M. G. Large Superconducting Spin Valve Effect and Ultrasmall Exchange Splitting in Epitaxial Rare-Earth-Niobium Trilayers. *Physical Review Letters* **115** (2015).

[96] Wang, X. L. *et al.* Giant triplet proximity effect in superconducting pseudo spin valves with engineered anisotropy. *Physical Review B - Condensed Matter and Materials Physics* **89**, 140508 (2014). URL https://link.aps.org/doi/10.1103/PhysRevB.89.140508.

[97] Leksin, P. V. *et al.* Evidence for Triplet Superconductivity in a Superconductor-Ferromagnet Spin Valve. *Phys. Rev. Lett.* **109**, 57005 (2012). URL http://link.aps.org/doi/10.1103/PhysRevLett.109.057005.

[98] Buzdin, A. I., Vedyayev, A. V. & Ryzhanova, N. V. Spin-orientation-dependent superconductivity in F/S/F structures. *EPL (Europhysics Letters)* **48**, 686 (1999). URL http://stacks.iop.org/0295-5075/48/i=6/a=686.

[99] Tagirov, L. R. Low-Field Superconducting Spin Switch Based on a Superconductor /Ferromagnet Multilayer. *Phys. Rev. Lett.* **83**, 2058–2061 (1999). URL http://link.aps.org/doi/10.1103/PhysRevLett.83.2058.

[100] Peña, V. *et al.* Giant Magnetoresistance in Ferromagnet/Superconductor Superlattices. *Phys. Rev. Lett.* **94**, 57002 (2005). URL http://link.aps.org/doi/10.1103/PhysRevLett.94.057002.

[101] Stamopoulos, D., Manios, E. & Pissas, M. Stray-fields-based magnetoresistance mechanism in $Ni_{80}Fe_{20}$-Nb-$Ni_{80}Fe_{20}$ trilayered hybrids. *Phys. Rev. B* **75**, 184504 (2007). URL http://link.aps.org/doi/10.1103/PhysRevB.75.184504.

[102] Fominov, Y. V. *et al.* Superconducting triplet spin valve. *JETP Letters* **91**, 308–313 (2010). URL http://link.springer.com/10.1134/S002136401006010X.

[103] Ohring, M. *The Materials Science of Thin Films* (Academic Press, 2001).

[104] Thornton, J. A. & Penfold, A. S. Cylindrical Magnetron Sputtering. In Vossen, J. L. & Kern, W. (eds.) *Thin Film Processes*, 75–113 (Academic Press, San Diego, 1978). URL http://www.sciencedirect.com/science/article/pii/B9780127282503500076.

[105] Gutekunst, G., Mayer, J. & Rühle, M. Atomic structure of epitaxial Nb-Al2O3 interfaces I. Coherent regions. *Philosophical Magazine A* **75**, 1329–1355 (1997). URL http://dx.doi.org/10.1080/01418619708209859.

[106] Kwo, J., Hong, M. & Nakahara, S. Growth of rare-earth single crystals by molecular beam epitaxy: The epitaxial relationship between hcp rare earth and bcc niobium. *Applied Physics Letters* **49** (1986). URL http://scitation.aip.org/content/aip/journal/apl/49/6/10.1063/1.97155.

[107] Mack, C. *Fundamental Principles of Optical Lithography: The Science of Microfabrication* (John Wiley and Sons, 2007).

[108] Cox, D. C. *Introduction to focused ion beam nanometrology* (IOP Publishing Ltd, 2015).

[109] Kim, S. J., Latyshev, Y. I. & Yamashita, T. Submicron stacked-junction fabrication from Bi_2Sr_2CaCu_2O_8+δ whiskers by focused-ion-beam etching. *Applied Physics Letters* **74**, 1156–1158 (1999).

[110] Kim, S.-J., Latyshev, Y., Yamashita, T. & Kishida, S. New approach for fabricating submicron scale intrinsic Josephson junctions using high-T_c superconducting materials. *Physica C: Superconductivity* **362**, 150–155 (2001). URL http://www.sciencedirect.com/science/article/pii/S0921453401006621.

[111] Bell, C. *et al.* Fabrication of nanoscale heterostructure devices with a focused ion beam microscope. *Nanotechnology* **14**, 630–632 (2003). URL http://stacks.iop.org/0957-4484/14/i=6/a=312?key=crossref.392c0d6e5fba0b8e4a5a839014c23d75.

[112] Patterson, A. L. The Scherrer Formula for X-Ray Particle Size Determination. *Phys. Rev.* **56**, 978–982 (1939). URL https://link.aps.org/doi/10.1103/PhysRev.56.978.

[113] Foner, S. Versatile and Sensitive Vibrating Sample Magnetometer. *Review of Scientific Instruments* **30**, 548–557 (1959). URL http://scitation.aip.org/content/aip/journal/rsi/30/7/10.1063/1.1716679.

[114] Ustinov, A. V. & Kaplunenko, V. K. Rapid single-flux quantum logic using π-shitters. *Journal of Applied Physics* **94**, 5405–5407 (2003).

[115] Kalcheim, Y., Millo, O., Egilmez, M., Robinson, J. W. A. & Blamire, M. G. Evidence for anisotropic triplet superconductor order parameter in half-metallic ferromagnetic $La_{0.7}Ca_{0.3}Mn_3O$ proximity coupled to superconducting $Pr_{1.85}Ce_{0.15}CuO_4$. *Physical Review B - Condensed Matter and Materials Physics* **85**, 104504 (2012). URL https://link.aps.org/doi/10.1103/PhysRevB.85.104504.

[116] Kalcheim, Y. *et al.* Magnetic field dependence of the proximity-induced triplet superconductivity at ferromagnet/superconductor interfaces. *Physical Review B* **89**, 180506 (2014). URL https://link.aps.org/doi/10.1103/PhysRevB.89.180506.

[117] Kalcheim, Y., Millo, O., Di Bernardo, A., Pal, A. & Robinson, J. W. A. Inverse proximity effect at superconductor-ferromagnet interfaces: Evidence for induced triplet pairing in the superconductor. *Physical Review B* **92**, 060501 (2015). URL https://link.aps.org/doi/10.1103/PhysRevB.92.060501.

[118] Moussy, N., Courtois, H. & Pannetier, B. Local spectroscopy of a proximity superconductor at very low temperature. *Europhysics Letters* **55**, 861–867 (2001).

[119] Kontos, T., Aprili, M., Lesueur, J. & Grison, X. Inhomogeneous Superconductivity Induced in a Ferromagnet by Proximity Effect. *Phys. Rev. Lett.* **86**, 304–307 (2001). URL https://link.aps.org/doi/10.1103/PhysRevLett.86.304.

[120] Vélez, M., Cyrille, M. C., Kim, S., Vicent, J. L. & Schuller, I. K. Enhancement of superconductivity by decreased magnetic spin-flip scattering: Nonmonotonic T_c dependence with enhanced magnetic ordering. *Physical Review B - Condensed Matter and Materials Physics* **59**, 14659–14662 (1999).

[121] Chien, C. L. & Reich, D. H. Proximity effects in superconducting/magnetic multilayers. *Journal of Magnetism and Magnetic Materials* **200**, 83–94 (1999).

[122] Satchell, N. *et al.* Control of Superconductivity with a Single Ferromagnetic Layer in Niobium/Erbium Bilayers. *Phys. Rev. Applied* **7**, 44031 (2017). URL https://link.aps.org/doi/10.1103/PhysRevApplied.7.044031.

[123] Tomy, C. V., Balakrishnan, G. & Paul, D. M. Observation of the peak effect in the superconductor $Ca_3Rh_4Sn_{13}$. *Phys. Rev. B* **56**, 8346–8350 (1997). URL https://link.aps.org/doi/10.1103/PhysRevB.56.8346.

[124] Tang, C., Ling, X., Bhattacharya, S. & Chaikin, P. M. Peak effect in superconductors: melting of Larkin domains. *Europhysics Letters (EPL)* **35**, 597–602 (1996). URL https://doi.org/10.1209%2Fepl%2Fi1996-00157-x.

[125] Rao, K. V. Nuclear Hyperfine Contribution to Thermal Conductivity of Holmium. *Physical Review Letters* **22**, 943–945 (1969). URL https://link.aps.org/doi/10.1103/PhysRevLett.22.943.

[126] Eschrig, M. Spin-polarized supercurrents for spintronics. *Physics Today* **64**, 43–49 (2011). URL http://scitation.aip.org/content/aip/magazine/physicstoday/article/64/1/10.1063/1.3541944. 1509.02242.

[127] Eschrig, M. Theory of Andreev bound states in S-F-S junctions and S-F proximity devices. *Philosophical Transactions of the Royal Society A: Mathematical, Physical and Engineering Sciences* **376**, 20150149 (2018). URL http://rsta.royalsocietypublishing.org/lookup/doi/10.1098/rsta.2015.0149.

[128] Weides, M. Magnetic anisotropy in ferromagnetic Josephson junctions. *Applied Physics Letters* **93**, 052502 (2008). URL http://aip.scitation.org/doi/10.1063/1.2967873.

[129] Kontos, T. *et al.* Josephson Junction through a Thin Ferromagnetic Layer: Negative Coupling. *Physical Review Letters* **89**, 137007 (2002). URL https://link.aps.org/doi/10.1103/PhysRevLett.89.137007https://journals.aps.org/prl/pdf/10.1103/PhysRevLett.89.137007. 0201104v2.

[130] Robinson, J. W. A., Barber, Z. H. & Blamire, M. G. Strong ferromagnetic Josephson devices with optimized magnetism. *Applied Physics Letters* **95**, 192509 (2009). URL http://aip.scitation.org/toc/apl/95/19.

[131] Bell, C., Loloee, R., Burnell, G. & Blamire, M. G. Characteristics of strong ferromagnetic Josephson junctions with epitaxial barriers. *Physical Review B - Condensed Matter and Materials Physics* **71**, 180501 (2005). URL https://link.aps.org/doi/10.1103/PhysRevB.71.180501. 0502537.

[132] Halász, G. B., Blamire, M. G. & Robinson, J. W. A. Magnetic-coupling-dependent spin-triplet supercurrents in helimagnet/ferromagnet Josephson junctions. *Physical Review B* **84**, 024517 (2011). URL https://link.aps.org/doi/10.1103/PhysRevB.84.024517.

[133] Robinson, J. W. A., Halász, G. B., Buzdin, A. I. & Blamire, M. G. Enhanced supercurrents in josephson junctions containing nonparallel ferromagnetic domains. *Physical Review Letters* **104**, 207001 (2010). URL https://link.aps.org/doi/10.1103/PhysRevLett.104.207001.

[134] Klose, C. *et al.* Optimization of Spin-Triplet Supercurrent in Ferromagnetic Josephson Junctions. *Physical Review Letters* **108**, 127002 (2012). URL https://link.aps.org/doi/10.1103/PhysRevLett.108.127002.

[135] Banerjee, N., Robinson, J. & Blamire, M. G. Reversible control of spin-polarized supercurrents in ferromagnetic Josephson junctions. *Nature Communications* **5**, 4771 (2014). URL http://www.nature.com/articles/ncomms5771.

[136] Sprungmann, D., Westerholt, K., Zabel, H., Weides, M. & Kohlstedt, H. Evidence for triplet superconductivity in Josephson junctions with barriers of the ferromagnetic Heusler alloy Cu 2 MnAl. *Physical Review B* **82**, 060505 (2010). URL https://link.aps.org/doi/10.1103/PhysRevB.82.060505.

[137] Witt, J. D. S., Robinson, J. W. A. & Blamire, M. G. Josephson junctions incorporating a conical magnetic holmium interlayer. *Physical Review B* **85**, 184526 (2012). URL https://link.aps.org/doi/10.1103/PhysRevB.85.184526.

[138] Bergeret, F. S., Volkov, A. F. & Efetov, K. B. Odd triplet superconductivity and related phenomena in superconductor- ferromagnet structures. *Reviews of Modern Physics* **77**, 1321–1373 (2005). URL https://link.aps.org/doi/10.1103/RevModPhys.77.1321.0506047.

[139] Eschrig, M. & Löfwander, T. Triplet supercurrents in clean and disordered half-metallic ferromagnets. *Nature Physics* **4**, 138–143 (2008). URL http://www.nature.com/articles/nphys831.

[140] Oboznov, V. A., Bol'ginov, V. V., Feofanov, A. K., Ryazanov, V. V. & Buzdin, A. I. Thickness Dependence of the Josephson Ground States of Superconductor-Ferromagnet-Superconductor Junctions. *Physical Review Letters* **96**, 197003 (2006). URL https://link.aps.org/doi/10.1103/PhysRevLett.96.197003.

[141] Weides, M. *et al.* High quality ferromagnetic 0 and π Josephson tunnel junctions. *Applied Physics Letters* **89**, 122511 (2006). URL http://aip.scitation.org/doi/10.1063/1.2356104.

[142] Born, F. *et al.* Multiple 0-π transitions in superconductor/insulator/ferromagnet/superconductor Josephson tunnel junctions. *Physical Review B - Condensed Matter and Materials Physics* **74**, 140501 (2006). URL https://link.aps.org/doi/10.1103/PhysRevB.74.140501.

[143] Robinson, J. W., Piano, S., Burnell, G., Bell, C. & Blamire, M. G. Critical current oscillations in strong ferromagnetic π junctions. *Physical Review Letters* **97** (2006). URL https://journals.aps.org/prl/pdf/10.1103/PhysRevLett.97.177003. 0606067.

[144] Piano, S., Robinson, J. W., Burnell, G. & Blamire, M. G. 0-π oscillations in nanostructured Nb/Fe/Nb Josephson junctions. *The European Physical Journal B* **58**, 123–126 (2007). URL http://www.springerlink.com/index/10.1140/epjb/e2007-00210-8.

[145] Robinson, J. W. A., Piano, S., Burnell, G., Bell, C. & Blamire, M. G. Zero to π transition in superconductor-ferromagnet-superconductor junctions. *Physical Review B* **76**, 094522 (2007). URL https://link.aps.org/doi/10.1103/PhysRevB.76.094522.

[146] Bannykh, A. A. *et al.* Josephson tunnel junctions with a strong ferromagnetic interlayer. *Physical Review B* **79**, 054501 (2009). URL https://link.aps.org/doi/10.1103/PhysRevB.79.054501.

[147] Blum, Y., Tsukernik, A., Karpovski, M. & Palevski, A. Oscillations of the Superconducting Critical Current in Nb-Cu-Ni-Cu-Nb Junctions. *Physical Review Letters* **89**, 187004 (2002). URL https://link.aps.org/doi/10.1103/PhysRevLett.89.187004.

[148] Yates, K. A. *et al.* Andreev bound states in superconductor/ferromagnet point contact Andreev reflection spectra. *Physical Review B* **95**, 094516 (2017). URL https://link.aps.org/doi/10.1103/PhysRevB.95.094516.

[149] Usman, I. T. M. *et al.* Evidence for spin mixing in holmium thin film and crystal samples. *Physical Review B* **83**, 144518 (2011). URL https://link.aps.org/doi/10.1103/PhysRevB.83.144518.

[150] Di Bernardo, A. *et al.* Signature of magnetic-dependent gapless odd frequency states at superconductor/ferromagnet interfaces. *Nature Communications* **6**, 8053 (2015). URL http://www.nature.com/articles/ncomms9053.

[151] Khasawneh, M. A., Pratt, W. P. & Birge, N. O. Josephson junctions with a synthetic antiferromagnetic interlayer. *Physical Review B* **80**, 020506 (2009). URL https://link.aps.org/doi/10.1103/PhysRevB.80.020506.

[152] Bakurskiy, S. V. *et al.* Theoretical model of superconducting spintronic SIsFS devices. *Applied Physics Letters* **102**, 192603 (2013). URL http://aip.scitation.org/doi/10.1063/1.4805032.

[153] Robinson, J. W. A., Chiodi, F., Egilmez, M., Halász, G. B. & Blamire, M. G. Supercurrent enhancement in Bloch domain walls. *Scientific Reports* **2**, 699 (2012). URL http://www.nature.com/articles/srep00699.

[154] Houzet, M. & Buzdin, A. I. Long range triplet Josephson effect through a ferromagnetic trilayer. *Physical Review B - Condensed Matter and Materials Physics* **76**, 060504 (2007). URL https://link.aps.org/doi/10.1103/PhysRevB.76.060504. 0705.2929.

[155] Robinson, J. W. A., Banerjee, N. & Blamire, M. G. Triplet pair correlations and nonmonotonic supercurrent decay with Cr thickness in Nb/Cr/Fe/Nb Josephson devices. *Physical Review B* **89**, 104505 (2014). URL https://link.aps.org/doi/10.1103/PhysRevB.89.104505.

[156] Maxfield, B. W. & McLean, W. L. Superconducting Penetration Depth of Niobium. *Physical Review* **139**, A1515–A1522 (1965). URL https://link.aps.org/doi/10.1103/PhysRev.139.A1515.

[157] Epperlein, P. W. Magnetic penetration depths in superconducting Nb films. *Physica B+C* **108**, 931–932 (1981). URL https://www.sciencedirect.com/science/article/pii/0378436381907695?via%3Dihub.

[158] Weides, M. *et al.* Ferromagnetic 0-π Josephson junctions. *Applied Physics A: Materials Science and Processing* **89**, 613–617 (2007). URL http://link.springer.com/10.1007/s00339-007-4206-3. 0701693.

[159] Pfeiffer, J. *et al.* Static and dynamic properties of 0, π, and 0-π ferromagnetic Josephson tunnel junctions. *Physical Review B - Condensed Matter and Materials Physics* **77**, 214506 (2008). URL https://link.aps.org/doi/10.1103/PhysRevB.77.214506. 0801.3229.